DOE/ER/14092--1

NONUNIFORM LIOUVILLE TRANSFORMERS FOR QUASI-HOMOGENEOUS OPTICAL FIELDS

FINAL TECHNICAL REPORT

Grant No.: DE-FG03-89ER14092

Period of Performance: 09-25-89 to 01-22-93

Sponsor:

U.S. Department of Energy

Contractor:

Physical Optics Corporation
20600 Gramercy Place, Suite 103
Torrance, CA 90501
(310) 320-3088

Principal Investigator:

Tomasz Jannson, Ph.D.
(310) 320-3088

March 1993

TABLE OF CONTENTS

APPENDICES

PROGRAM SUMMARY

During the last two decades, there have been dramatic improvements in the development of optical sources. Examples of this development range from semiconductor laser diodes to free electron beam lasers and synchrotron radiation. Before these developments, standards for the measurement of basic optical parameters (quantities) were less demanding. Now, however, there is a fundamental need for new, reliable methods for providing fast quantitative results for a very broad variety of optical systems and sources. This is particularly true for partially coherent optical beams, since all optical sources are either fully or partially spatially coherent (including Lambertian sources).

Until now, there has been no satisfactory solution to this problem. During the last two decades, however, the foundations of physical radiometry have been developed by Walther [1-3], Wolf and co-workers [4-24]. By integrating physical optics, statistical optics and conventional radiometry, this body of work provides necessary tools for the evaluation of radiometric quantities for partially coherent optical beams propagating through optical systems [25,26]. In this program, Physical Optics Corporation (POC) demonstrated the viability of such a radiometric approach for the specific case of generalized energy concentrators called Liouville transformers. We believe that this radiometric approach is necessary to fully characterize any type of optical system since it takes into account the partial coherence of radiation.

In this program, POC developed a new theoretical model and techniques for computing the transformation of radiometric quantities of partially coherent optical beams through linear optical systems. These techniques employ radiometric ray tracing (R^2T) methods based on semigeometrical phase-space trace formulas that are valid for quasi-homogeneous sources in the short-wavelength approximation. In particular, in this program the theoretical foundations of the R^2T method for a broad class of sources, systems, and geometries were established. These foundations included both the first order short wavelength approximation and higher approximation orders.

Previous attempts to provide quantitative measurements on a physical optics (and statistical optics) level were too complicated for any practical use. They were based on 4-D Fresnel diffraction formulas with an 8-D system kernel. By contrast, POC's R^2T approach is much more simple and practical due to the implementation of a new model of generalized radiance in 4-D phase-space which obtains all basic radiometric quantities, such as radiant emissivity (and optical intensity), radiant intensity and energy flux. These quantities fully characterize propagation of partially

coherent beams through optical systems. In addition, POC's R^2T method is more general than geometrical ray tracing because it provides quantitative results in the form of spatial/angular 2-D distributions of radiometric quantities while still preserving the information about the spatial coherence of the optical beam. By contrast, the geometric ray tracing is not able to provide either of those two quantitative results. As a result, POC's R^2T model is the only effective quantitative means for computing all the above radiometric quantities for partially coherent optical beams for a broad variety of optical systems. These include free-space propagation [25-26], non-imaging concentrators and collimators [25], large aperture waveguides with variable cross-sections [25], imaging systems [27] based on first order optics [28], holographic systems [29], and other linear optical systems including aperture stops [25]. The family of optical sources that can be analyzed by this method includes non-Lambertian quasi-homogeneous sources [7] with non-uniform intensity 2-D spatial distribution and a statistically homogeneous [30] non-uniform 2-D distribution of a complex degree of spatial coherence. The broad variety of sources that belongs to this family includes high-power pulse/CW lasers, synchrotron radiation, semiconductor lasers, Lambertian (thermal) sources and a broad class of non-Lambertian sources such as tungsten lamps, deuterium lamps, hollow cathodes, laser induced plasmas and many others. Also, general problems of radiation transfer and heat transfer can be analyzed by POC's R^2T approach.

There are many applications of this program that can benefit the U.S. Department of Energy. These benefits include progress in x-ray physics, radiometry, plasma physics, laser physics, spectroscopy, solar physics, in particular, and physical optics, statistical optics and optical engineering, in general, wherever we deal with partially coherent optical sources. In all these cases, POC's R^2T model can provide the only efficient tool to compute the transformation of optical beams through linear optical systems, in the form of the spatial/angular distribution of radiometric quantities. This is especially important in the case where we need to compute the output distribution of the radiometric quantities, based on the knowledge of the input (source) distribution of optical radiation as well as the optical system transmitting this radiation. The energy related areas of interest (discussed in detail in the text) include LLNL's AVLIS program and synchrotron radiation facilities for high accuracy source calibration, to mention only a few.

1.0 INTRODUCTION

This section will present the general background of semigeometrical phase-space trajectories and their significance to physical and statistical optics.

1.1 Historical Background

The origins of semigeometrical phase-space trajectories related to POC's R^2T model can be traced to the well-known brightness theorem [32] , obtained on a purely geometrical basis, which is a basic theorem of conventional radiometry (the oldest area of optics (Leonardo De Vinci)). It can be shown that the brightness (radiance) theorem for imaging optical systems is a particular form of an optical analog of the Liouville theorem (Marcuse [33] and others [34,35]). The Liouville theorem has been successfully applied to evaluating the maximum concentration limit for non-imaging optical systems and has demonstrated the impossibility of constructing such an ideal non-imaging system with axial symmetry (Winston and Welford [35]). Using the Liouville theorem in spherical coordinates (also see Appendix A), however, it is possible to demonstrate an ideal concentration system with spherical symmetry (Jannson and Winston [34]).

A fundamental breakthrough in theoretical radiometry was achieved by Walther [1,2] who included spatial coherence in definitions of generalized radiance. Using these definitions, Wolf and co-workers [3-23] established the foundations for physical radiometry. Using the apparatus of physical radiometry [3-23,36-38], the physical optics generalization of the brightness theorem was proven by Walther [3] and Simon and Wolf [27] for Walther's second definition of radiance [2] and by Kim [24] for the first of Walther's definitions of radiance [1]. (This can be identified with the Wigner distribution [39], which is well known in quantum mechanics.) Specifically, for this program, Simon and Wolf [27] provided a rigorous proof of the physical brightness theorem in the short-wavelength asymptotic approximation for first order optical system [28,40], and Wolf et al. [38] proved the physical brightness theorem for all "good" definitions of radiance analyzed by Friberg et al. [10,38]. Moreover, Bastiaan [40] and Kim [24], using Walther's first definition of radiance, have shown that the physical brightness theorem can be extended to Fresnel diffraction in free-space, if diffraction aperture effects can be ignored. Furthermore, during this program, it was shown that the physical brightness theorem can be used in the case of Fresnel diffraction, even if diffraction aperture effects are included, assuming that certain necessary conditions are satisfied (Jannson, Tengara [25,26]).

The preliminary formulation of the R^2T model was presented by POC at the 1991 Annual Meeting of the Optical Society of America (Jannson, Tengara, Tin [25,26]), and then at the 10th Symposium on Energy Engineering Sciences, Argonne National Laboratory, May 1992.

In spite of the remarkable progress in physical radiometry [3-23,36-38], rigorous definition of the area of the validity of the R^2T concept still remains an issue. This is basically because of the asymptotic ($\lambda \rightarrow 0$) character of R^2T. Of course, the mathematical difficulties of the asymptotic approximations are well-known, particularly in the context of asymptotic relations between quantum mechanics and classical mechanics (see, e.g., Ref. [41]). Fortunately, in free-space, the semigeometrical asymptotic R^2T model is also recognized as a first order term in a Taylor series, with respect to the dimensionless parameter $\lambda z f^2$ [11]. Using this parameter, the higher-order terms can be ignored if $\lambda z f^2 << 1$ (λ is the optical wavelength, z is the distance between the input and output planes, and f is the maximum spatial frequency of the input intensity spatial distribution) assuming the quasi-homogeneous source model [7].

Carter and Wolf [7] demonstrated that the concept of quasi-homogeneous sources is fundamental to physical radiometry. Using the concept of quasi-homogeneous sources, it was possible to integrate physical radiometry with Fourier optics (Jannson [11]). Quasi-homogeneous sources are statistically homogeneous, and poorly-coherent, in the sense of global spatial coherence. The concept of global spatial coherence introduced by Kondratienko and Skrinsky [42] , Kim [24], and Nemez [43], states that an optical beam of interest, is (fundamentally) spatially poorly-coherent, if its 4-D phase-space effective hyper-area (PSEA) is much larger than the elementary cell ($\Delta x \Delta y \Delta px \Delta py \sim (\lambda/2)^2$) in 4-D phase-space ($x,y;p_x,p_y$), where p_x and p_y represent the optical directional cosines. By contrast, if PSEA ~ $(\lambda/2)^2$, the optical field is fully spatially coherent (e.g., single-mode Gaussian laser beam [31]), as a result of an optical analog of Heisenburg's uncertainty principle.

In the case of quasi-homogeneous sources, a number of important theorems of physical optics can be generalized. Those include the Van Cittert Zernike theorem [32], and the 2-D Wiener-Khintchine theorem [32]. Moreover, it has been shown (Carter and Wolf [7]) that, in the case of quasi-homogeneous sources, both of Walther's definitions of generalized radiance coincide, being "good" definitions of generalized radiance (since they are always non-negative) in the sense of Friberg [10]. In addition, it was shown that, in the case of statistically-homogeneous optical fields, the Van Cittert Zernike theorem can be generalized as a general propagation law, since it is the consequence of satisfying by the complex degree of spatial coherence of the Helmholtz equation with respect to a difference of coordinates (see Appendix D) [30].

POC believes that these recent developments in physical radiometry and the theory of coherence represent an excellent foundation which can lead to a general model of propagation of partially coherent radiation through optical systems. This can have important implications in many Department of Energy current interests.

1.2 POC's Approach

As an intermediate approach between geometrical optics and wave diffraction, POC introduced the new concept of semigeometrical phase-space trajectories and radiometric ray tracing (R^2T) during the initial two years of this DOE program. This development has major implications as a theoretical and practical tool for the effective computing of partially coherent optical beams throughout a broad variety of optical systems. These applications include free-space, non-imaging optical systems, imaging optical systems, laser resonators and holographic optical systems. Because of their relationship to phase-space density and to the Liouville theorem, the general theoretical formulas governing semigeometrical phase-space trajectories were referred to before as Nonuniform Liouville Transformers (NLT).

POC's R^2T approach is more general than geometrical optics. This is because it provides *quantitative* relations for radiometric quantities such as emissivity, radiant intensity, and energy flux, while also including the spatial coherence of the optical beam as an additional parameter of the system. Although R^2T is less general than a wave diffraction model, it offers an obvious advantage over the latter, because R^2T provides the necessary quantitative results without troublesome and time-consuming computations of four-dimensional (4-D) diffraction integrals in the spatial domain. Furthermore, the R^2T concept can be used in sophisticated geometries such as non-imaging optics, in which standard computing, based on wave diffraction, is hopelessly complicated. In these cases, geometrical optics provides only qualitative results and not the quantitative results for radiometric quantities provided by R^2T.

More specifically, POC's R^2T model generalization of conventional non-imaging optics [34,35] falls into the following four major categories (three of them are related to optical source features and the fourth to non-imaging system geometry):

1. *Nonuniform* intensity 2-D spatial distribution in the input source plane
2. *Partial* spatial coherence of a source

3. *Non-Lambertian* source angular distribution
4. *Anisotropic* (e.g., elliptic) cross-section of non-imaging concentrator/collimator systems

These categories are summarized in Table 1-1.

Table 1-1. R^2T Non-Imaging Optics vs Conventional Non-Imaging Optics

Feature	Conventional Non-Imaging Optics	R^2T Non-Imaging Optics
1. Source Intensity Spatial Distribution	Uniform	Generally Nonuniform
2. Source Spatial Coherence	(N/A, Indirectly Assumed Incoherence)	Partial
3. Source Angular Distribution of Radiation	Lambertian	Generally Non-Lambertian
4. Geometry of Non-Imaging System	Isotropic	Generally Anisotropic

In general, R^2T quantification can be applied to a broad variety of optical systems. These systems include free-space, astigmatic and stigmatic imaging systems (in the first order optics approximation) [28,40], isotropic and anisotropic non-imaging systems and holographic imaging systems (Figure 1-1). Moreover, under certain conditions, weak diffraction effects on apertures (edges and slits, etc.) can also be included.

The variety of optical sources which can be computed using the R^2T model is also very broad. This range includes the majority of partially-coherent sources, such as high-power pulse lasers, semiconductor lasers (laser diodes), synchrotron radiation, all classical (Lambertian) sources, non-Lambertian sources, and a broad variety of secondary optical sources, such as video displays.

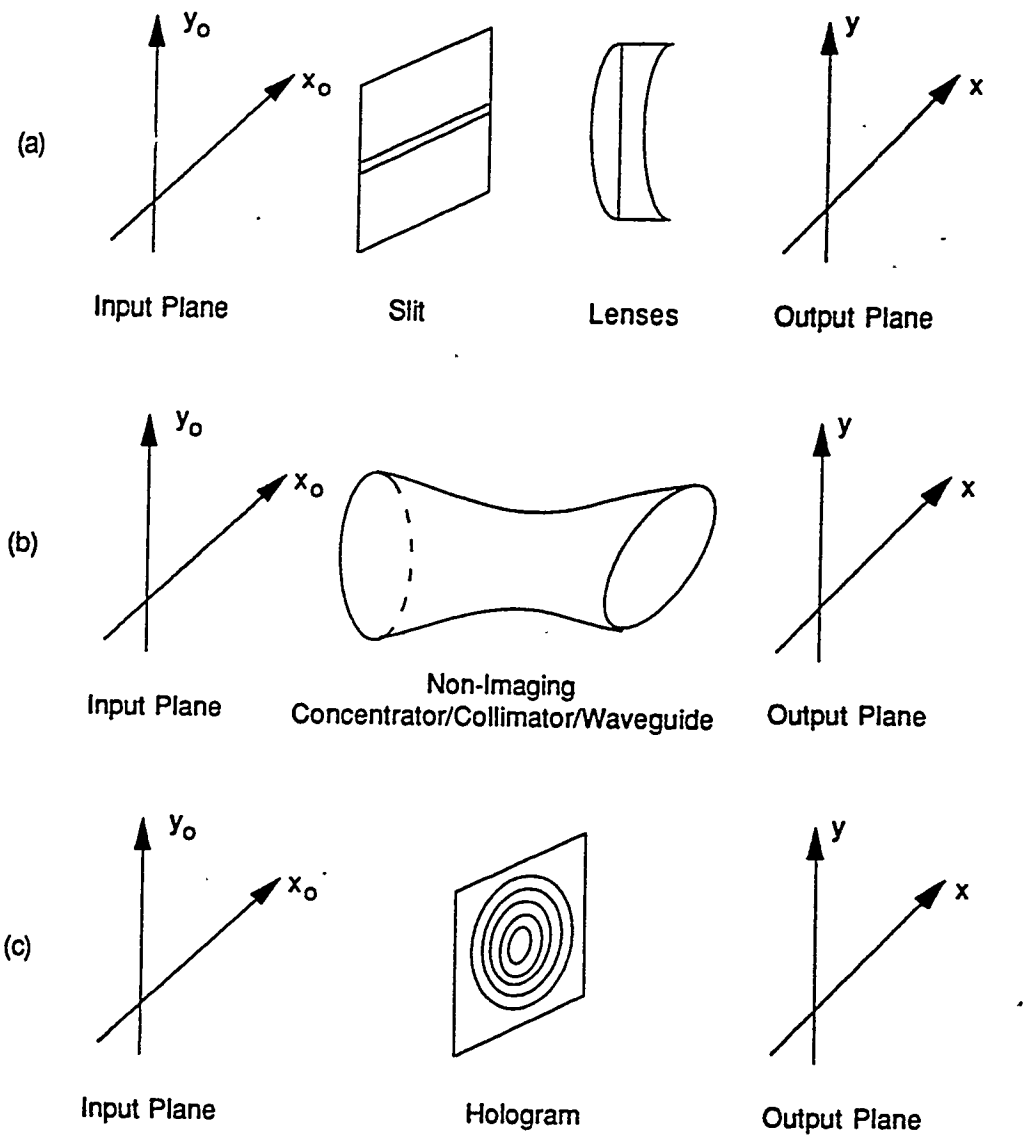

Figure 1-1
Illustration of Optical Systems That Can Be Computed by the R^2T Model. They include (a) imaging systems (stigmatic and astigmatic) with aperture stops, (b) non-imaging systems (isotropic and anisotropic), and (c) holographic imaging systems.

1.2.1 Summary of Theoretical Results

The foundations of the radiometric and the R^2T approach were established by POC during this program. In particular, the following results were established by POC:

1. A more general model than the short-wavelength asymptotic approximation R^2T model, based on Taylor series expansion of radiance transfer function (RTF), has been formulated for free-space (see Refs. [25, 26]), including not only the so-called asymptotic (first order) approximation [27], but also the second order and the third order approximation containing $O(\lambda)$ and $O(\lambda^2)$ terms, respectively.

2. A rigorous derivation of the R^2T model for the imaging systems in the first-order optics approximation has been formulated (see Ref. [27] and Appendix C). Another approach to imaging optical systems, based on Fourier optics was formulated by the author ten years ago [11]. Also, the R^2T model has been compared with conventional approach, from a computer time budget point of view.

3. Using the second order short wavelength approximation, the validity of the R^2T model has been evaluated in free-space, based on the four conditions (see Refs. [25, 26]), defining the Fresnel diffraction approximation quasi-homogeneity of the optical source, the R^2T first order approximation, and the non-existence of non-homogeneous waves. Those conditions have been proven to be necessary and sufficient by using direct computing.

4. The generalized van Cittert Zernike theorem for statistically-homogeneous optical fields has been proven (see Ref. [30] and Appendix D), demonstrating that the propagation of spatial coherence can be described by (linear) Helmholtz wave equation.

5. The R^2T model has been extended to non-imaging optics, far beyond Winston's model based on uniform Lambertian sources (see Table 1-1).

6. The graphic method of phase-space diagrams demonstrating the evolution of optical beams has been demonstrated. This method has been confirmed experimentally by using a PSEA measuring device.

7. For experimental purposes, sources with regulated spatial coherence, based on POC's rotating (graded refractive index) GRIN diffusers, were designed and demonstrated.

8. A theoretical model of holographic optical elements (HOEs) with tunable angular coherence characteristics has been demonstrated (see Ref. [29]), and preliminary experimental results have been obtained using such HOEs as radiation sources.

Some of the major results of previous studies were based on a paper by the PI of this project [11]. They integrate physical radiometry with Fourier optics (see Results 1, 2, 3)). Other relevant publication prepared under this program include:

A. T. Jannson, L. Sadovnik, T. Aye, I. Tengara, "Radiometric Ray Tracing," J. Opt. Soc. Am. (Dec. 1991), Proc. of the 1991 OSA Annual Meeting, San Jose (Nov. 1991); MCC4; see also T. Jannson, I. Tengara, "Radiometric Ray Tracing," Proc. of the 10th Symposium on Energy Engineering Sciences, Argonne National Laboratory (May 1992).

B. R. Simon, E. Wolf, "Transfer of Radiance by Gaussian-Schell Model Beams in Paraxial System," submitted to J. Opt. Soc. Am. B.

C. E. Wolf, J. Jannson, T. Jannson, "Analogue of the van Cittert Zernike Theorem for Statistically Homogeneous Wave Field," Opt. Lett., 5, 1032 (1990).

D. T. Jannson, I. Tengara, "Lippmann-Bragg Broadband Holographic Mirrors," J. Opt. Soc. Am., 8, 201 (1991).

E. T. Jannson, I. Tengara, and D. Erwin, "Semigeometrical Phase-Space Trajectories in Physical Radiometry," in preparation.

1.3 The Basic Principles of the R^2T Model

Conventionally, a linear optical system can be described either qualitatively by geometrical optics or quantitatively by a wave diffraction model. Considering the spatial coherence of the optical beam, the general diffraction formula for the monochromatic case has the following form [44,45]:

$$W(x_1,y_1;x_2,y_2) = \iiiint G(x_1,y_1;x_2,y_2;x_{01},y_{01};x_{02},y_{02}) \\ W_o(x_{01},y_{01};x_{02},y_{02})\,dx_{01}\,dy_{01}\,dx_{02}\,dy_{02} \qquad (1\text{-}1)$$

where G is an 8-D kernel describing the linear optical system, and W is the cross-spectral density, in the form [32]:

$$W(x_1,y_1;x_2,y_2) = \left\{U^*(x_1,y_1)\,U(x_2,y_2)\right\}_{ens} \qquad (1\text{-}2)$$

where U(x,y) is the complex amplitude. The asterisk denotes the conjugation operation and $\{\ldots\}_{ens}$ denotes the ensemble average. In general, the cross-spectral density can be represented as [32]

$$W(x_1,y_1;x_2,y_2) = \mu(x_1,y_1;x_2,y_2)\sqrt{I(x_1,y_1)}\sqrt{I(x_2,y_2)} \tag{1-3}$$

where μ is the complex degree of spatial coherence ($|\mu| \leq 1$), and I is the optical intensity.

It should be emphasized that, in spite of the tremendous complexity of the 4-D diffraction formula (Eq. (1-1)), this is only the first step in computing more sophisticated optical systems such as those illustrated in Figure 1-1. In fact, in the case of non-imaging systems, it is necessary to use this formula many times in an iterative manner, a hopelessly complicated scenario from a computer time budget perspective.

Obviously, a simplified method for computing radiometric quantities which preserves the features of the optical beams, such as non-uniform intensity and partial spatial coherence, is highly desired. This is particularly true for energy-related applications. We believe that the R^2T computing method based on semigeometrical phase-space trajectories can fill this gap. As illustrated in Figure 1-2, the general R^2T computing procedure can be broken down into three major steps:

1. *Calculation of input phase-space density*, B_o (generalized brightness and the generalized radiance function are among several names used for this function), from optical intensity (I_o), degree of spatial coherence (μ_o), and spatial distribution; i.e.,

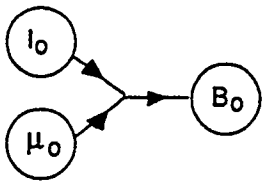

(1-4)

2. *Projection of the radiance function* (B) in phase-space according to Fermat's principle:

$$B_o(\vec{R}_o,\vec{s}_o) = B(\vec{R},\vec{s}) \tag{1-5a}$$

where

$$(\vec{R}_o,\vec{s}_o) \xrightarrow{\text{Fermat's Principle}} (\vec{R},\vec{s}) \tag{1-5b}$$

Here, $\vec{R} = (x,y,z)$, and $\vec{s} = (s_x,s_y,s_z)$ is unit vector of observation.

3. *Integration of radiance function,* either in the space domain (x,y) or the direction domain (s_x, s_y), in order to obtain measurable radiometric quantities such as emissivity (E), radiant intensity (J), and energy flux (F). For example, the direction integral is

$$E(x,y) = \iint B\left(x,y;s_x,s_y\right) ds_x\, ds_y \tag{1-6}$$

This 2-D integral is very simple, since it does not contain an oscillating 4-D kernel (in contrast to 2-D Fourier integrals, for example).

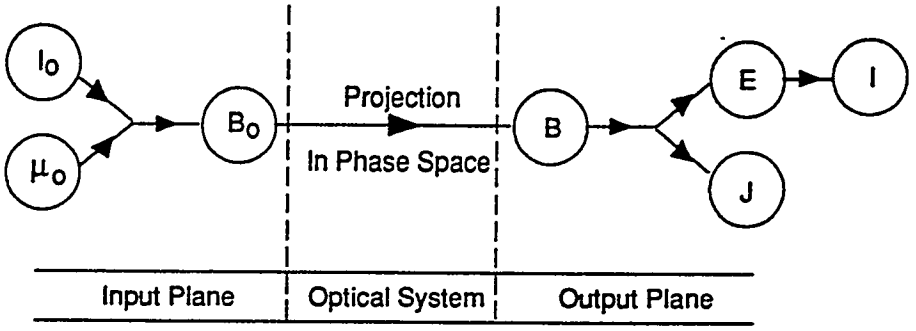

Figure 1-2
A Schematic of the General R^2T Computing Procedure. I_o is the input optical intensity, μ_o is the input complex degree of spatial coherence, B_o is the generalized input radiance, B is the generalized output radiance, E is the output emissivity, J is the output radiant intensity, and I is the output optical intensity.

Comparing Eqs. (1-4) to (1-6) with Eq. (1-1), it is seen that the R^2T computing model, Eqs. (1-4) to (1-6), is indeed much simpler than the wave diffraction model, Eq. (1-1), and that the computer time savings are therefore obvious. We can safely say that the R^2T approach is the only practical approach that can be used for computing propagation radiometric quantities of partially coherent optical beams through linear optical systems. It should be noted that in paraxial approximation

$$E \cong I \tag{1-7}$$

Therefore, the R^2T model provides an indirect transformation of optical intensity through an optical system:

$$\boxed{I_o(x_o,y_o) \rightarrow I(x,y)} \tag{1-8}$$

even for partially spatially coherent optical beams, providing at the same time a factor of about 100:1 computer time saving in comparison to the scalar diffraction model for free-space. In the case of more sophisticated optical systems, especially including non-imaging optics based on total internal reflection (TIR), the R^2T approach is the only method for providing quantitative results for radiometric quantities.

1.3.1 Elementary Example--Free-Space in Paraxial Approximation

For Fresnel scalar diffraction, we have [44,45]

$$I(x,y) \equiv \iiint G(x,y;x_{01},y_{01};x_{02},y_{02}) \mu_o(x_{01},y_{01};x_{02},y_{02}) \sqrt{I_o(x_{01},y_{01})}\sqrt{I_o(x_{02},y_{02})} dx_{01}dy_{01}dx_{02}dy_{02} \quad (1\text{-}9)$$

where G is the 6-D Fresnel diffraction kernel [44,45] The respective R^2T diagram, illustrated in Figure 1-3, consists of three basic steps:

$$B_o(\vec{r},\vec{p}) = s_z I_o(\vec{r}_o)\tilde{\mu}_o(\vec{p}/\lambda) \quad (1\text{-}10a)$$

$$B(\vec{r},\vec{p}) = B_o\left[\vec{r} - (z/s_z)\vec{p},\vec{p}\right] \quad (1\text{-}10b)$$

$$I(\vec{r}) \equiv \iint B(\vec{r},\vec{p})d^2p;\ d^2p = dp_x\, dp_y; \quad (1\text{-}10c)$$

where $\tilde{\mu}(\vec{p}/\lambda) = \hat{F}\{\mu(\vec{r}')\}$.

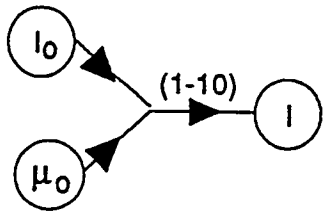

Figure 1-3
Elementary R^2T Diagram for Free-Space in Paraxial Approximation

Comparing Eqs. (1-9) and (1-10), instead of 4-D integration (1-9) with a 6-D kernel, we have 2-D projection (1-10b) and 2-D integration (1-10c) with a 4-D kernel. In addition, in order to evaluate the input radiance, $B_o(\vec{r},\vec{p})$, it is usually sufficient to know only the input intensity 2-D spatial

distribution, $I_o(\vec{r}_o)$, since the input 2-D distribution of the complex degree of spatial coherence $\mu_o(\vec{r}')$ is usually determined by the general character of the optical source, as it is in the case of synchrotron radiation [24,46] (see Figure 1-3).

In order to compare the scalar Fresnel diffraction model and the R^2T model with respect to computer time expenditure, three computers were used: a Sun Sparc Station, a CRAY Y-MP and an Everex PC. The results are summarized in Table 1-2. It is seen that the difference in duration of computer use is quite significant, up to 778:1 for the Everex PC and the 1-D case (1.06 h vs. 4.9 sec) and about 30:1 for the 2-D case. Of course, only the free-space case (and space-invariant imaging system) can be used for comparison, since non-imaging optical systems, space-invariant imaging systems, and holographic systems [29] are too complicated to use the Fresnel diffraction model in an iterative manner. It should be emphasized that only POC's Everex PC R^2T software is specially adjusted for this type of computation. The Gaussian-correlated (σ_g) circular source of radius a with either a Gaussian intensity distribution (σ_S) or with a constant profile ($\sigma_S = \infty$) was used for comparison:

$$I_o(\vec{r}) = \exp\left(-\frac{r^2}{2\sigma_s^2}\right) \mathrm{circ}\left(\frac{r}{a}\right) \tag{1-11a}$$

$$\mu_o(\vec{r}') = \exp\left(-\frac{r'^2}{2\sigma_g^2}\right); \sigma_g << \sigma_s \tag{1-11b}$$

Using Walther's second definition of generalized radiance [2] and the radiance transfer function (RTF) model [11], it has been shown that the R^2T model is valid in free-space for $z < z_1$, where

$$z_1 = \frac{\Lambda_1^2}{10\lambda}, \tag{1-12}$$

and Λ_1 is the resolving element of the spatial intensity distribution. For example, for typical synchrotron sources, $\Lambda_1 = 1$ mm and $z_1 = 10$ cm for $\lambda = 1$ μm.

Table 1-2 Comparison of Computation Times for Computing Emissivity by Using Various Computers

	One-Dimensional Line Source Intensity with Constant Profile Average Number of Plotting Point for x = 40							Two-Dimensional Circular Source Intensity with Gaussian Profile Average Number of Plotting Points for (x,y) = 625			
	Order of Integration	Computation Time for Relative Error ≤ 10^{-6}						Order of Integration	Computation Time for Relative Error ≤ 10^{-4}		
		Parameters Used: z = 0, $\frac{2\pi\sigma_g}{\lambda} = 20$, $\frac{2\pi a}{\lambda} = 500$			Parameters Used: z = 10, $\frac{2\pi\sigma_g}{\lambda} = 400$, $\frac{2\pi a}{\lambda} = 2000$				Parameters Used: z = 50, $\frac{2\pi\sigma_g}{\lambda} = 20$, $\frac{2\pi a}{\lambda} = 2000$, $\frac{2\pi\sigma_s}{\lambda} = 2000$		
		Sun Sparc Station 1+ (FORTRAN)	Cray Y-MP (FORTRAN)	Everex PC 486/33 MHz (Microsoft BASIC 7.1)	Sun Sparc Station 1+ (FORTRAN)	Cray Y-MP (FORTRAN)	Everex PC 486/33 MHz (Microsoft BASIC 7.1)		Sun Sparc Station 1+ (FORTRAN)	Cray Y-MP (FORTRAN)	Everex PC 486/33 MHz (Microsoft BASIC 7.1)
Fresnel Method	2	408 sec	24 sec	244 sec	8.2 hr	0.46 hr	1.06 hr	4	7,795 hr	463 hr	4,661 hr
Radiometry Method	1	0.27 sec	0.016 sec	0.16 sec	38 sec	2 sec	4.9 sec	2	252 hr	15 hr	151 hr

In order to independently confirm this result, the Fresnel diffraction and R^2T methods have been computed directly for free-space using Eqs. (1-9) and (1-10a) through (1-10c), respectively, for the (1-11a) and (1-11b) 1-D source model with $\sigma_S = \infty$, and the following criteria:

$$Q = \left(\frac{z}{a}\right)^3 \frac{4\lambda}{\pi a}\left(1+\frac{x}{a}\right)^4 >> 1 \quad \text{(Fresnel approximation)} \qquad \text{(1-13a)}$$

$$a/\sigma_g >> 1 \text{ (quasi-homogeneity approximation)} \qquad \text{(1-13b)}$$

$$\phi_F = \lambda z f_1^2 << 1 \qquad \text{(1-13c)}$$

(R^2T first order approximation equivalent to Eq. (1-12) for $f_1 = \frac{1}{\Lambda_1}$)

$$\sigma_g/\lambda > 1 \text{ (no evanescent waves)} \qquad \text{(1-13d)}$$

In Figure 1-4 it is seen that these two models indeed nearly coincide for $Q = 98$, $a/\sigma_g = 25$, $\sigma_g/\lambda = 3$, and $\phi_F = 0.62$; i.e., where all four criteria are satisfied. Computing results suggest that the criteria (1-13) indeed create the set of necessary and sufficient conditions for the reliability of a specific R^2T theoretical model of physical radiometry.

Considering the parallel results [24] based on the first of Walther's definitions of generalized radiance [1], further studies are necessary to establish a solid base for the R^2T model.

The reliability of the RTF model [11], represented by Eq. (1-12) has been tested by verifying that the criteria (1-13a,b,c,d) constitute the set of necessary and sufficient conditions for agreement between the output spatial emissivity distributions, obtained by using either Eq. (1-5) or Eqs. (1-10). Since, Eqs. (1-9) and (1-10a,b,c) do not depend on any specific definition of generalized radiance, they should constitute objective criteria to evaluate any theoretical R^2T model of physical radiometry, dependent on any specific definition of generalized radiance.

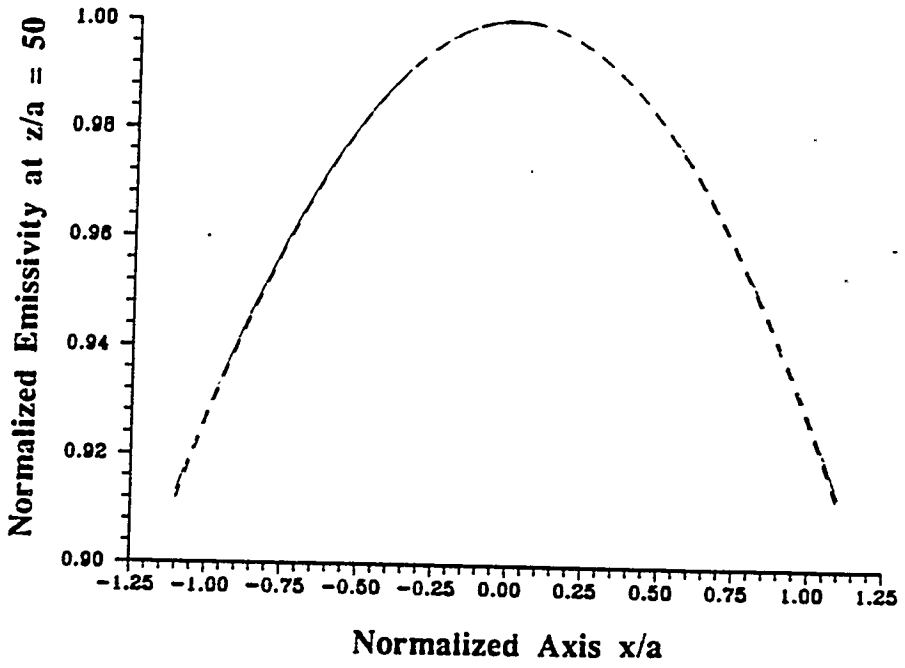

Figure 1-4
Comparison of Emissivity Distribution for Fresnel Diffraction (Solid Line) and R^2T (Broken Line). 1-D Free-Space Models for Q = 98, $a/\sigma_g = 25$, $\sigma_g/\lambda = 3$, and $\phi_F = 0.62$.

1.3.2 Numerical Results for the R^2T Model

Using the Gaussian-correlated circular source model defined by Eqs. (1-11a and b), a broad variety of linear optical systems have been analyzed by using the radiometric ray tracing (R^2T) model. They include free-space [25,26], imaging systems in the first order optics approximation [27], and non-imaging concentrators/collimators and large-aperture waveguides [25] with a curved profile and anisotropic cross section (see Figure 1-1). Here, we present only one simple example of a truncated non-imaging cone with circular input and output radii of 0.15 mm and 0.6 mm, respectively. The input is a Gaussian correlated circular source of radius a with a Gaussian intensity at $z/a = 0$; $2\pi\sigma_g/\lambda = 20$, $2\pi a/\lambda = 1771$, and $2\pi\sigma_s/\lambda = 2000$. For this cone, statistical ray-tracing was provided with up to 3 total internal reflections, and the total number of rays was 7,110, 861. Using the R^2T model illustrated in Figure 1-2, a 2-D spatial distribution of emissivity $E(\vec{r})$ was computed at the output plane $z/a = 200$ (see Figure 1-5).

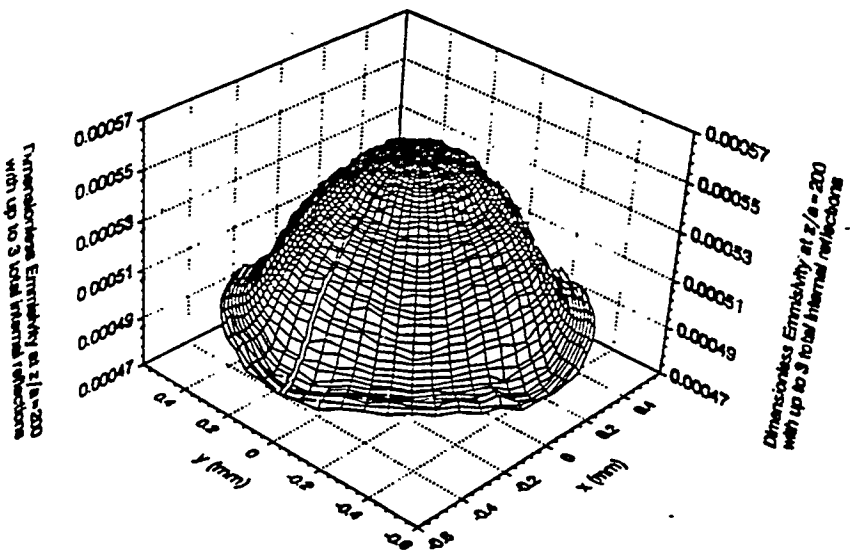

Figure 1-5
Illustration of 2-D Spatial Distribution of Output Emissivity (Optical Intensity) Computed by Using the R^2T Model. The output of the non-imaging optics truncated cone with input and output radii of 0.15 mm and 0.6 mm, respectively, is z/a = 200. The input is a Gaussian-correlated circular source of radius a with a Gaussian intensity at z/a = 0; $2\pi\sigma_g/\lambda = 20$, $2\pi a/\lambda = 1771$, $2\pi\sigma_s/\lambda = 2000$. The total number of rays using up to 3 total internal reflections is 7,110,861.

Using an approach similar to that illustrated in Figure 1-5, the analogous 2-D distributions of radiometric quantities (radiance, emittance, radiant intensity, energy flux) have been computed for the broad variety of optical systems illustrated in Figure 1-1. Using the R^2T method, the computer time saving factor is about 100:1 for free-space and practically infinite for more sophisticated non-imaging systems with reflection walls. The broad variety of quasi-homogeneous optical sources [7] that can be analyzed by using the R^2T model includes all Lambertian sources and a broad variety of non-Lambertian sources such as synchrotron radiation, high power pulse/CW lasers, semiconductor lasers, tungsten lamps, deuterium lamps, hollow cathodes, and laser induced plasma.

1.4 Program Philosophy

Much of conventional radiometry is concerned with the propagation of radiance through optical systems. However, as is well known, the radiance function is not a directly measurable quantity. The reason for this is that the radiance function $B(\vec{r},\vec{p})$ requires knowledge of both spatial and angular distribution, in contradiction to the Heisenberg uncertainty principle. Only certain averages

and integrals involving $B(\vec{r},\vec{p})$ represent physical observations, such as radiant emittance $E(\vec{r})$, optical intensity $I(\vec{r})$, radiant intensity $J(\vec{p})$, and energy flux E.

In this program, POC developed ray tracing techniques using the phase-space formation similar to that used to calculate quantities both in image-forming systems and in non-imaging concentrators. In particular, we developed computational techniques for tracing the radiance of optical beams through lens systems, utilizing the ABCD matrices which have been so successful in laser physics [31] . This program extends this theory to fields which are not beam like and for which the ABDC matrices cannot be used. The results would be of particular interest for non-imaging optics and for optics utilizing wide-angle systems. Light sources of particular interest include synchrotron radiation and wiggler radiation. These sources can be considered quasi-homogeneous while undulator radiation is less often quasi-homogeneous.

The remarkable success of applying semiclassical trace formulas [41] for the phase-space integration of energy density levels in quantum mechanics has created the opportunity for adapting these results into physical optics, in general, and to the generalization of semigeometrical phase-trajectories, in particular. The formal analogy between non-relativistic quantum mechanics and 2-D monochromatic paraxial physical optics has been developed by Gloge and Marcuse [48] and Eichmann [49] (with the z-coordinate "playing the role" of time in quantum mechanics). This analogy has been generalized in this program into "mixed" quantum states, with an optical analog of the quantum density matrix [53] governing the spatial coherence of the optical beam in the space-domain representation. In general, three density matrix representations have been shown to be closely related to radiometric quantities (see Appendix A) since they are related to cross-spectral density (1-14a), the radiance function (1-14b), and radiant intensity (1-14c):

$$\langle \vec{r} \,|\, \hat{\rho} \,|\, \vec{r}' \rangle \qquad \text{(1-14a)}$$

$$\langle \vec{r} \,|\, \hat{\rho} \,|\, \vec{p} \rangle \qquad \text{(1-14b)}$$

$$\langle \vec{p} \,|\, \hat{\rho} \,|\, \vec{p} \rangle \qquad \text{(1-14c)}$$

where $\hat{\rho}$ is the density operator

$$\hat{\rho} = \{ |U\rangle\langle U| \}_{ens} \qquad \text{(1-14d)}$$

$|U\rangle$ is the complex amplitude in Dirac notation [50-52], $\{ \ldots \}_{ens}$ is the ensemble average, $\vec{r} = (x,y)$, and $\vec{p} = (s_x,s_y)$. As a result, it has been shown in paraxial optics (equivalent to non-relativistic quantum mechanics) that the equation of motion for the optical density operator collapses to the optical Liouville theorem in the "classical" (i.e., short-wavelength) approximation, where λ plays the role of Planck's constant, h. This analogy played some role in the development of the R^2T model by either learning from recent semiclassical developments in quantum mechanics [41] or by using 2-D optical media in an analogy of "essentially 2-D" geometries of quantum mechanics.

Future areas of study will include a comprehensive evaluation of the validity of the R^2T model, further engineering development of this model as well as its generalization into more general sources and system geometries as well as into time-dependent polarization states (non-homogeneous source case) and higher orders of short wavelength approximation. The results should be useful for establishing new higher accuracy source calibration standards, based on synchrotron radiation [47] as well as for many problems in spectroscopy, high energy physics, plasma physics, solar physics, photonics, radiometry, etc., wherever quantitative evaluation of partially-coherent optical system is required.

2.0 TECHNICAL RESULTS

2.1 Semi-Geometrical Phase-Space Trace Formulas

2.1.1 Basic Definitions

Consider a monochromatic complex amplitude $u(\vec{R})$ satisfying the Helmholtz equation, where $\vec{R} = (x,y,z) = (\vec{r},z)$; then the 2-D Fourier transform has the form

$$\tilde{u}(\vec{f}') = \hat{F}\{u(\vec{r})\} = \int u(\vec{r}) e^{-i2\pi \vec{f}' \bullet \vec{r}} d^2r \qquad (2\text{-}1)$$

where $\vec{f}' = (f_x', f_y')$ is a spatial frequency vector of the complex amplitude and $d^2r = dxdy$.

Using the second of Walther's definitions [2] of generalized radiance, we have

$$B(\vec{r},\vec{p}) = 2\omega k s_z \, \mathrm{Re}\left[\left\{u(\vec{r})\,\tilde{u}^*(\vec{p}/\lambda)\right\}_{ens} \exp(-ik\vec{p}\cdot\vec{r})\right] \tag{2-2}$$

where $\{\ldots\}$ is the ensemble average, $\vec{s} = (s_x, s_y, s_z) = (\vec{p}, s_z)$ is the unit vector of the observation direction. We can also define the remaining radiometric quantities, such as energy flux:

$$F = \iiint B(\vec{r},\vec{p})\, d^2r\, d^2p \tag{2-3}$$

emittance,

$$E(x,y) = \iint B(\vec{r},\vec{p})\, d^2p \tag{2-4}$$

and radiant intensity,

$$J(p_x,p_y) = s_z \iint B(\vec{r},\vec{p})\, d^2r \tag{2-5}$$

It is also useful to introduce the complex radiance function, in the form [11]

$$\begin{aligned} B^{(+)}(\vec{r},\vec{p}) &= 2\omega k s_z \left\{u(\vec{r})\,\tilde{u}^*(\vec{p}/\lambda)\right\}_{ens} \exp(-ik\vec{p}\cdot\vec{r}) \\ &= 2\omega k s_z \iint W(\vec{r}',\vec{r}) \exp ik\vec{p}(\vec{r}'-\vec{r})\, d^2r' \end{aligned} \tag{2-6}$$

where $W(\vec{r}',\vec{r})$ is the cross spectral density function [4],

$$W(\vec{r}_1,\vec{r}_2) = \left\{u^*(\vec{r}_1)\,u(\vec{r}_2)\right\}_{ens} \tag{2-7}$$

and

$$B(\vec{r},\vec{p}) = \mathrm{Re}\left[B^{(+)}(\vec{r},\vec{p})\right] \tag{2-8}$$

We can write Eq. (2-7) in the form [4]

$$W(\vec{r}_1,\vec{r}_2) = \sqrt{I(\vec{r}_1)}\,\sqrt{I(\vec{r}_2)}\,\mu(\vec{r}_1,\vec{r}_2) \tag{2-9}$$

where μ is the complex degree of spatial coherence, $I(\vec{r}) = W(\vec{r},\vec{r})$ is the optical intensity, and due to well-known Schwartz inequality,

$$|\mu| \leq 1 \tag{2-10}$$

Eqs. (2-1) through (2-10) define the basic apparatus of physical radiometry [1-23] that integrates the radiometric quantities (radiance, emittance, radiant intensity, energy flux) with physical optics (complex wave amplitude, optical intensity), and the theory of spatial coherence (cross-spectral density, complex degree of spatial coherence). The formalism of physical radiometry, through statistical ensemble averaging, provides the fundamentals of statistical wave optics [45], equivalent to a "mixed states" representation of quantum mechanics [53], based on density matrix formalism [53].

The formal analogy between the cross-spectral density function (2-7) and the density matrix, discussed in Appendix A, provides a mechanism for the derivation of an optical analog of the Liouville theorem [33] as a semigeometrical asymptotic approximation of the density matrix dynamic equation.

2.1.2 Quasi-Homogeneous Sources

In the quasi-homogeneous source approximation [7], Eq. (2-9) becomes

$$W_o\left(\vec{r}_1, \vec{r}_2\right) \equiv I_o\left(\frac{\vec{r}_1+\vec{r}_2}{2}\right)\mu_o\left(\vec{r}_1, \vec{r}_2\right) \tag{2-11}$$

as well as [26]

$$B_o^{(+)}\left(\vec{r}, \vec{p}\right) = (1/2)B_o\left(\vec{r}, \vec{p}\right) \tag{2-12}$$

where index "o" denotes the source plane. Also, the generalized radiance function (2-2) becomes [7]

$$B_o\left(\vec{r}, \vec{p}\right) = 2\omega k s_z I_o\left(\vec{r}\right)\tilde{\mu}\left(\vec{p}/\lambda\right) \tag{2-13}$$

where

$$\tilde{\mu}(\vec{f}) = \hat{F}\{\mu(\vec{r})\}$$

In this approximation, both of Walther's definitions of generalized radiance coincide [7], and they are non-negative, and also satisfy all three Friberg's conditions (defining the properties of a physically-correct definition of radiance; non-negativeness; zeroing outside the source boundaries; and linear relation with cross-spectral density function) [10]. This approximation holds for statistically homogeneous spatial coherence:

$$\mu_o(\vec{r}_1, \vec{r}_2) = \mu_o(\vec{r}_1 - \vec{r}_2) \tag{2-14}$$

and for slowly-varying source intensity I_o, in respect to spatial coherence degree, such as, that [11]

$$a >> \rho_{coh} \tag{2-15}$$

where a is the resolution element of the intensity spatial distribution $I_o(\vec{r})$, and ρ_{coh} is the spatial coherence radius.

2.1.3 Paraxial Approximation

Using Eqs. (2-2) and (2-4), we obtain the following formula for the generalized radiant emissivity [36]:

$$E(\vec{r}) = (c/k)\,\mathrm{Im}\left\{u^* \frac{\partial u}{\partial z}\right\}_{ens} \tag{2-16}$$

where Im{ ... } determines the imaginary part and the Poynting vector (in scalar approximation) is [36]

$$\vec{S} = (c/k)\,\mathrm{Im}\{u^* \nabla u\}_{ens} \tag{2-17}$$

In the paraxial approximation, we have

$$\frac{\partial u}{\partial z} \equiv i k s_z u \tag{2-18}$$

thus, using Eq. (2-16), we obtain ($s_z \equiv 1$),

$$E(\vec{r}) = c s_z \left\{ |u|^2 \right\}_{ens} \propto I(\vec{r}) \tag{2-19}$$

i.e., the emissivity is proportional to the optical intensity.

2.1.4 Semigeometrical Phase-Space Trace Formulas in the First Order Short Wavelength Approximation

The geometrical brightness theorem, obtained by a geometrical ray tracing analysis, is well known [32]. Here, we will obtain the physical optics generalization of brightness theorem, obtained on the basis of physical radiometry and Fourier optics [44]. A more comprehensive analysis of this problem, obtained for the Gaussian-Schell model beams in paraxial systems, has been provided for this program by Simon and Wolf [27] in Appendix C.

The generalized radiance propagation through space-invariant linear systems has the form

$$B(\vec{r},\vec{p}) = \iint g(\vec{r}-\vec{r}_o,\vec{p}) B_o(\vec{r}_o,\vec{p})\, d^2 r_o \tag{2-20}$$

where g is the radiance spread function. In the case of short-wavelength ($\lambda \to 0$), the radiance spread function reduces to the Dirac delta function [11]

$$g(r-r_o,p) = \delta\left[\vec{r}-\vec{r}_o-(z/s_z)\vec{p}\right] \tag{2-21}$$

and the 2-D integral of Eq. (2-20) reduces to the simple phase-space $(\vec{r},\vec{p})$ trace relation [11]:

$$B(\vec{r},\vec{p}) = B_o\left[\vec{r}-(z/s_z)\vec{p},\vec{p}\right] \tag{2-22}$$

thus, the radiant emittance is

$$E(\vec{r}) = \iint B(\vec{r},\vec{p}) d^2 p = \iint B_o\left[\vec{r}-(z/s_z)\vec{p},\vec{p}\right] d^2 p \tag{2-23}$$

and the radiant intensity is

$$J(\vec{p}) = s_z \iint B(\vec{r},\vec{p})d^2r = s_z \iint B_o\left[\vec{r}-(z/s_z)\vec{p},\vec{p}\right]d^2r \qquad (2\text{-}24)$$

where $p = \sin\theta$, $p_x = \cos\theta\cos\varphi$, and $p_y = \cos\theta\sin\varphi$.

In the first order optics approximation [40], the radiometric rays can be transmitted through the system according to the following transformation rule:

$$\begin{bmatrix}\vec{r}\\ \vec{p}\end{bmatrix} = \hat{S}\begin{bmatrix}\vec{r}_o\\ \vec{p}_o\end{bmatrix}. \qquad (2\text{-}25)$$

where the 4-D column phase-space vectors with components $(x,y; p_x, p_y)$ are multiplied by the so-called *ray transfer matrix* [27]

$$S = \begin{bmatrix}A & B\\ C & D\end{bmatrix} \qquad (2\text{-}26)$$

where A, B, C, D are matrix components and

$$\det S \equiv AD - BC = 1 \qquad (2\text{-}27)$$

as a consequence of Liouville theorem [33].

For propagation through a distance in free-space in the z direction, we have

$$S = \begin{bmatrix}1 & z\\ 0 & 1\end{bmatrix} \qquad (2\text{-}28)$$

and for a thin lens, we have

$$S = \begin{bmatrix}1 & 0\\ -1/f & 1\end{bmatrix} \qquad (2\text{-}29)$$

where f is the focal length of the lens. According to Ref. [38] (also see Ref. [3]), the semigeometrical phase-space transport formula, Eq. (2-22), is preserved for all radiance definitions satisfying the three Friberg conditions [10] and for the first-order systems described by the transformation (Eq. (2-25)).

Moreover, the physical optics analog of the brightness theorem holds for paraxial optical beams transformed through any first-order optical systems, if the Fermat principle can be applied including Fresnel reflection from a locally-flat interface, and Fresnel refraction through locally flat interface.

In Ref. [11], the physical optics analog to the brightness theorem has been proven for a general class of space-invariant linear optical systems. These systems include free-space and imaging optical systems. This general formalism, based on the Radiance Transfer Function (RTF) allows the development of semigeometrical phase-space formulas not only in the first order short-wavelength approximation but also in the higher approximation orders. As an illustration of this formalism, the second order approximation will be discussed in the next section.

2.1.5 Semigeometrical Phase-Space Formulas in the Second Order Approximation and Validity of the First Order Approximation

The relation (Eq. (2-22)) represents the first order short-wavelength approximation. It transforms phase-space points from input space $(\vec{r},\vec{p})_o$ into the output space $(\vec{r},\vec{p})$. Unfortunately, this formula does not provide any criterion of validity of this asymptotic in nature approximation. In this chapter, using results of the author's paper [11], we will show that in free-space, we can define dimensionless parameter that could be used for power expansion of a system transfer function in order to evaluate the higher orders approximation as well as to evaluate the validity of the first order approximation.

The Fourier transform of Eq. (2-20) has the form:

$$\tilde{B}(\vec{f},\vec{p}) = G(\vec{f},\vec{p})\,\tilde{B}_o(\vec{f},\vec{p}) \qquad (2\text{-}30)$$

where $\tilde{B}(\vec{f},\vec{p}) = \hat{F}\{B(\vec{f},\vec{p})\}$, and G is the Radiance Transfer Function (RTF), introduced by the author in Ref. [11].

In free-space, the RTF has the form [11]:

$$G(\vec{f},\vec{p}) = \frac{1}{2}\exp\left[(-ikzs_z)\left(1-\sqrt{1-\frac{2\lambda\vec{p}\vec{f}}{s_z^2}-\left(\frac{\lambda f}{s_z}\right)^2}\right)\right] + \frac{1}{2}\exp\left[(ikzs_z)\left(1-\sqrt{1+\frac{2\lambda\vec{p}\vec{f}}{s_z^2}-\left(\frac{\lambda f}{s_z}\right)^2}\right)\right] \quad (2\text{-}31)$$

Expanding the square roots of Eq. (2-31) into a Taylor series containing powers of $\frac{2\lambda\vec{p}\cdot\vec{f}}{s_z^2}\pm\left(\frac{\lambda f}{s_z}\right)^2$, and assuming that $p/s_z = \tan\theta$ is not larger than a few units, we obtain, in the quadratic approximation, the following expression:

$$G(\vec{f},\vec{p}) = \exp\left(-i\frac{2\pi z}{s_z}\vec{p}\vec{f}\right)\cos\left\{\left(\frac{\pi z\lambda}{s_z}\right)\left[f^2+\left(\frac{\vec{p}\vec{f}}{s_z}\right)\right]\right\} \quad (2\text{-}32)$$

According to Eq. (2-22), for

$$\Phi = \left(\frac{\pi z\lambda}{s_z}\right)\left[f^2+\left(\frac{\vec{p}\vec{f}}{s_z}\right)^2\right] << 1 \quad (2\text{-}33)$$

the RTF reduces to the form:

$$G(\vec{f},\vec{p}) = \exp\left(-i\frac{2\pi z}{s_z}\vec{p}\vec{f}\right) = \hat{F}\left\{\delta\left(\vec{r}-(z/s_z)\vec{p}\right)\right\}$$

i.e., it coincides with Eq. (2-21) representing the first order approximation. In an analogous way, we can calculate the third order approximation (containing $O(\lambda^2)$ terms) and higher orders as well.

In order to evaluate the influence of the second order RTF terms, consider an example of a sinusoidal intensity distribution:

$$I(\vec{r}_o) = A\left[1+a\cos\left(2\pi\vec{f}_1\cdot\vec{r}_o+\beta\right)\right]$$

then, using Eqs. (2-20) and (2-30), we obtain

$$B(\vec{r},\vec{p}) = A\,\omega\,ls_z\,\tilde{\mu}(p/\lambda)\left[1+a\,M\left(\vec{f}_1,\vec{p}\right)\right]\times\cos\left[2\pi\vec{f}_1\left(\vec{r}-\frac{z}{s_z}\vec{p}\right)+\beta\right]$$

where M-factor has the form of cosinusoidal term in Eq. (2-32). Therefore, the radiance function still projects along straight lines defined by Eq. (2-21), with modulation, however, dependent on the spatial frequency vector $\vec{f}_1$. This result shows that the semigeometrical phase-space trace formulas can be extended beyond the first order short-wavelength approximation, the result shown first by the author in Ref. [11].

Introducing $\vec{p}\cdot\vec{f} = p\cdot f\cos\alpha$, and considering that $p = \sin\theta$, and $s_z = \cos\theta$, where θ is the angle between the z-axis and the direction of observation, we obtain,

$$\Phi = \left(\frac{\pi z\lambda f^2}{\cos^3\theta}\right)\left[1-(\sin\alpha\ \sin\theta)^2\right] \qquad (2\text{-}34)$$

where α is the angle between $\vec{f}$ and $\vec{p}$. As an example, we can consider the sinusoidal distribution of the spatial intensity distribution, illustrated in Figure 2-1, where $\vec{f}_1$ is its spatial frequency vector and $\Lambda_1 = 1/f_1$ is its spatial period. Assuming, as an arbitrary criterion, that

$$\phi \le \frac{\pi}{10} \qquad (2\text{-}35)$$

(then $\cos\phi = \cos(\frac{\pi}{10}) = 0.95 \equiv 1$), we obtain, for $\phi = \frac{\pi}{10}$, the following relation:

$$\frac{\cos^3\theta}{1-(\sin\alpha\ \sin\theta)^2} = 10z\lambda f_1^2 = W(\theta,\alpha) \qquad (2\text{-}36)$$

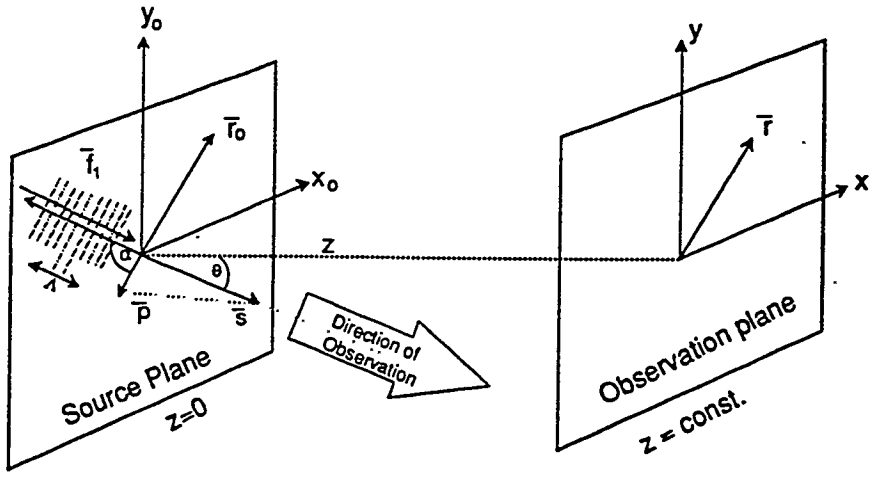

Figure 2-1
Geometry of the Diffraction System. The direction of observation is determined by the unit vector **s** situated at angle θ with respect to z axis. The vectors $\mathbf{r_o}$ and **r** are the position vectors in the planes (x_o,y_o) and (x,y), respectively. A typical sinusoidal source intensity is represented by the spatial frequency vectors $\pm\mathbf{f}_1$; $\Lambda = 1/f_1$ is the "grating constant" of this intensity distribution. The angle α is measured between the vector $\mathbf{f}_1$ and the projection **p** of the unit vector **s** onto the (x,y) plane.

This relation preserves $\phi = \text{constant} = \frac{\pi}{10}$; thus, the angular distribution $W(\theta,\alpha)$ defines the relation between W, α, θ, preserving the constant value of φ. This relation is illustrated in Figure 2-2 for only one quadrant because $W(\alpha) = W(n\pi \pm \alpha)$, where $n = 0, \pm1, \ldots$ It is seen that

$$W \leq 1 \tag{2-37}$$

Indeed, for $\alpha = \pi/2$, $W = W_{max} = \cos\theta \leq 1$. Also, for $\theta = 0$, i.e., for the normal direction,

$$W(\theta,\alpha) = W(0,0) = 1 \tag{2-38}$$

i.e., it does not depend on α. Otherwise, we have anisotropic behavior, illustrated in Figure 2-2. It should be noted that $s_z = \cos\theta$ can not be too small, otherwise the Taylor expansion does not hold. Therefore, only $\theta \leq 60°$ is illustrated in Figure 2-2.

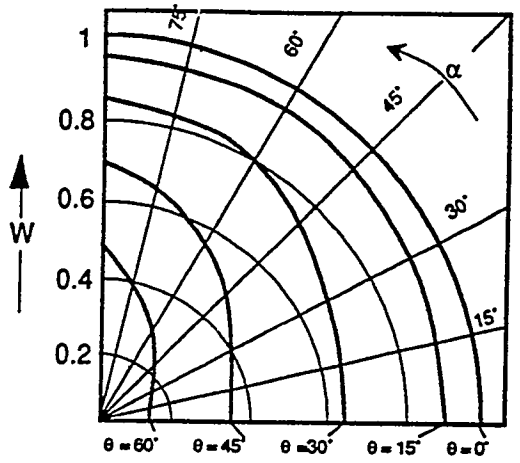

Figure 2-2
Illustration of the Relation (2-36) in Polar Coordinates (W,α) Where the Dimensionless Parameter $W = 2z\lambda f_1^2$ and α is the Angle Between the Vector $\mathbf{f}_1$ and **p**. The relation W(α) is illustrated in the range 0°-90°, for five values of observation angle θ: 0°, 15°, 30°, 45°, and 60°.

For those large θ angles, a strong anisotropic effect can be observed. For example, for θ = 60°, W increases from W = 0.13 for α = 0 to W = 0.5 for α = 90°.

Assuming W = 1, Eq. (2-36) becomes

$$z_1 = \frac{1}{10\lambda f_1^2} = \frac{\Lambda_1^2}{10\lambda} \qquad (2\text{-}39)$$

For Λ_1 = 1 mm and λ = 1 μm, we obtain z_1 = 10 cm; i.e., the radiometric ray tracing method can be used for z ≤ 10 cm; while for Λ_1 = 1 μm, z ≤ 1 mm. The other cases are also illustrated in Table 2-1.

Table 2-1. Validity of the Radiometric Ray Tracing Method (W = 1)

Λ_1	100 μm	1 mm	2 mm	5 mm	1 cm	10 cm
z_1	1 mm	10 cm	40 cm	2.5 m	10 m	1 km

It is seen that the radiometric ray tracing method is valid for quite long distances, assuming that intensity variation is not significant. This is quite often the case for many high energy conventional

and non-conventional sources, even with a high degree of spatial coherence. We illustrate this with a number of examples.

Example 1: *Poorly-Coherent High-Energy Laser Beam*

In the case of a multi-mode laser, the spatial coherence radii ρ_{coh} is frequently on the order of 100 μm, and there is an intensity variation maximum frequency on the order of a few lines per cm. Assuming $\rho_{coh} = 50$ μm and $f_1 = 5$/cm, we obtain $\Lambda_1 = 2$ mm; i.e., $\Lambda_1 >> \rho_{coh}$ and the source is quasi-homogeneous. Then, according to Table 2-1, for $z < 40$ cm the radiometric ray tracing method holds.

Example 2: *Partially-Coherent Laser Beam*

In this case, even assuming $\rho_{coh} = 1$ cm, we need to have $\Lambda_1 > 10$ cm in order to satisfy the quasi-homogeneity requirement. Assuming $\Lambda_1 = 10$ cm, we obtain from Table 2-1, $z_1 = 1$ km; i.e., the radiometric ray tracing approximation is valid for $z < 1$ km.

Example 3: *Typical Conventional Source*

In this case, $\rho_{coh} < 10\,\lambda$. Assuming $\Lambda_1 = 1$ mm, the quasi-homogeneity condition is well satisfied; then, from Table 2-1, $z_1 = 10$ cm.

Example 4: *Non-Uniform Conventional Source*

Assuming $\Lambda_1 = 100$ μm and $z_1 = 1$ mm, the radiometric ray tracing approximation only holds for very short distances ($z < 1$ mm)

These examples demonstrate that the radiometric ray tracing approximation can be used even for partially coherent laser sources, while it may not necessarily be valid for some types of conventional sources. Approximately, in order to use this method, the following two conditions need to be satisfied:

$$\Lambda_1 >> \rho_{coh} \tag{2-40}$$

and

$$\Lambda_1 > 1 \text{ mm} \tag{2-41}$$

In summary, a broad variety of fairly uniform and non highly-coherent sources, both conventional and non-conventional, satisfy the radiometric ray tracing approximation.

2.1.6 Validity of the First Order Approximation for Paraxial Optics Case

2.1.6.1 Two of Walther's Radiance Function Definitions

In the paraxial case, $s_z \cong 1$, $f << 1/\lambda$, and the coherent transfer function [44] reduces to the form:

$$H(\vec{f}') = \exp\left[ikz\left(1-\frac{(\lambda f')^2}{2}\right)\right] = \\ = \exp(ikz)\exp\left(-ikz(\lambda f')^2/2\right) = \\ = \exp ikz \ \exp\left(-i\pi z\lambda f'^2\right) \qquad (2\text{-}42)$$

Using Eq. (2-42), the RTF, is

$$G(\vec{f},\vec{p})_F = \exp\left(-i2\pi z\,\vec{p}\cdot\vec{f}\right)\cos\left(\pi z\lambda f^2\right) \qquad (2\text{-}43)$$

This result can be obtained directly from Eq. (2-32) by putting $s_z \cong 1$ and $\left|\vec{p}\,\vec{f}\right|/f^2 << 1$. Thus, the phase factor Φ (see Eq. (2-33)), describing the departure from the ray-tracing case (2-21) is

$$\Phi_F = \pi z\lambda f^2 \qquad (2\text{-}44)$$

i.e., using the second of Walther's definitions of radiance, we *do not*, in general obtain the validity of radiometric ray tracing, in the paraxial approximation. On the contrary, as was shown by Kim [24], using the first of Walther's definitions of radiance [1] in the form

$$B'(\vec{r},\vec{p}) = \text{const}\iint d^2r'\left\{u^*(\vec{r}+\vec{r}'/2)\,u(\vec{r}-\vec{r}'/2)\right\}_{ens}\exp(ik\vec{p}\vec{r}') \qquad (2\text{-}45)$$

and the Fresnel diffraction approximation, we obtain *exactly* the conventional ray tracing formula [24]. Of course, this rather surprising result does not need to have any fundamental consequences because, according to the Heisenberg uncertainty principle, the radiance function is not a measurable function. Yet, the results obtained after integration of the radiance function over either angular or space domain should be independent of the radiance function definitions. (It should be noted that in addition to the two radiance definitions presented above, Wolf et al. [38]

obtained an entire class of radiance function definitions physically identical to those above.) This problem is discussed in detail in the next section.

2.1.6.2 Comparison of Fresnel Diffraction Model with Radiometric Ray Tracing By Direct Computing

In order to verify the validity of the radiometric ray tracing approximation, independently of the definition of the radiance function, a computer modeling was performed, to compare the results for the emittance function, based either on the Fresnel diffraction integral (see, e.g., Ref. [44]), or on radiometric ray tracing (R^2T). Since radiometric ray tracing is based on the short-wavelength asymptotic formula, Eq. (2-22), it does not depend on the radiance function definition. Obviously, the Fresnel diffraction integral does not depend on the radiance function definition either. For the sake of simplicity, the 1-D diffraction model has been used.

The 1-D Fresnel diffraction integral can be presented in the form [44]:

$$U(x) = \frac{1}{i\lambda z} \int K(x, x_o; z) U_o(x_o) dx_o \qquad (2\text{-}46)$$

where U and U_o are output and input complex amplitudes, respectively, and Fresnel diffraction kernel is

$$K(x, x_o; z) = \exp\left[\frac{ik(x-x_o)^2}{2z}\right] \qquad (2\text{-}47)$$

where $k = 2\pi/\lambda$.

Using the cross-spectral density function:

$$W(x_1, x_2) = \left\{ U^*(x_1) U(x_2) \right\}_{ens} \qquad (2\text{-}48)$$

the optical intensity is

$$I(x) = W(x, x) \qquad (2\text{-}49)$$

and using Eqs. (2-46) through (2-48), the output intensity is

$$I(x) = W(x,x) = -\frac{1}{(\lambda z)^2}\iint K^*(x,x_{o1};z)K(x,x_{o2};z) \times W(x_{o1},x_{o2})dx_{o1}\,dx_{o2} \qquad (2\text{-}50)$$

In the quasi-homogeneous source approximation [7], the cross-spectral density can be presented in the form:

$$W(x_1,x_2) \equiv I\left(\frac{x_1+x_2}{2}\right)\mu(x_1-x_2) \qquad (2\text{-}51)$$

where μ is complex degree of spatial coherence. According to Ref. [44], the Fresnel diffraction approximation is valid if the following condition is satisfied:

$$z^3 >> \frac{\pi}{4\lambda}(x-x_o)^4 \qquad (2\text{-}52)$$

and the quasi-homogeneous source approximation is satisfied if

$$a >> \sigma_g \qquad (2\text{-}53)$$

where a is the characteristic length of intensity variation, where $I(x_o)$ is approximately constant, while σ_g is the characteristic size of the spatial coherence region.

The radiometric ray tracing approximation is based on the radiometric formula Eq. (2-22), and the radiometric relation for emissivity:

$$E(x) = \int B(x,p_x)dp_x \qquad (2\text{-}54)$$

where B is the radiance function and p_x is the x-component of optical direction cosines (we assume here n = constant).

In the paraxial (Fresnel diffraction) approximation, we have [7]

$$E(x) \equiv I(x) \qquad (2\text{-}55)$$

Thus, we can compare Eqs. (2-50) and (2-54), using Eq. (2-55). This approach gives us the chance to compare both theoretical models: the Fresnel diffraction model (Eq. (2-50)) and the radiometric ray tracing model (Eq. (2-54)), without using a specific definition for the radiance function. This is possible due to Eq. (2-55) and the fact that, according to Ref. [7], all definitions of generalized radiance coincide in the quasi-homogeneous source plane.

In order to compute both cases, we assume the rectangular model of the intensity distribution

$$I(x_o) = \text{rect}\left(\frac{x_o}{a}\right) \tag{2-56}$$

where the rectus function is

$$\text{rect}(\xi) = \begin{cases} 1 \text{ for } |\xi| \le 1/2 \\ 0 \text{ otherwise} \end{cases} \tag{2-57}$$

i.e., a is the size of the input slit.

We also assume the Gaussian model of spatial coherence distribution in the form

$$\mu(x') = \exp\left(\frac{-x'}{\sigma_g}\right)^2 \tag{2-58}$$

In order to evaluate the validity of the all approximation models included, we introduce four criteria (see also Section 1):

$$Q = \frac{\left(\frac{z}{a}\right)^3}{(\pi/4)\frac{a}{\lambda}\left(1+\frac{x}{a}\right)^4} >> 1 \tag{2-59a}$$

$$\frac{a}{\sigma_g} >> 1 \tag{2-59b}$$

$$\phi_F = \lambda z f^2 = \frac{\lambda}{a}\frac{z}{a} << 1 \qquad (2\text{-}59c)$$

$$\frac{\sigma_g}{\lambda} > 1 \qquad (2\text{-}59d)$$

The first criterion determines the validity of Fresnel diffraction approximation and it is obtained from Eq. (2-52) assuming $\Delta x = |a + x|_{max}$.

The second criterion determines the validity of the quasi-homogeneous source approximation and also the validity of ignoring the edges of the spatial intensity distribution ($a >> \lambda$).

The third criterion determines the validity of the R^2T model ($\phi_F << 1$).

The fourth criterion determines the partial coherence condition ($\sigma_g > \lambda$).

Using the above four criteria, the Fresnel diffraction model is compared with the radiometric ray tracing model for a variety of cases.

In the first case, illustrated in Figure 2-3, the normalized intensity/emissivity has been computed for both models, for $z/a = 10$, assuming $2\pi\sigma_g/\lambda = 20$, and $2\pi a/\lambda = 100$. Then, $Q = 4$, $a/\sigma_g = 5$, $\sigma_g/\lambda = 3.3$, and $\phi_F = 1$. Obviously, both models, R^2T and Fresnel diffraction, are not well satisfied.

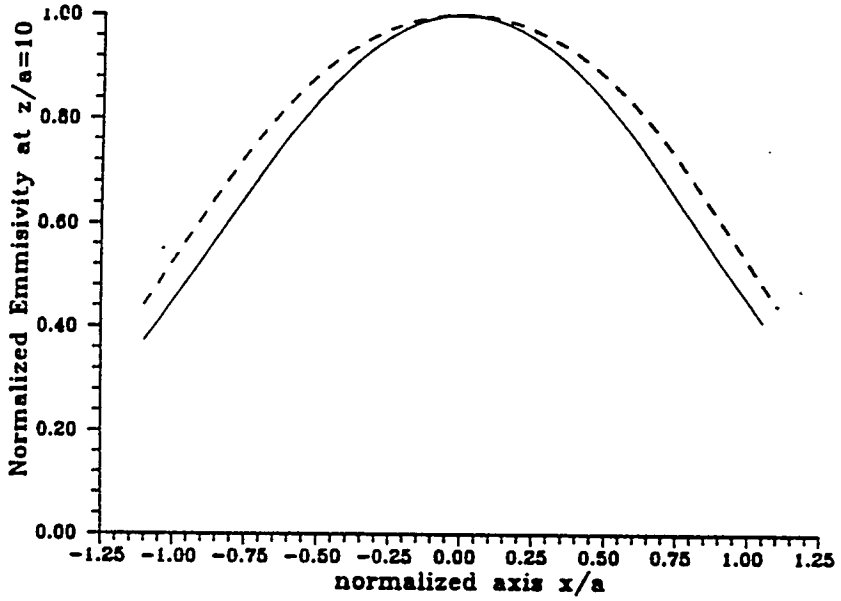

Figure 2-3
Computer Modeling of Two Approximation Models (Fresnel Diffraction - Broken Line, and Radiometric Ray Tracing - Continuous Line) for Output Intensity/Emissivity at z/a = 10 and Rectangular Input Intensity Distribution. $Q = 4$, $a/\sigma_g = 5$, $\sigma_g/\lambda = 3.3$, $\phi_F = 1$.

In the second case (Figure 2-4), for the same distance $z/a = 10$, $Q = 78$, $z/\sigma_g = 5$, $\sigma_g/\lambda = 3.3$, and $\phi_F = 12$, the Fresnel diffraction approximation is very well satisfied, but the radiometric ray tracing approximation is not satisfied. As a result, the differences between the two models are very significant.

In the third case, illustrated in Figure 2-5, the distance is larger ($z/a = 15$), and the radiometric model is even less satisfied ($Q = 264$, $a/\sigma_g = 5$, $\sigma_g/\lambda = 3$, $\phi_F = 36$). Again, the differences are very significant. In the fourth case (Figure 2-6), the situation is similar.

While in the four Fresnel diffraction cases, the radiometric ray tracing approximation was not satisfied, the next two cases satisfy both models much better. Specifically, in case 5, illustrated in Figure 2-7, $z/a = 10$, $Q = 98$, $a/\sigma_g = 5$, $\sigma_g/\lambda = 16$, and $\phi_F = 0.66$. It is seen that both models are agreeable in the central region, but the Gibbs' effect [54] creates a difference at the edges, due to relatively high spatial coherence, and relatively short distance from the input plane.

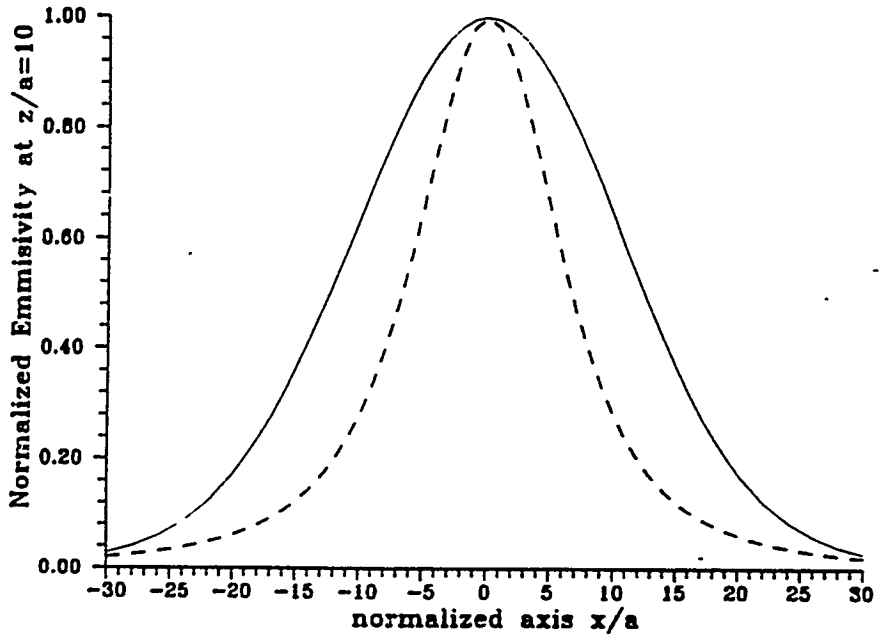

Figure 2-4
Same as Figure 2-3; $Q = 78$, $a/\sigma_g = 5$, $\sigma_g/\lambda = 3$, $\phi_F = 12$.

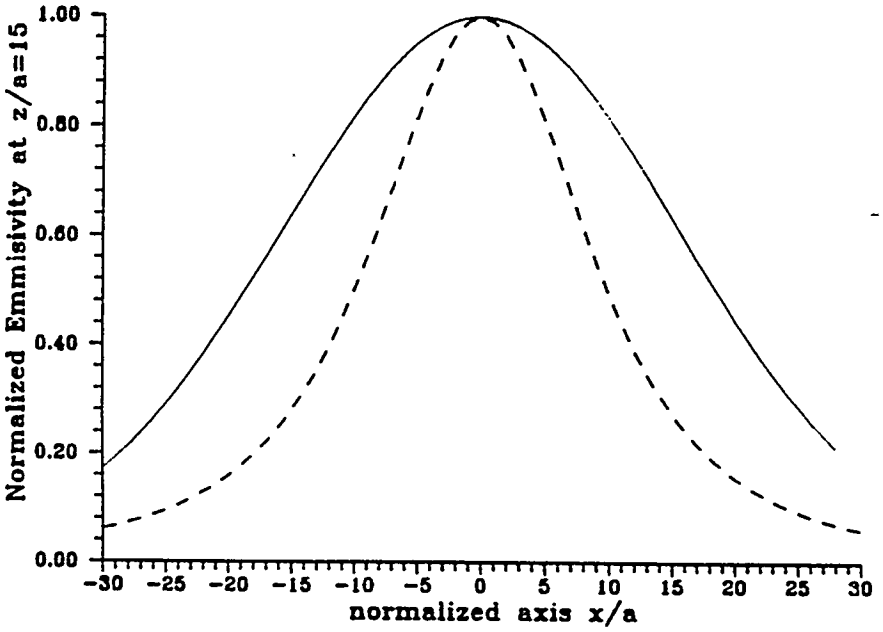

Figure 2-5
Same as Figure 2-3, but for $z/a = 15$, $Q = 264$, $a/\sigma_g = 5$, $\sigma_g/\lambda = 3$, $\phi_F = 36$.

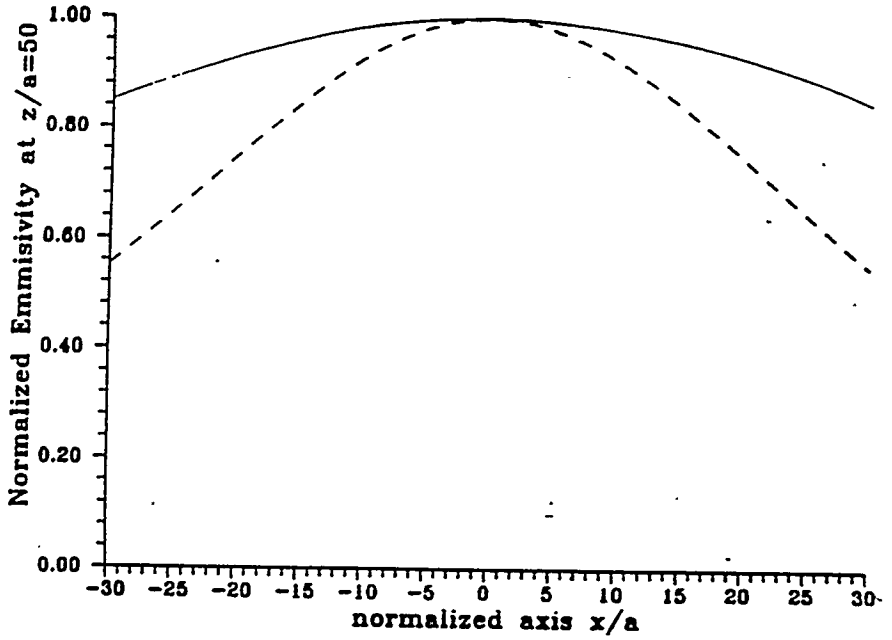

Figure 2-6
Same as Figure 2-3, but for z/a = 50, Q = 98, $a/\sigma_g = 5$, $\sigma_g/\lambda = 3$, $\phi_F = 63$.

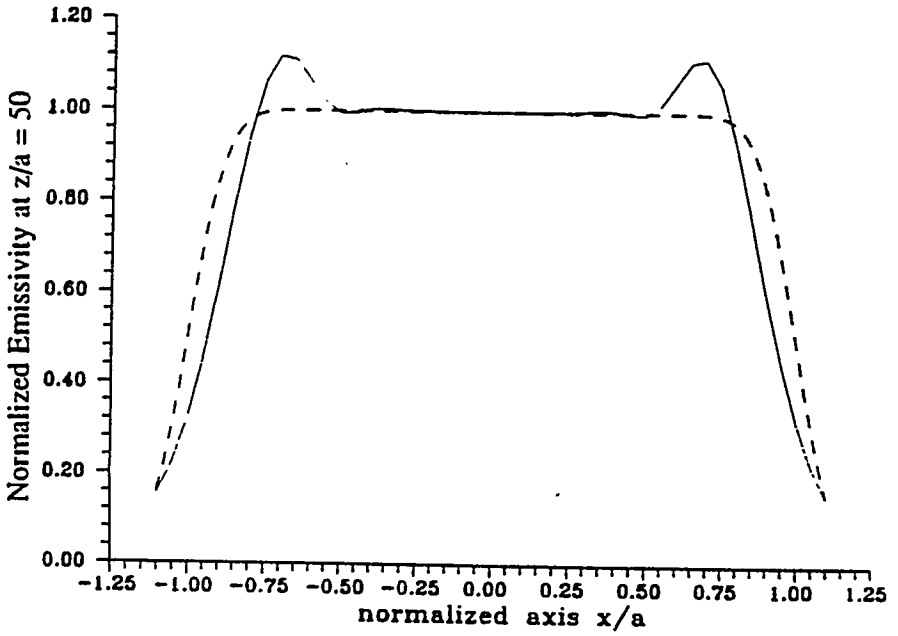

Figure 2-7
Same as Figure 2-3, but for z/a = 10, Q = 98, $a/\sigma_g = 5$, $\sigma_g/\lambda = 16$, $\phi_F = 0.66$.

In the sixth case, illustrated in Figure 2-8, the Fresnel diffraction approximation is not valid ($Q = 0.19$), but the radiometric ray tracing approximation is valid ($\phi_F << 1$). Yet the spatial coherence is high ($\sigma_g >> \lambda$), and the Gibbs effect is very significant.

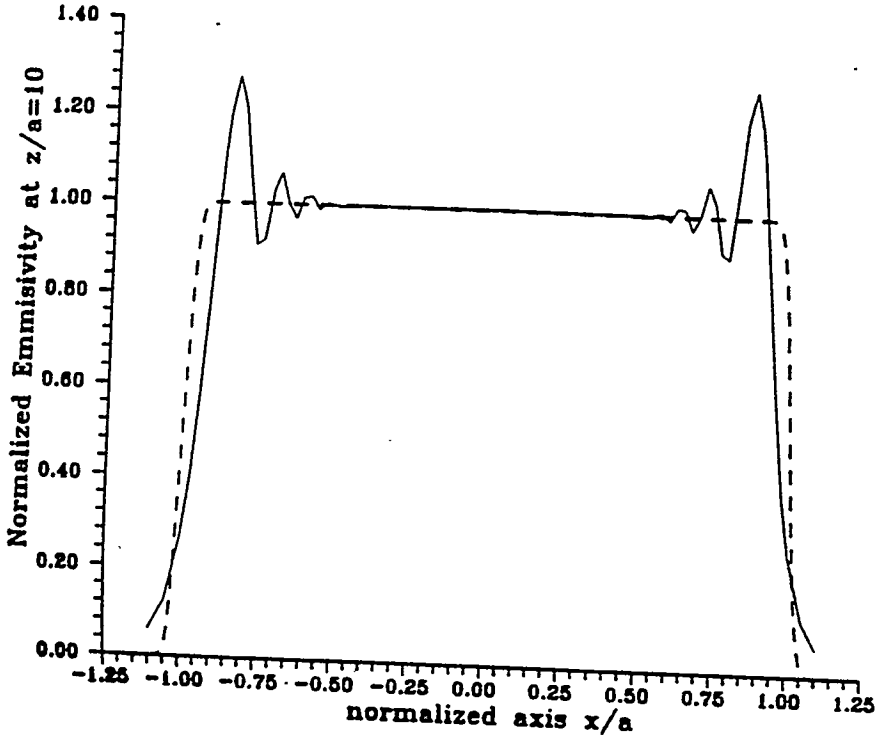

Figure 2-8
Same as Figure 2-3, but for $z/a = 10$, $Q = 0.19$, $a/\sigma_g = 5$, $\sigma_g/\lambda = 66$, $\phi_F = 0.03$.

In order to "kill" the Gibbs effect, we modify Case 5 by increasing the distance from $z/a = 10$ to $z/a = 50$. As a result, Case 7, as illustrated in Figure 2-9, demonstrates the significant improvement ($Q = 98$, $a/\sigma_g = 5$, $\sigma_g/\lambda = 16$, $\phi_F = 0.62$), but the quasi-homogeneous approximation is still poorly satisfied ($a/\sigma_g = 5$).

Finally, in Case 8, illustrated in Figure 2-10, we improve the quasi-homogeneous source approximation from $a/\sigma_g = 5$ to $a/\delta g = 25$ ($z/a = 50$, $Q = 98$, $a/\sigma_g = 25$, $\sigma_g/\lambda = 3.3$, $\phi_F = 0.62$), and, as a result, the good agreement between the Fresnel diffraction model and the radiometric ray tracing model can be observed.

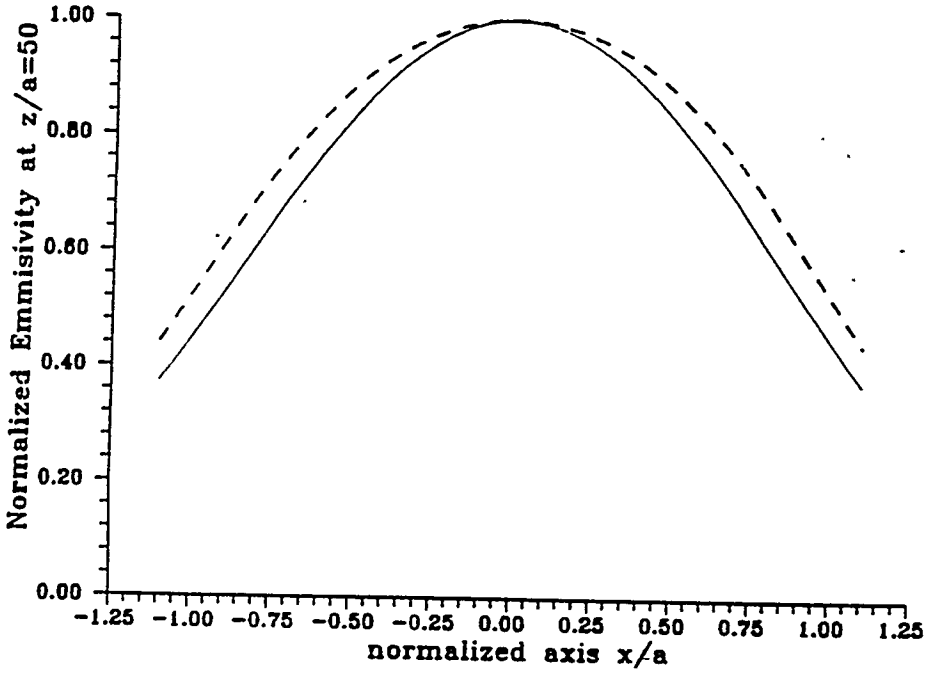

Figure 2-9
Same as Figure 2-3, but for z/a = 50, Q = 98, $a/\sigma_g = 5$, $\sigma_g/\lambda = 16$, $\phi_F = 0.62$.

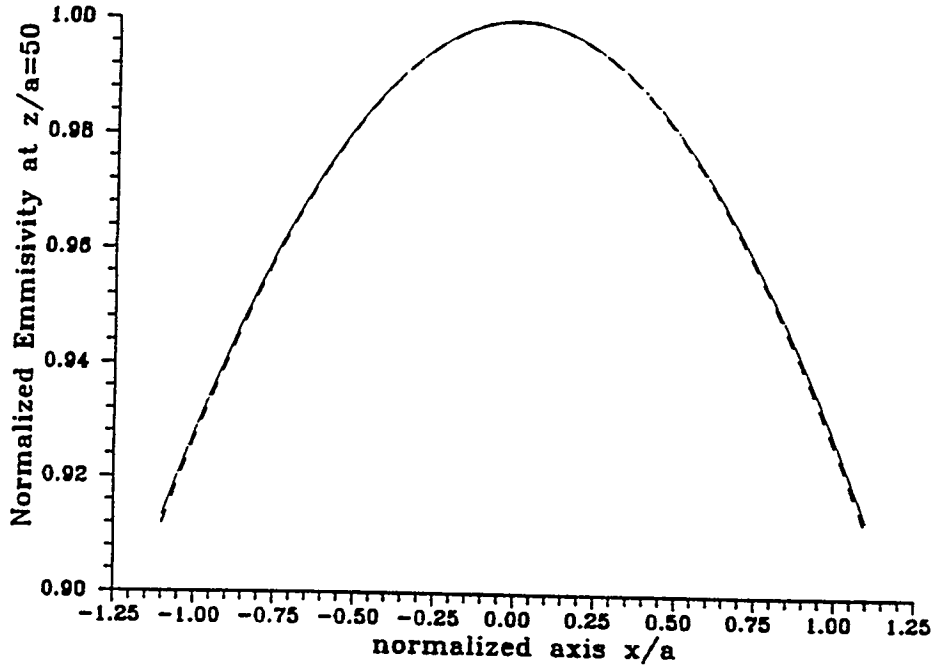

Figure 2-10
Same as Figure 2-3, but for z/a = 50, Q = 98, $a/\sigma_g = 25$, $\sigma_g/\lambda = 3$, $\phi_F = 0.62$.

The final system design is (for $\lambda = 1\ \mu m$)

$$\lambda = 1\ \mu m \quad (2\text{-}60a)$$
$$\sigma_g = 3.3\ \mu m \quad (2\text{-}60b)$$
$$a = 83\ \mu m \quad (2\text{-}60c)$$
$$z = 4\ mm \quad (2\text{-}60d)$$

The final result, illustrated in Figure 2-10, confirms our hypothesis that in order to obtain good agreement between two models (Fresnel diffraction and radiometric ray tracing), all four criteria Eq. (2-59) need to be satisfied. As a conclusion, the radiometric ray tracing method is only effective if the following criteria are satisfied:

a. Fresnel diffraction approximation (2-59a)
b. Radiometric ray tracing approximation (2-59c)
c. Quasi-homogeneous source approximation (2-59b)
d. Moderate source spatial coherence (to kill Gibbs' effect).

2.2 Selected Examples of the Applicability of the Semigeometrical Phase-Space Trajectories in Physical Optics

The semigeometrical phase-space trajectories constituting the model of radiometric ray tracing (R^2Ts) cover almost all areas of physical optics.

Based on the physical optics version of the brightness theorem as a short-wavelength asymptotic approximation of physical optics, R^2T has been applied to non-imaging optics, free-space and imaging optics. The experimental results have been provided for the phase-space effective area (PSEA) used for evaluating the global coherence of the optical beam for its evolution in phase-space. The classic Van Cittert Zernike theorem, conventionally known as determining the propagation of spatial coherence of the optical beam from the incoherent source, has been generalized for statistically-homogeneous optical fields [30]. The relations between the density matrix, radiance function, spatial coherence, and the Liouville theorem, based on a formal analogy between nonrelativistic quantum mechanics and 2-D paraxial physical optics with the z-coordinate as a parameter, are discussed in Appendix A.

The results presented in this chapter, especially in Section 2.2.1, demonstrate the potential of the R^2T method. Specifically, such result as illustrated in Figure 2-18 (see also Section 1.0) can not be obtained by any other method.

2.2.1 Non-Imaging Optics

Non-imaging optics (NIO) have been the focus of POC's R^2T model applications and are the original area which stimulated the initiation of this program. This occurred as a response to growing interest in a better understanding of the propagation of partially-coherent optical beams through large-aperture fibers and waveguides with variable cross-section, for high-energy beam transmission, collimation, and concentration. The R^2T model, presented in this section, allows us to quantitatively analyze the light sources, providing the results for all basic radiometric quantities. The model holds for partially-coherent non-Lambertian sources and anisotropic waveguide geometries.

In order to apply the R^2T model to non-imaging optics, the first step is to look at conventional geometrical ray tracing, illustrated in Figure 2-11. The second step is to apply the physical brightness theorem and, finally, to use simple integration in order to obtain the measurable radiometric quantities such as emissivity and radiant intensity. As a simple example, the truncated cone geometry illustrated in Figure 2-12 has been selected. Yet, the presented method holds for arbitrary cones with curved profiles and anisotropic cross sections. A Gaussian-correlated circular source of radius a with Gaussian intensity distribution can be presented in the form

$$I_o(\vec{r}) = \exp\left(-\frac{r^2}{2\sigma_s^2}\right)\mathrm{circ}\left(\frac{r}{a}\right); r^2 = x^2+y^2, \lambda << a \qquad (2\text{-}61a)$$

$$\mu(\vec{r}') = \exp\left(-\frac{r'^2}{2\sigma_g^2}\right); \sigma_g << \delta_s \qquad (2\text{-}61b)$$

where

$$\mathrm{circ}\left(\frac{r}{a}\right) = \begin{cases} 1 & \text{for } r \le a \\ 0 & \text{for } r > a \end{cases}$$

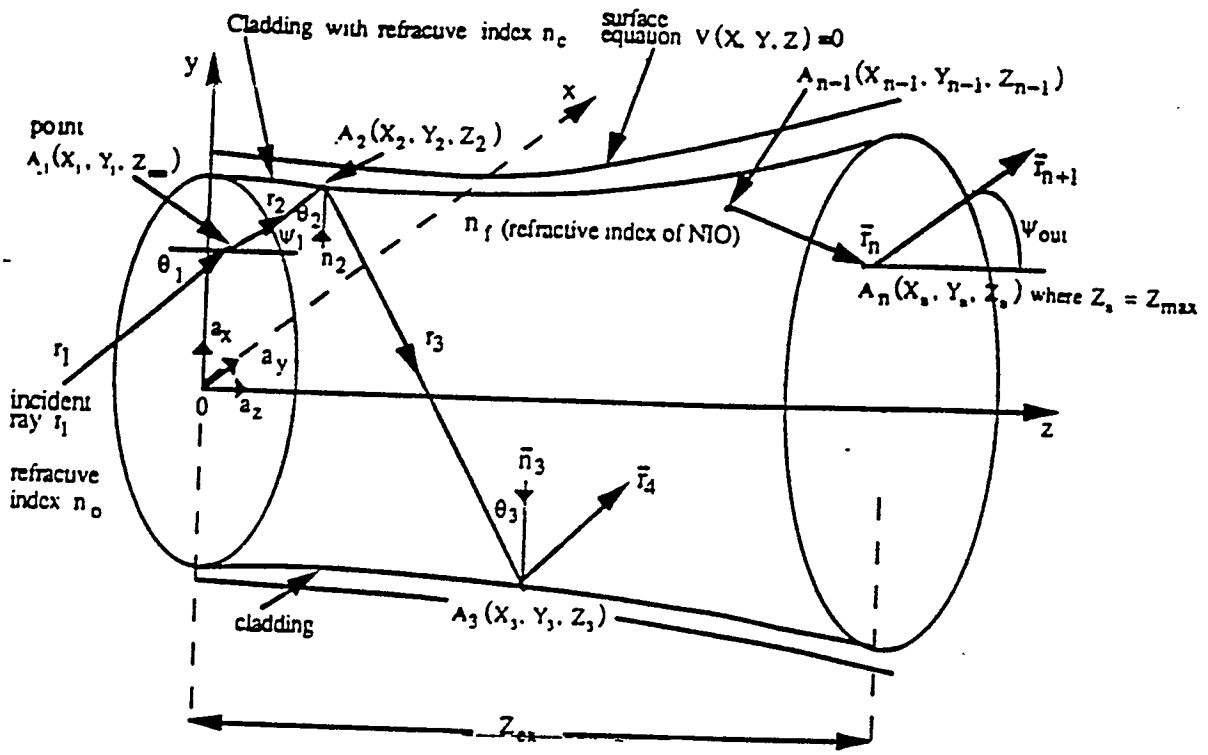

Definition of Notations:

- $V(X, Y, Z) = 0$, NIO surface equation
- n_o = refractive index outside NIO
- N_f = refractive index of NIO
- n_c = refractive index of cladding
- $\bar{r}_1$ = incident unit vector at $z = z_{min}$
- $\bar{r}_{n+1}$ = transmitted unit vector at $z = z_{max}$

Figure 2-11
Representation of NIO Surface Profile and Notations for the R^2T

Based on R^2T, the input emissivity of this source is illustrated in Figure 2-13. For the truncated cone total internal reflection (TIR) geometry, using the R^2T model, the output radiance angular distribution for $x = 0$, $y = 0$ has been computed at $z/a = 200$, for two locations, assuming no

total internal reflection (TIR) (see Figure 2-14). Assuming three TIRs, the output radiance is illustrated in Figure 2-15. It is seen that the central area is unchanged, confirming the Liouville theorem. The same distribution for a peripheral location is illustrated in Figure 2-16 for a single TIR, and in Figure 2-17 for three TIRs. Finally, the output emissivity is computed for Figure 2-18.

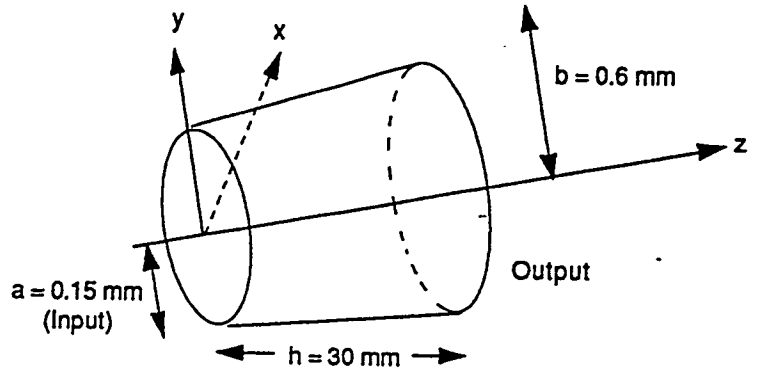

Figure 2-12
Truncated Cone Geometry

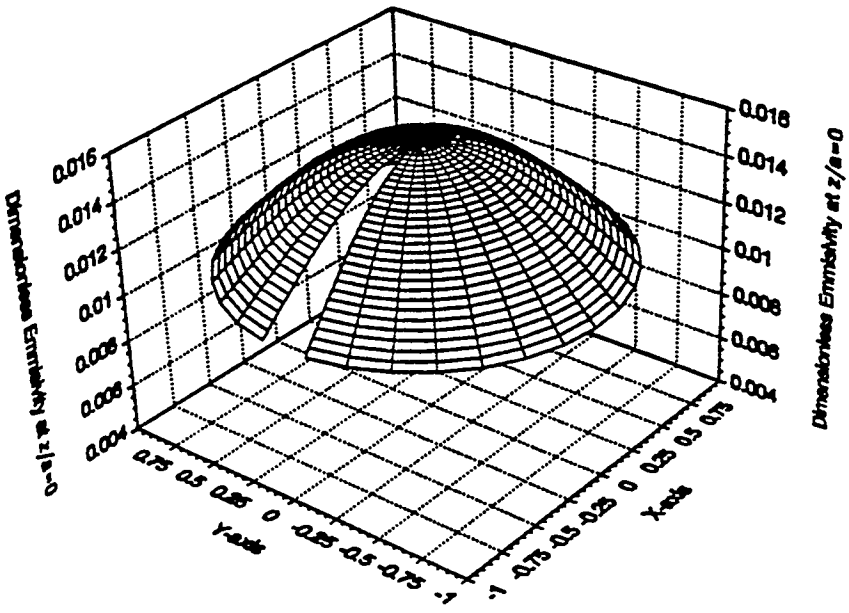

Figure 2-13
Emissivity Plot for Free-Space at z/a = 0 for a Gaussian-Correlated Circular Source of Radius a = 0.15 mm with Gaussian intensity at z/a = 0; $2\pi\sigma_g/\lambda = 20$, $2\pi a/\lambda = 1771$, $2\pi\sigma_s/\lambda = 2000$

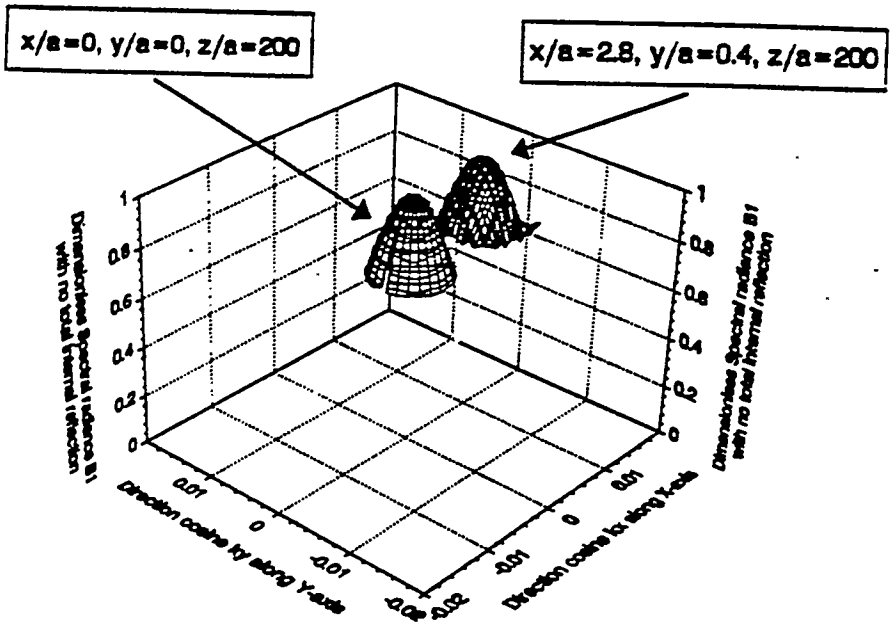

Figure 2-14
The Output of NIO Angular Distribution of Generalized Radiance at z/a = 200 for Central (x = y = 0) and Peripheral (x/a = 2.8, y/a = 0.4) Locations. The NIO geometry is a truncated cone with circular input and output radii a =0.15 mm) and b =0.6 mm, respectively, assuming no TIRs. The input is a Gaussian-correlated circular source of radius a with Gaussian intensity at z/a = 200; $2\pi\sigma_g/\lambda = 20$, $2\pi a/\lambda = 1771$, $2\pi\sigma_s/\lambda = 2000$.

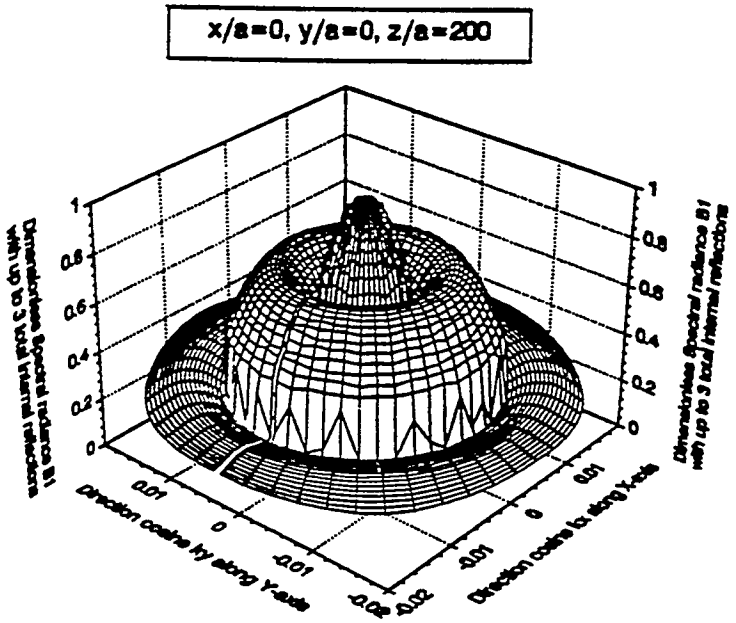

Figure 2-15
The Output of NIO Angular Distribution of Generalized Radiance at z/a = 200 for a Central Location. The NIO geometry is a truncated cone with circular input and output radii a = 0.15 mm and b = 0.6 mm, respectively assuming three TIRs. The input is a Gaussian-correlated circular source of radius a with Gaussian intensity at z/a = 200; $2\pi\sigma_g/\lambda = 20$, $2\pi a/\lambda = 1771$, $2\pi\sigma_s/\lambda = 2000$.

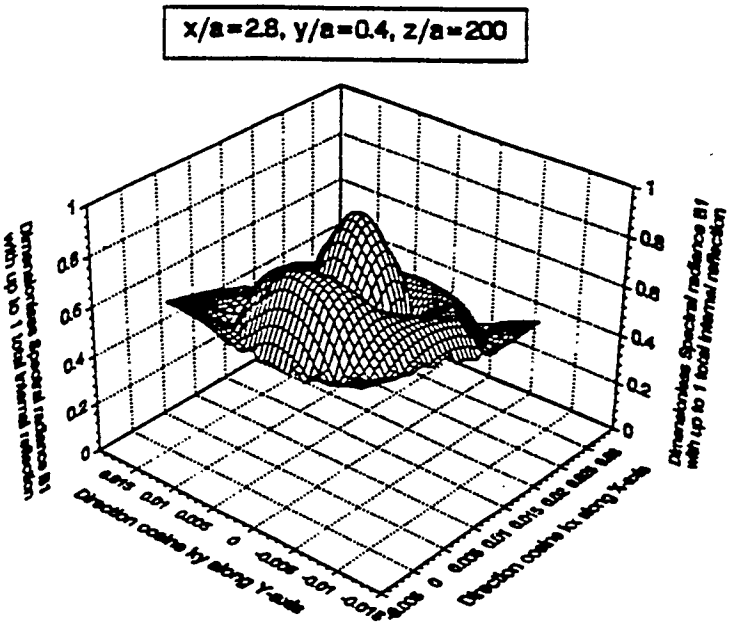

Figure 2-16
The Output of NIO Angular Distribution of Generalized Radiance at z/a = 200 for a Peripheral Location (x/a = 2.8, y/a = 0.4. The NIO geometry is a truncated cone with circular input and output radii a = 0.15 mm and b = 0.6 mm, respectively for one TIR. The input is a Gaussian-correlated circular source of radius a with Gaussian intensity at z/a = 200; $2\pi\sigma_g/\lambda = 20$, $2\pi a/\lambda = 1771$, $2\pi\sigma_s/\lambda = 2000$.

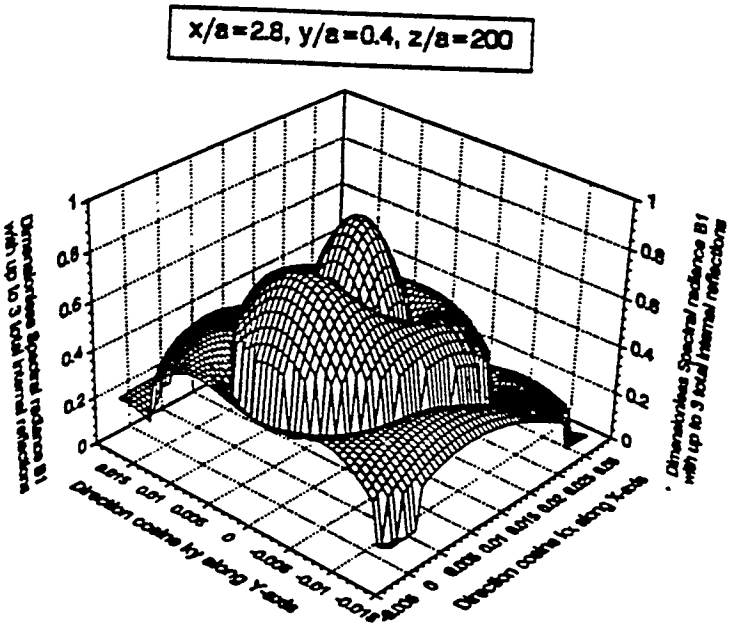

Figure 2-17
The Output of NIO Angular Distribution of Generalized Radiance at z/a = 200 for a Peripheral Location (x/a = 2.8, y/a = 0.4). The NIO geometry is a truncated cone with circular input and output radii a = 0.15 mm and b = 0.6 mm, respectively, assuming three TIRs. The input is a Gaussian-correlated circular source of radius a with Gaussian intensity at z/a = 0; $2\pi\sigma_g/\lambda = 20$, $2\pi a/\lambda = 1771$, $2\pi\sigma_s/\lambda = 2000$.

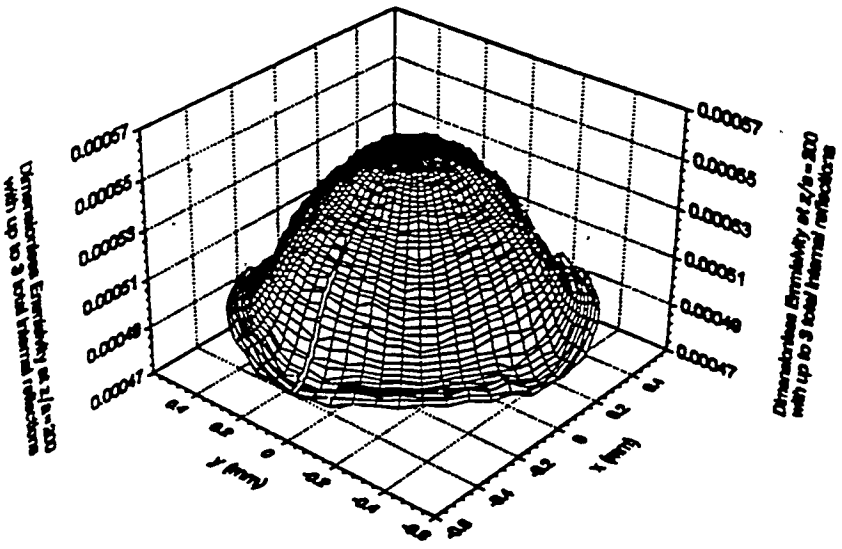

Figure 2-18
The Output of NIO Generalized Emissivity Spatial Distribution at z/a = 200. The NIO geometry is a truncated cone with circular input and output radii a =0.15 mm and b = 0.6 mm, respectively. The input is a Gaussian-correlated circular source of radius a with Gaussian intensity at z/a = 0; $2\pi\sigma_g/\lambda = 20$, $2\pi a/\lambda = 1771.574$, $2\pi\sigma_s/\lambda = 2000$. The total number of rays used up to 3 total internal reflections is 7,110,861. Peak value at (x, y) = (0, 0) is 0.00056.

Figure 2-18, also illustrated in Section 1, demonstrates the capability of the R^2T method. It is impossible to obtain this result by any other method. Even if the Fresnel diffraction approach were possible (such an approach does not yet exist), it would take a hopeless amount of computer time (even using a CRAY) to obtain this result.

2.2.2 Free-Space

The radiance angular distribution of the same source at the input plane z = 0 and at the center (x = y = 0) is illustrated in Figure 2-19 and the spatial distribution is shown in Figure 2-20. The same distribution at z/a = 200, illustrated in Figure 2-21, shows the obvious narrowing of angular size. Figure 2-22 shows the peripheral (x/a = y/a = 0.8) location.

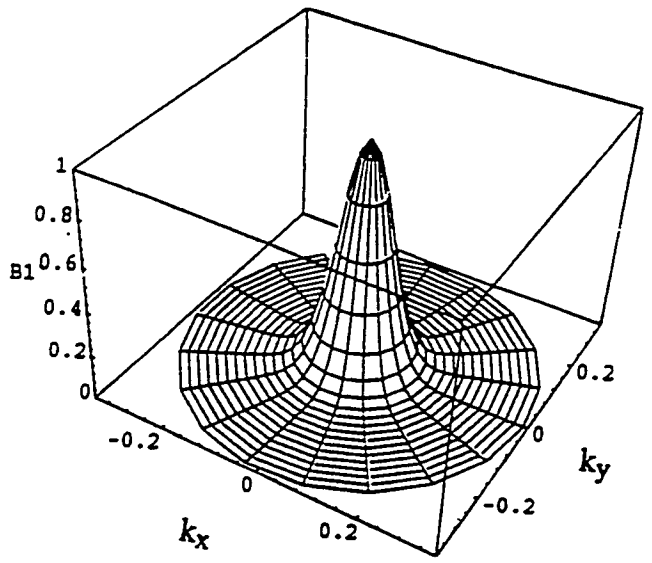

Figure 2-19
The Generalized Radiance of a Gaussian-Correlated Circular Source of Radius a = 0.15 mm with a Gaussian Intensity Profile in Free-Space. The values of the parameters are: $2\pi\sigma_g/\lambda = 20$, $2\pi a/\lambda = 177$, $2\pi\sigma_s/\lambda = 2000$, x/a = 0, y/a = 0, z/a = 0. σ_g and σ_s are the variances for spectral coherence and density, respectively. k_x and k_y are directional cosines with respect to the x and y axes, respectively.

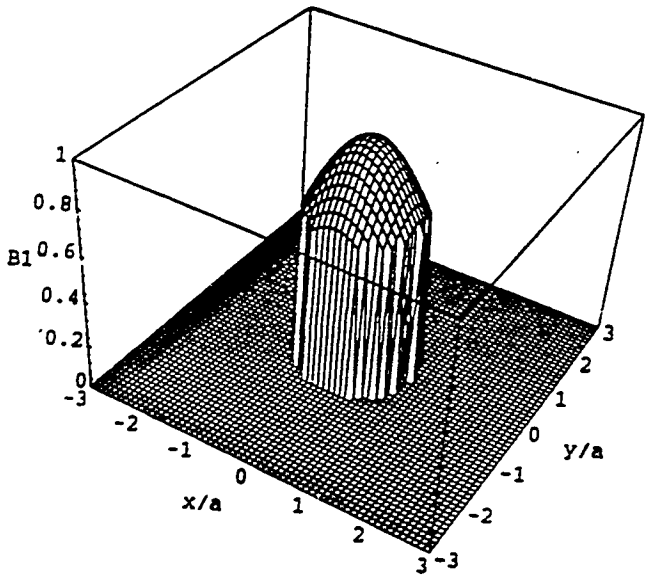

Figure 2-20
The Generalized Radiance of a Gaussian-Correlated Circular Source of Radius a = 0.15 mm with a Gaussian Intensity Profile in Free-Space of a Smaller Scale than Figure 2-13. The values of the parameters are: $2\pi\sigma_g/\lambda = 20$, $2\pi a/\lambda = 177.574$, $2\pi\sigma_s/\lambda = 2000$, z/a = 0, kx = 0, ky = 0, σ_g and σ_s are the variances for spectral coherence and density, respectively. k_x and k_y are the directional cosines with respect to the x and y axes, respectively.

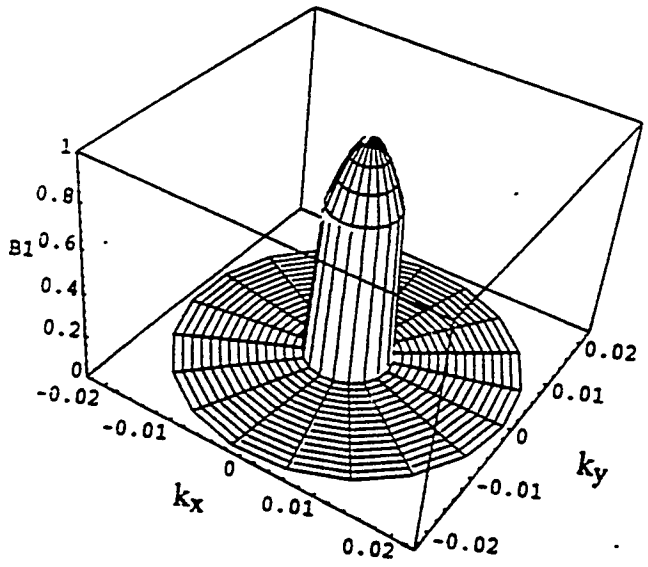

Figure 2-21
The Generalized Radiance of a Gaussian-Correlated Circular Source of Radius a = 0.15 mm with a Gaussian Intensity Profile in Free-Space. The values of the parameters are: $2\pi\sigma_g/\lambda = 20$, $2\pi a/\lambda = 177.574$, $2\pi\sigma_s/\lambda = 2000$, x/a = 0, y/a = 0, z/a = 200. σ_g and σ_s are the variances for spectral coherence and density, respectively. k_x and k_y are the directional cosines with respect to the x and y axes, respectively. Comparing this figure with Figure 2-20, an obvious narrowing of the angular spectrum can be observed.

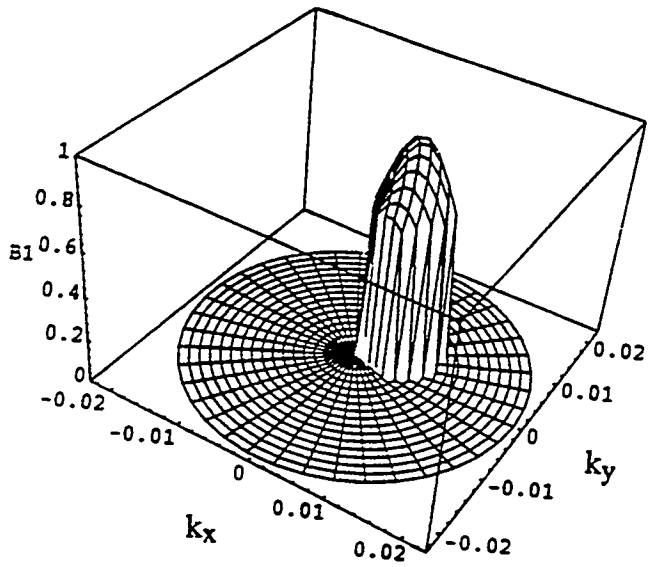

Figure 2-22
The Generalized Radiance of a Gaussian-Correlated Circular Source of Radius a = 0.15 mm with a Gaussian Intensity Profile in Free-Space at a Peripheral Location (x/a = 0.8, y/a = 0.8). The values of the parameters are: $2\pi\sigma_g/\lambda = 20$, $2\pi a/\lambda = 177.574$, $2\pi\sigma_s/\lambda = 2000$, x/a = 0.8, y/a = 0.8, z/a = 200. σ_g and σ_s are the variances for spectral coherence and density, respectively. k_x and k_y are the directional cosines with respect to the x and y axes, respectively.

The evolution of the phase-space trajectories in free-space can be computed directly on the basis of the first order optics using the (ABCD) matrix in the form:

$$\begin{bmatrix} x \\ p_x \end{bmatrix} = \begin{bmatrix} 1 & z \\ 0 & 1 \end{bmatrix} \begin{bmatrix} x_o \\ p_{ox} \end{bmatrix} \tag{2-62}$$

or

$$\begin{aligned} x &= x_o + z p_{ox} \\ p_x &= p_{ox} \end{aligned} \tag{2-63}$$

In Figures 2-23 and 2-24, the straight line in the input phase-space is transformed into the straight line in the output phase-space, according to Eq. (2-62). Finally, the output 1-D generalized emissivity spatial distribution is summarized for various distances in Figure 2-25.

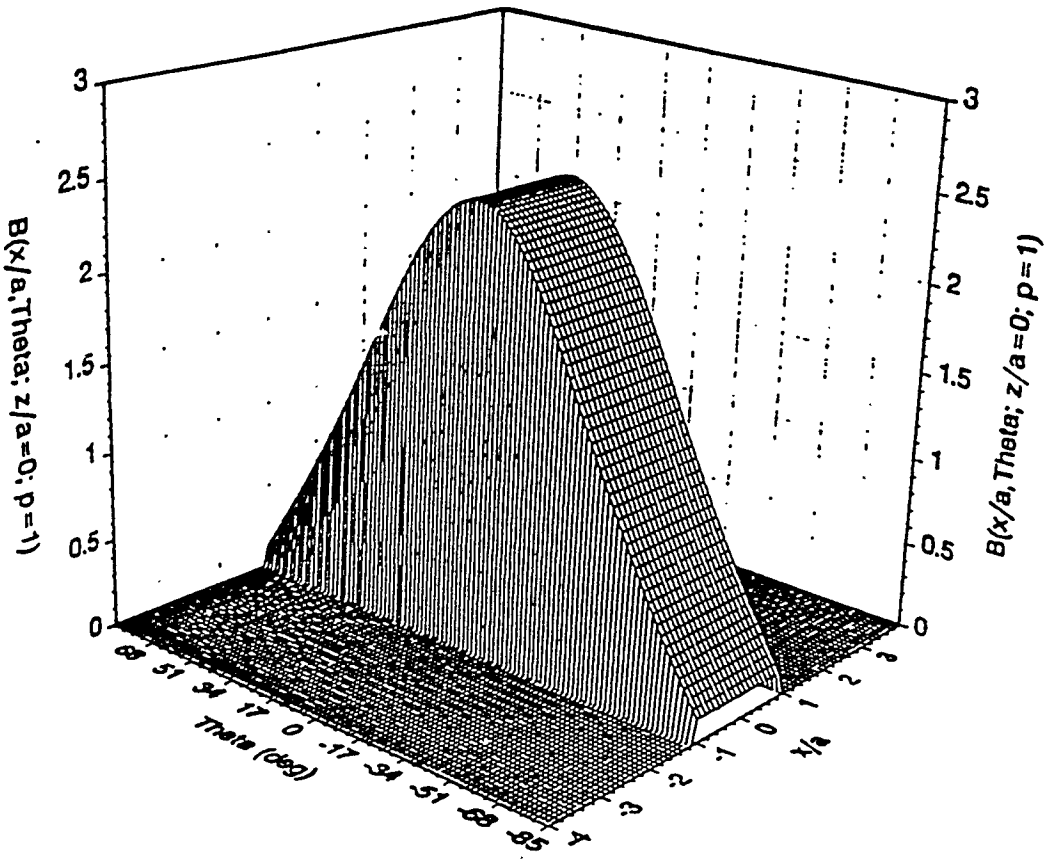

Figure 2-23
Model of Source Generalized Radiance in Phase Space for z = 0

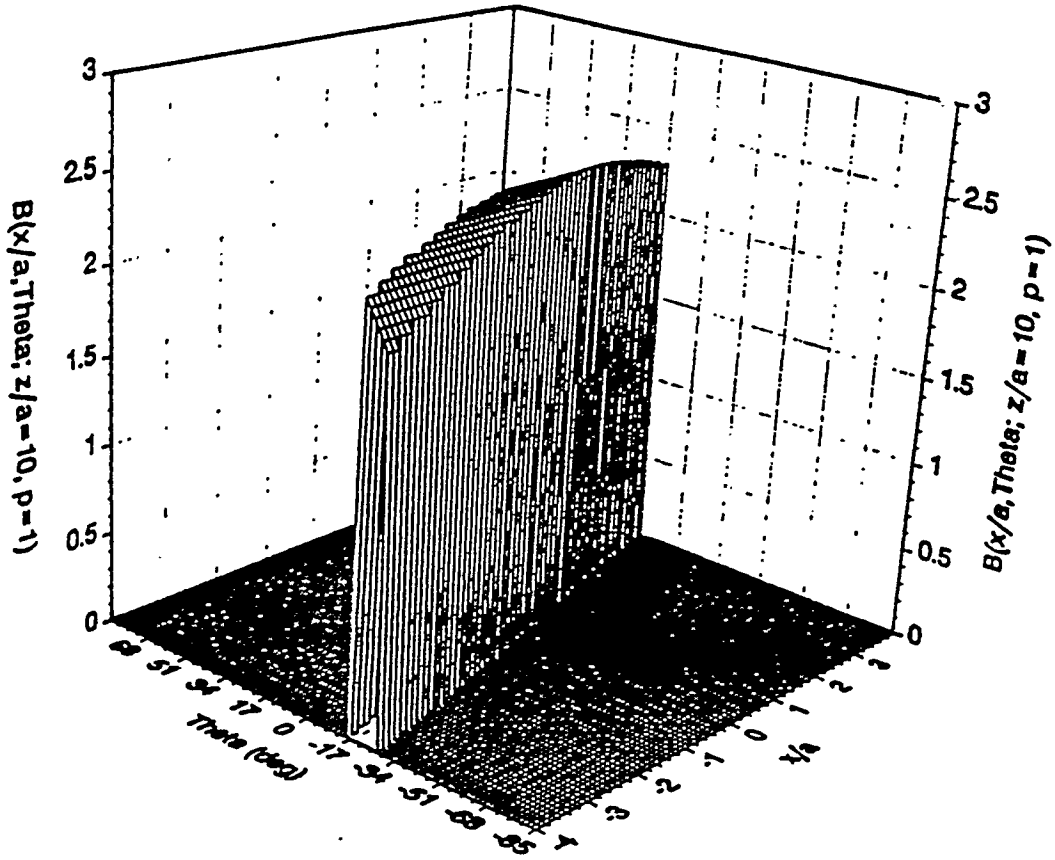

Figure 2-24
The Phase-Space Density (General Radiance) Distribution for z/a = 10. Being more general than the first-order optics model, it confirms the validity of Eq. (2-62) for this geometry.

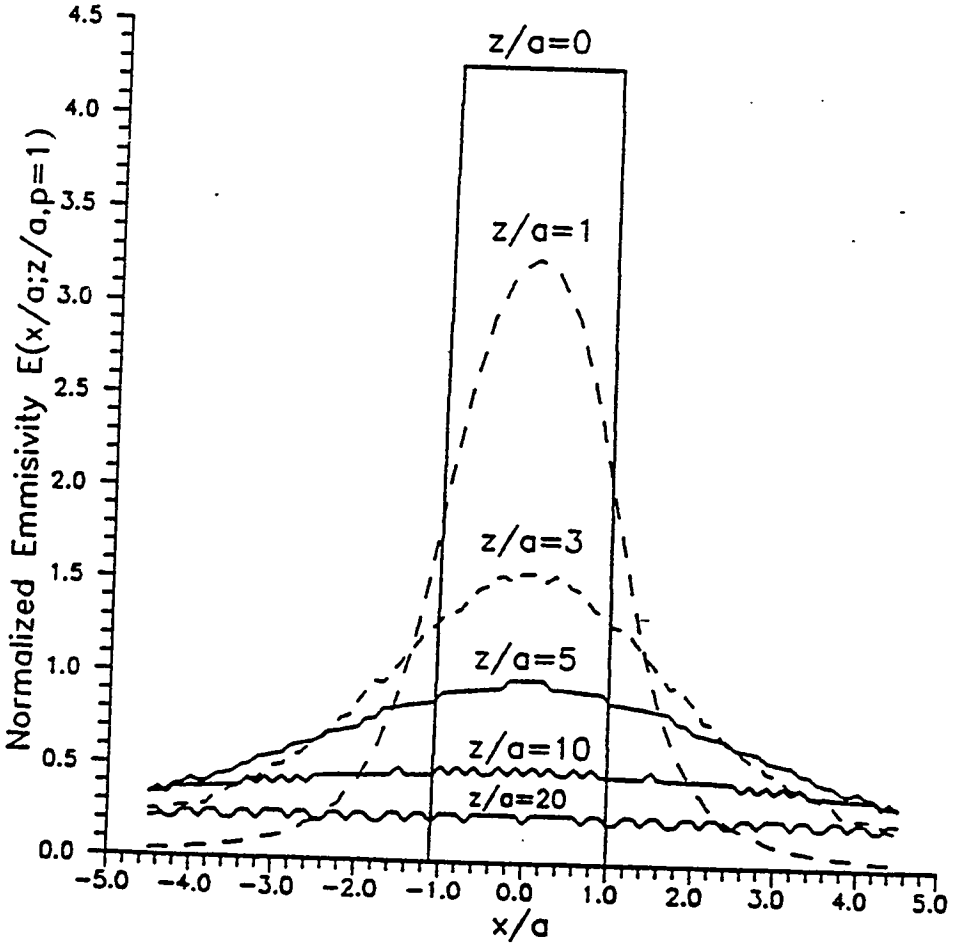

Figure 2-25
One-Dimensional Normalized Emissivity of Gaussian-Correlated Source of Uniform Intensity Located at $z/a = 0$ and $|x/a| \leq 1$.

2.2.3 Phase-Space Effective Area (PSEA)

A powerful method for optical system evaluation is based directly on phase-space trajectories:

$$q = q(z) \ , \quad p = p(z) \tag{2-64}$$

where (p,q) are generalized coordinates, either spatial (q) or related to linear momentum (p).

These trajectories describe the z-motion of the set of 4-D phase-space points characterizing the phase-space density function:

$$\rho(p, q) = \rho[p(z), q(z)] \tag{2-65}$$

The relation between generalized radiance (β) and phase-space density (ρ) is discussed in Appendix A.

According to the Liouville theorem, this function remains constant along the phase-space trajectories, i.e.,

$$\frac{d\rho}{dz} = 0 \tag{2-66}$$

It is useful to define the phase-space effective area (PSEA) A (p, q) surrounded by the phase-space boundary

$$\rho(p, q) = \text{constant} \tag{2-67}$$

i.e.,

$$A(p,q) = \oint_C d\rho dq \tag{2-68}$$

where the boundary, C, is defined by Eq. (2-67). According to the Heisenberg uncertainty principle, the PSEA cannot be smaller than the elementary cell PSEA:

$$A \geq A_0, \quad A_0 = (\Delta p dq)_0 = \lambda\!\!\!^{-2} \tag{2-69}$$

where $\lambda\!\!\!^{-} = \lambda/2\pi$. The elementary cell PSEA, A_0, can be identified as the phase-space coherent area, introduced by Kondratienko, Skrinsky [42], and Kim [24]. Using more direct reasoning, the origin of the elementary cell PSEA, A_0, can be derived from the van Cittert Zernike theorem [32], where the phase-space boundary, C_0, defined for $\rho_0 = 0.81\ \rho_{max}$, is obtained from the following relation (see Ref. [32], p. 511):

$$P_1 P_2 \frac{r_0}{R} = 0.16\lambda \tag{2-70}$$

where r_o is the source diameter, R is the distance between the source and observation plane, and P_1P_2 is the spatial coherence radius, where $\rho_o = 0.81\ \rho_{max}$; thus, the elementary area, A_o, is

$$A_o = \pi^2 (P_1 P_2)^2 \left(\frac{r_o}{R}\right)^2 = \pi(0.16)^2 \lambda^2 \cong \left(\frac{\lambda}{2}\right)^2 \qquad (2\text{-}71)$$

in agreement with Ref. [24]. As Kim [24] and Nemez [43] point out, the ratio A/A_o can be used as a criterion of global spatial coherence. Specifically, for $A = A_o$, the optical beam is fully spatially-coherent and for $A > A_o$, the field is (globally) partially spatially-coherent.

The evolution of the optical system can be monitored through observation of the phase-space boundary, C, as it changes with the z-coordinate. According to Lichtenberg [55] and Nemez [43], parallel straight-line phase-space boundaries are transformed into parallel straight-line boundaries. Also, elliptic contours are invariant [43].

The parallel line invariance has been verified by computer modeling (see Section 2.2.2). In this section, the above phase-space invariances (also related to the Poincare invariants analyzed by Jannson and Winston [34]) are based on Nemez' experimental modeling [43].

Experimental Results Based on PSEA Measuring Device

The block diagram of the PSEA-measuring device is illustrated in Figure 2-26. Using the first order optics and ABCD matrix formalism in cascade form, we obtain [43]

$$x_5 = -\frac{b}{f_o} x_o + \left(b + f_o - \frac{ab}{f_o}\right) \dot{x}_o - \frac{bf_o}{f} y_o \qquad (2\text{-}72)$$

$$y_5 = -\frac{bf_o}{f} \dot{x}_o + \left(b + f_o - \frac{ab}{f_o}\right) y_o - \frac{b}{f_o} \dot{y}_o \qquad (2\text{-}73)$$

where the parameters a, b, and f_o are defined in Figure 2-26. The optical quadrupole, twisted at 45° with respect to (x, y), is described by the following set of equations in the new twisted (x, y) coordinate system:

$$\begin{bmatrix} x_4 \\ \dot{x}_4 \end{bmatrix} = \begin{bmatrix} 1 & 0 \\ -\frac{1}{f} & 1 \end{bmatrix} \begin{bmatrix} x_3 \\ \dot{x}_3 \end{bmatrix} \tag{2-74}$$

$$\begin{bmatrix} y_4 \\ \dot{y}_4 \end{bmatrix} = \begin{bmatrix} 1 & 0 \\ \frac{1}{f} & 1 \end{bmatrix} \begin{bmatrix} y_3 \\ \dot{y}_3 \end{bmatrix} \tag{2-75}$$

where $\dot{x} = \frac{dx}{dz}$, and $\dot{y} = \frac{dy}{dz}$.

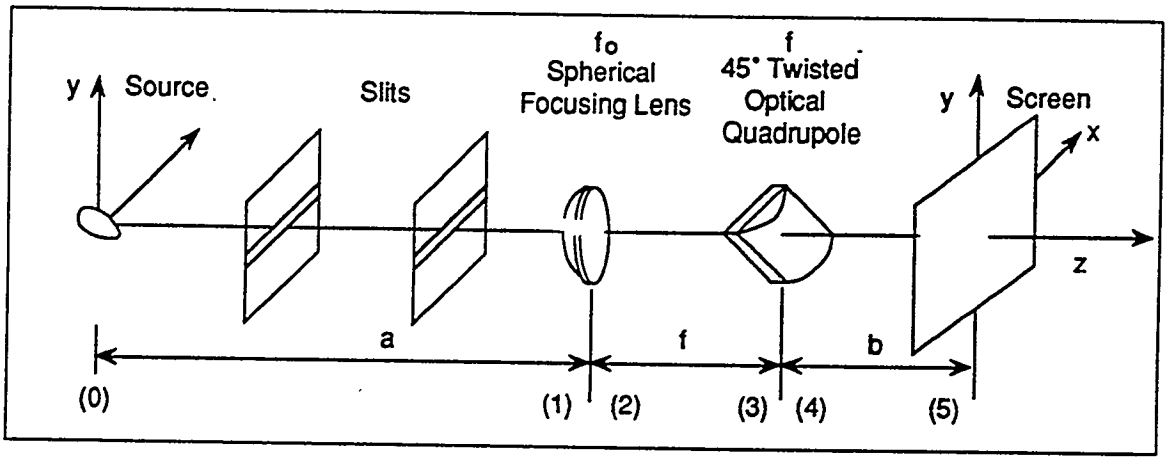

Figure 2-26
Block Diagram of the PSEA-Measuring Device

Two slits secure the narrow angular spectrum in the y-direction.

Setting the second terms in Eqs. (2-72) and (2-73) to zero gives

$$b + f_o - \frac{ab}{f_o} = 0 \tag{2-76}$$

The third terms are automatically zero ($y_o = 0$, $\dot{y}_o = 0$) because of the two horizontal slits, illustrated in Figure 2-26. We obtain

$$x_5 = -\frac{b}{f_o} x_o \tag{2-77a}$$

$$y_5 = -\frac{bf_o}{f}\dot{x}_o \tag{2-77b}$$

i.e., indeed, the phase-space coordinates $(x_o, \dot{x}_o)$ are displayed on the screen (x_5, y_5); i.e.,

$$(x_o, \dot{x}_o) \Rightarrow (x_5, y_5) \tag{2-78}$$

Eqs. (2-70) to (2-78) show that the proposed device indeed measures the PSEA.

A schematic of the PSEA-measuring device is illustrated in Figure 2-27. Such a device can be used for monitoring phase-space diagrams and phase-space trajectories [56]. The design parameters are

$$f_o = 184 \text{ mm} \tag{2-79a}$$
$$f = 65 \text{ mm} \tag{2-79b}$$
$$\text{Slit Width} \equiv 0.5\ \mu\text{m} \tag{2-79c}$$
$$\text{Second Slit Near Plane (1)} \tag{2-79d}$$
$$\text{(0) - source plane} \tag{2-79e}$$
$$\text{(5) - phase-space monitoring screen} \tag{2-79f}$$
$$b(a - f_o) = f_o^2 \tag{2-79g}$$
$$a > f_o \tag{2-79h}$$

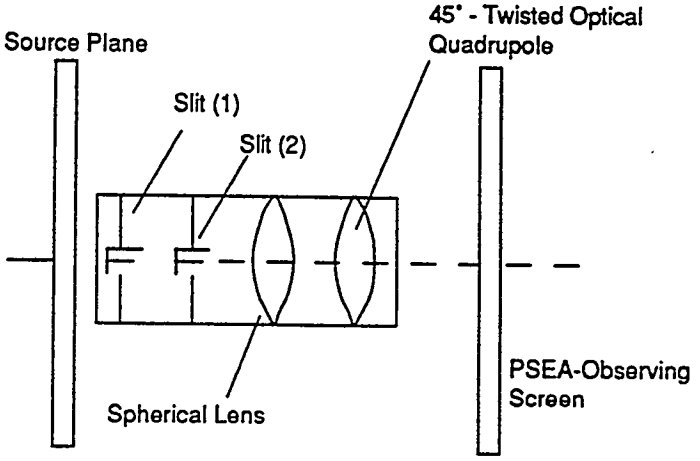

Figure 2-27
Schematic of the PSEA-Measuring Device. Such a device can be used for monitoring phase-space diagrams and phase-space trajectories as a function of z-coordinate.

In Figure 2-28, a 1-D point source is illustrated in phase-space for three different z-distances. It is seen that the characteristic rotation of the PSEA is similar to those illustrated in Figures 2-23 and 2-24.

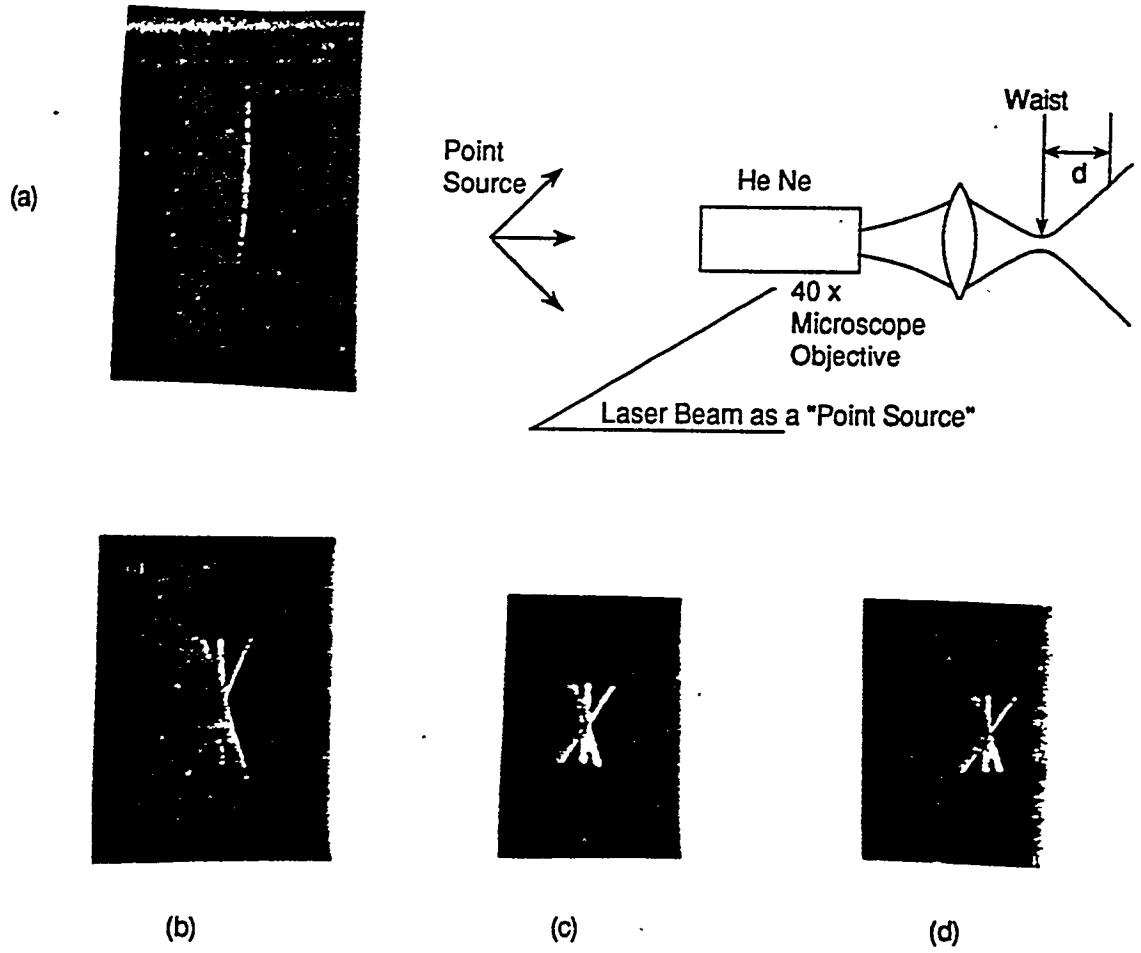

Figure 2-28
Experimental Results for the PSEA of the 1-D Point source (a) at Three Different Free-Space z-Distances (z = 0) (b), 183 mm (c), 396 mm (d)). The point source is a laser beam.

2.2.4 Imaging Optics

Using the PSEA method, we can also experimentally illustrate the phase-space trajectories for paraxial and non-paraxial (aberrated) imaging optical systems; see Figure 2-29. The illustration of comatic aberration in phase-space is presented in Figure 2-30.

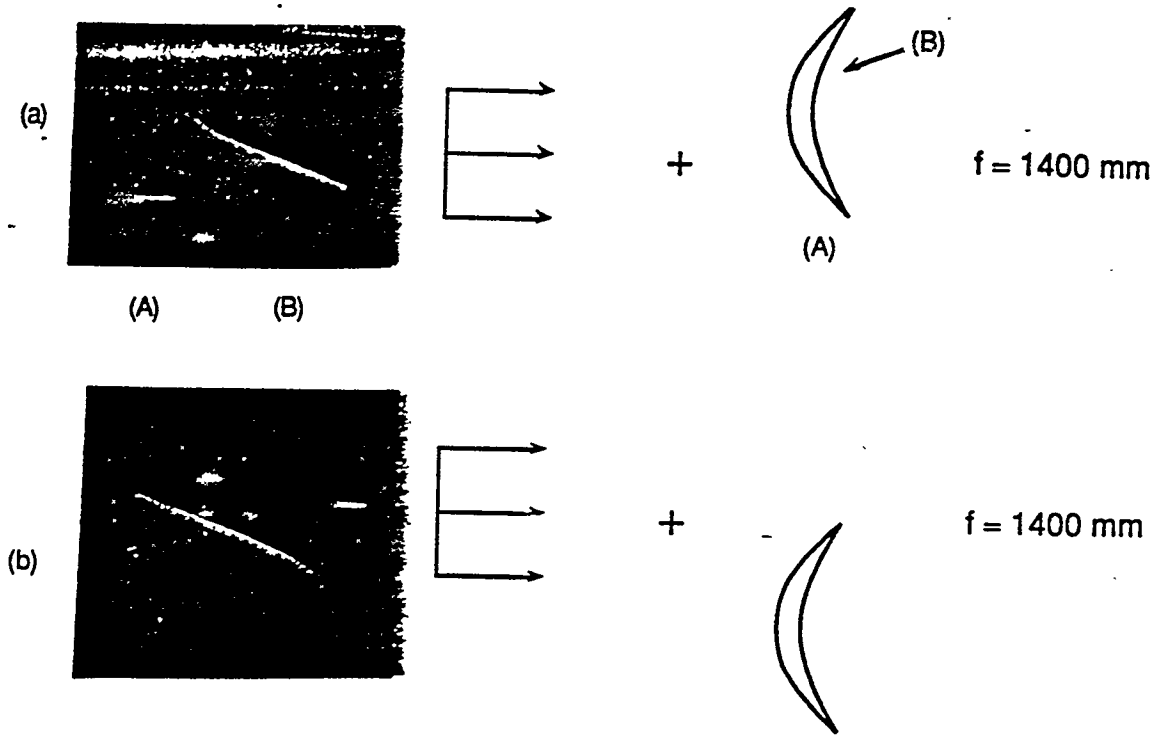

Figure 2-29
Experimental Results for the PSEA of the 1-D Plane Wave, Partially Transformed by a Lens with Nondeformed Wavefront (A) and Deformed Wavefront (B) by a Lens at the Top (a) and at the Bottom (b)

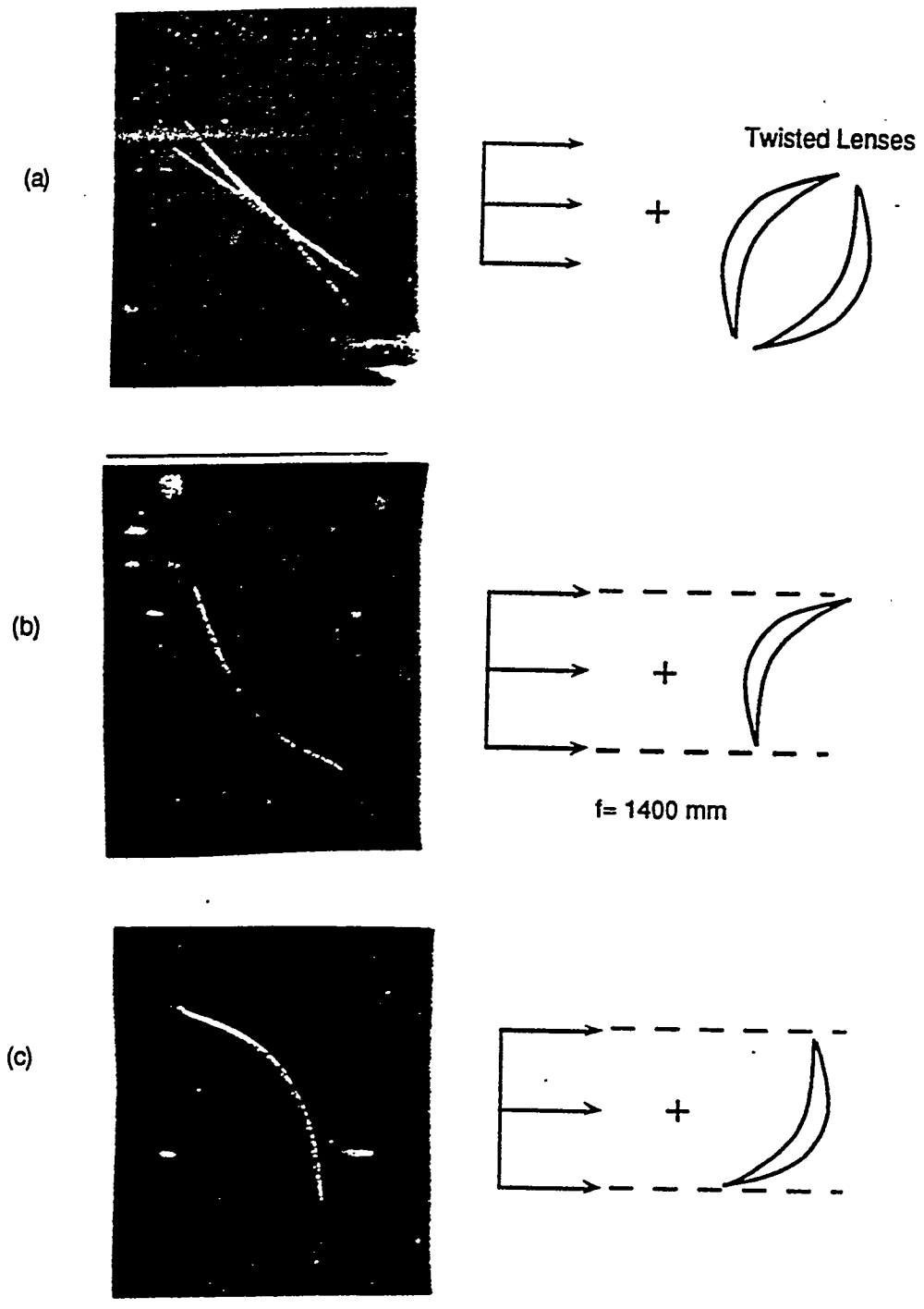

Figure 2-30
Illustration of Comatic Aberration in Phase Space Obtained with (a) Two Twisted Lenses, and (b) and (c) a Single Twisted Lens

2.3 Comparison of Computer Time Budget Between the R²T Model and the Fresnel Diffraction Model

This section considers the possibility of comparing the radiometric (ray-tracing) approximation with the results of direct integration of the propagation equation based on the cross-spectral density (see also Section 1):

$$I(\vec{r}) \propto \iiiint W(\vec{r}_{o1},\vec{r}_{o2})\, K^*(\vec{r};\vec{r}_{o1}) K(\vec{r};\vec{r}_{o2}) d^2r_{o1}\, d^2r_{o2} \qquad (2\text{-}80)$$

where $W(\vec{r}_1,\vec{r}_2)$ is the cross-spectral density, $I(\vec{r})$ is the intensity at a point $\vec{r} = (x,y)$ in the z plane and $\vec{r}_{o1} = (x_{o1},y_{o1})$ and $\vec{r}_{o2}$ are points in the source plane ($z = 0$). K is the diffraction kernel, given for the Fresnel case as

$$K(\vec{r};\vec{r}_o) = \exp(ikz) \exp \frac{ik}{2z}\left[(x-x_o)^2 + (y-y_o)^2\right] \qquad (2\text{-}81)$$

Eq. (2-80) is a four-dimensional integral, which must be performed at each point P in the plane at z.

It is logical to begin this process by examining to the artificial two-dimensional case, in which the source is assumed to be fully coherent (constant phase) and to have infinite extent in the y-direction, but to have a finite coherence length and finite extent in the x-direction. For the 2-D case, Eq. (2-80) becomes

$$I(x) \propto \iint W(x_{o1},x_{o2}) K^*(x;x_{o1}) K(x,x_{o2}) dx_{o1}\, dx_{o2} \qquad (2\text{-}82)$$

where x is the location in the z plane and x_{o1}, x_{o2} are points in the source plane. The 1-D Fresnel kernel is then

$$K(x,x_o) = \exp(ikz) \exp\left[\frac{ik}{2z}(x-x_o)^2\right] \qquad (2\text{-}83)$$

This is a two-dimensional integral for each x in the z plane, and is a completely tractable problem. In the present context, the analysis should start with the problem of a Gaussian source profile I(x) (with σ_I corresponding to the electron beam spatial distribution) with a Gaussian cross-spectral density function. That is,

$$W(x_1,x_2)=\left[I(x_1)I(x_2)\right]^{1/2}\mu(x_1-x_2) \tag{2-84}$$

where μ is a Gaussian with σ_g corresponding to the Gaussian sum of electron beam and single-electron radiation divergences. The quasi-homogeneous assumption takes the form $\sigma_g << \sigma_I$. We can compare the results of Eq. (2-82) with the ray-tracing method for a large range of the ratio σ_I/σ_g in order to determine the range of applicability of the ray-tracing method, that is, the real limits of the quasi-homogeneous assumption.

The 2-D problem is convenient for performing large numbers of comparisons, but the results of the 2-D analysis must be validated with results from the full 3-D problem. We present an analysis for the condition, appropriate for synchrotron radiation, that the source is statistically homogeneous. (The Gaussian cross-spectral density, generalized to 3-D from the above, is a special case of this.) Eq. (2-80) may be rewritten as

$$I(\vec{r}) \propto \int_{-\infty}^{\infty} dx_{o1} \int_{-\infty}^{\infty} dy_{o1} \int_{x_{o1}-\Delta x_{12}/2}^{x_{o1}+\Delta x_{12}/2} dx_{o2} \int_{y_{o1}-\Delta y_{12}/2}^{y_{o1}+\Delta y_{12}/2} dy_{o2} \left[I(\vec{r}_{o1})I(\vec{r}_{o2})\right]^{1/2} \mu(\vec{r}_{o1})\mu(\vec{r}_{o2})K^*(\vec{r};\vec{r}_{o1})K(\vec{r};\vec{r}_{o2}) \tag{2-85}$$

where Δx_{12} is the range of $x_1 - x_2$ over which g is nonzero, and similarly for Δy_{12}. The integral may be approximated by a sum over discrete values of the four variables of integration. To determine how many times the integrand must be evaluated, the needed fineness of the discretization must be calculated.

The discretization of the variables of integration is determined both by the shapes of I and g and by the rapidity of variation of the kernel. If δx_1 represents the separation of adjacent discrete values of x_{o1}, then the latter consideration requires

$$\delta x_1 << \frac{\lambda z}{2\pi(x_{o1}-x)} \tag{2-86}$$

This ensures that the kernel varies only slowly from one value of x_{o1} to the next. Similar constraints apply to y_{o1} and y_{o2}.

Consider numbers appropriate for the propagation of undulator radiation. Take $\sigma_x = \sigma_y = 0.2$ mm, $\lambda = 1000$ Å, $\Delta x_{12} = \Delta y_{12} = 30$ μm, and $z = 10$ m. Then the discretization interval is $\delta x_1 = 80$ μm at $x = 0$ (case A) and 1.6 μm at $x = 1$ cm (case B), assuming that the kernel is allowed to vary by 10% between discrete values of x_{o1}.

In case A, the kernel variation is sufficiently slow that the discretization of x_{o1} is in fact determined by the shape of I, so 80 μm is too large and Δx_1 should be more like 20 microns to capture the source profile. Correspondingly, Δx_2 should be on the order of 3 μm. The calculation of the intensity at $x = 0$ will then require (assuming the integration over x_{o1} and y_{o1} cover two σ_x) $(20)^2(10)^2 = 40{,}000$ evaluations of the integrand. The calculation at $x = 1$ cm will require $(250)^2\,(20)^2 = 2.5 \times 10^7$ evaluations since it is a more rapidly varying kernel.

The evaluation of the integral will be speeded up if the terms in the integrand are precomputed and stored in tables for look up during the summation. If tables are created for the values of I, μ, $\exp (ik/2z)(x - x_{o2})^2$ and $\exp (ik/2z)(y - y_{o2})^2$, then each evaluation of the integrand will require a square root, six complex multiplications, and a complex addition. A 10 Mflop machine will require of order one minute to perform the integration at $x = y = 1$ cm. Assuming conservatively that the average time of integration is one minute per point in the z plane, a 30×30 profile would be obtained in 900 minutes or 15 hours. Using similar assumptions, the corresponding simplified 2-D problem would execute in a fraction of a minute.

The computation was performed using three computers: a Sparc Station 1+, a Cray Y-MP and an Everex PC 486/33 MHz. The integral is performed by using the extended Simpson's rule, doubling the number of points until the relative tolerance of 10^{-6} is reached. The results are given in Table 1-2 in Section 1. It is seen that the difference in duration of computer use is quite significant, up to almost three orders of magnitude for the Everex PC 1-D case. It should be emphasized that such a comparison can be made only for free-space and first order optics. Otherwise, the problem is too sophisticated to apply to the Fresnel diffraction model (see Table 1-2 in Section 1).

Here, $X_o = x_o/a$, $X_1 = x_1/a$, $X = x/a$, $Z = z/a$, $p = \dfrac{2\pi\sigma_g}{\lambda}$, $p_1 = \dfrac{2\pi a}{\lambda}$, E is the output emissivity, and the source model is described by Eq. (2-61) for $\delta_s = \infty$. It is seen that saving time by the use of a supercomputer (Cray) or workstation (Sun) is problematic since no special programming has been done. The issue here, however, is saving time on the same computer when using the R^2T instead of the conventional Fresnel diffraction approach, as illustrated in Table 2-2.

Table 2-2 Comparison of Time Budgets for Three Computers/Software

X	Y	p	p_1	E(XYZ;p,p_1)	Sun (sec) (Fortran)	Cray (sec) (Fortran)	PC 486/33 MHz (sec) (MS Basic 7.1)
0	50	20	500	0.19257	10.2	0.605	6.1
0	10	400	2000	0.03146	616	34.7	96
0.5	10	400	2000	0.03136	741	41.8	96

The 1-D Fresnel diffraction integral was computed at USC using a 64-bit word size. The values of the integrals are given for each case together with the computational time (CPU seconds) for the three machines, Sun, Cray, and 486 PC.

2.4 Formal Analogy Between Paraxial Optics and Non-Relativistic Quantum Mechanics

Using the formal analogy between monochromatic paraxial optics and non-relativistic quantum mechanics, developed by Marcuse [48] and Eichmann [49], and discussed in Appendix A, we can better understand statistical optics as an analogy of statistical "mixed states" in non-relativistic quantum mechanics. It is seen that the z-coordinate in paraxial optics is equivalent to the t-coordinate in non-relativistic quantum mechanics. Therefore, only 2-D quantum mechanics can be compared to an analogous optical problem. Specifically, such essentially 2-D quantum mechanical problems as Multi-Quantum-Well (MQW) problem can be traced to analogous optical problems by comparison of 2-D potential energy V (x,y) with the analogous 2-D spatial index distribution:

$$V(x,y) \rightarrow -n(x,y) \tag{2-87}$$

Also, the optical analog of the Liouville theorem can be derived from the density matrix motion equation by identifying the optical density matrix with cross-spectral density (see Appendix A).

This formal analogy was exploited in this program to better understand the semi-geometrical phase-space trace formulas as an optical analog of semiclassical phase-space trace formulas in quantum mechanics, developed to investigate the spectra of quantum-mechanical systems when the classical dynamics is non-integrable [41].

2.5 DOE-Related Applications of Semigeometrical Phase-Space Trace Formulas

The focus of a comprehensive review of DOE-related applications was on synchrotron radiation. Other applications include Schell model beams that cover quasi-homogeneous sources as well as fully coherent laser radiation. Obviously, those beams have many energy related applications since they include the vast majority of laser sources--semiconductor laser diodes, free-electron lasers, solid state lasers, and many others. Using the analog of the van Cittert Zernike theorem for statistically homogeneous wave fields allows investigation of the propagation of spatial coherence in time and space, when the boundary conditions can be ignored. Also, holographic systems have been used in many DOE programs, including x-ray holography [80,82,83], solar physics [84], and plasma diagnostics [85]. The radiation/heat transfer problems that can be treated by the R^2T method are also discussed in this chapter.

2.5.1 Synchrotron Radiation

By synchrotron radiation we mean radiation emitted by an electron beam passing through a bending magnet, wiggler or undulator. Comprehensive reviews are given in Refs. [46, 71-73]. Synchrotron radiation is characterized by small source size (of order 1 mm); low beam divergence (of order 1 mr); high average power (up to tens of kW for bending-magnet radiation; tens of watts for undulator radiation); and linear polarization (helical undulators produce circular polarization). The radiation from bending magnets and wigglers is broadband, peaking typically in the x-ray region but extending through the visible and into the infrared. Undulators (which consist of a large number [say, 30] of wiggling magnets in series) produce narrowband output via constructive interference from the individual wigglers; this is analogous to the operation of a multilayer interference filter or of a phased-array linear antenna. Undulator output may be tuned by varying the magnetic field strength.

Synchrotron radiation is produced by bunches of electrons circulating in a storage ring; electron energies range from hundreds of MeV up to the GeV range. The rings have diameters of tens or hundreds of meters, so the bunch orbit time is typically on the order of 100 - 1000 ns. Each bunch is localized to a few cm in size. The temporal structure of a synchrotron radiation is therefore a series of pulses of a few ns width, with pulse frequency of order 1 - 10 MHz. The radiation continues during the decay time of the storage ring, generally many hours.

For applications requiring short wavelengths (vacuum ultraviolet to x-rays), synchrotron radiation possesses the same advantages that lasers have over other visible and near-visible sources. Standard methods of active spectroscopy (absorption, fluorescence, photoelectron, etc.) are used for crystallography, surface science, and inner-shell electron study [74-77]. Two major technological applications are submicron lithography for semiconductor processing and x-ray angiography of coronary disease [78,79]. Despite the short coherence length, synchrotron radiation has been used in x-ray holography [80].

2.5.1.1 General Properties of Synchrotron Radiation

The basic equation of electromagnetic emission from a magnetically deflected electron, in cgs units [73], is

$$P = \frac{2e^2 c \gamma^4}{3\rho^2} \tag{2-88}$$

where P is the power emitted by an electron moving in a circle of radius ρ, e is the electron charge, c is the speed of light and γ is the relativistic energy ratio E/m_0c^2. The total average power emitted may be expressed as

$$P_{tot}\,[kW] = 0.0265E^3[GeV]B[T]i[ma] \tag{2-89}$$

where B is the magnetic field strength and i is the time-averaged beam current. For electron energy 2 GeV, 1-T fields, and current of 100 mA, the total emitted power is 21 kW. The radiation has a broadband spectral distribution, proportional to the function

$$G_1(y) = y \int_y^\infty K_{5/3}(t)dt \tag{2-90}$$

$K_{5/3}$ is a modified Bessel function of the second kind,

$$y = v / v_c ; \quad v_c = \frac{3c\gamma^3}{4\pi\rho} \tag{2-91}$$

ν is the photon frequency, and ν_c is the critical frequency. For example, typical numbers for a hard x-ray source give a critical photon energy of $h\nu_c = 5$ keV or $\lambda c = 2.5$ Å.

The function $G_1(y)$ is plotted in Figure 2-31. The spectral peak is at somewhat lower energy than the critical photon energy, falling off sharply on the high-energy side but quite slowly on the low-energy side. For this reason, a synchrotron operating in the soft x-ray region still emits quite a lot of light in the visible and near-UV.

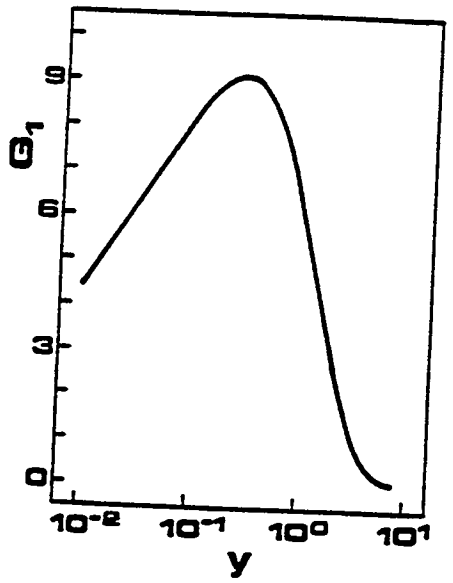

Figure 2-31
The Function $G_i(y)$ Gives the Spectral Profile of Bending Magnet and Wiggler Radiation, According to Ref. [73]

A wiggler or undulator consists of a region of sinusoidal magnetic field $\sin 2\pi\, s/L_w$, where s is the coordinate along the beam and L_w is the wiggler period. This causes the electron beam to follow an oscillating trajectory. Interference among wiggler periods causes destruction of most of the spectrum except for odd harmonics of the wavelength corresponding to the relativistically shortened wiggler period $L_w/2\gamma^2$. This spectral narrowing may or may not be smeared out by the angular divergence of the beam, according to the value of the dimensionless parameter

$$K = eBL_w/2\pi m_o c = 0.934B[T]L_w[cm] \qquad (2\text{-}92)$$

If $K < 1$ (weak magnetic field), the beam angular divergence caused by the wiggling is smaller than that of the emission itself, while if $K > 1$ (strong field), the reverse is true. A multiperiod sinusoidal magnetic field is called a wiggler if $K > 1$; wiggler radiation has the broadband bending magnet spectrum. If $K < 1$, the device is called an undulator and the spectrum consists of odd harmonics of the undulator wavelength $L_w/2\gamma^2$.

2.5.1.2 Optical Hardware for Use in Synchrotron Radiation

The applications of synchrotron radiation described above generally employ wavelengths sufficiently short that satisfactory materials are not available to fabricate usual transmissive optical elements (lenses and fibers). For this reason, beamlines typically admit synchrotron radiation directly into an experiment without focusing; if focusing is needed, curved mirrors are used. If spectral filtering is needed, ruled gratings may be used in the UV region, while x-ray monochromators may be made using Bragg reflections from a crystal surface, which thus acts as a grating. Apertures, of course, may be used.

2.5.1.3 Radiometric Properties of Synchrotron Radiation

This section is concerned with the possibility of finding a function giving the brightness [1,2] which, for a cross-spectral density function appropriate for synchrotron radiation, transforms in the normal radiometric manner. This is an important issue in the design of beamlines of synchrotron facilities.

The issue has been treated in two works by Kim [24,81]. He considered the case of paraxial propagation and showed that in this case, the brightness defined by Walther's first definition of the generalized radiance function (grf) [1] does in fact transform radiometrically. We retrace Kim's reasoning below, filling in the steps.

The following is based on Ref. [24]. We start with Kim's Eq. (14), defining brightness as in [1]

$$B(x,\phi) = \text{const.} \int d^2\xi \left\{ \varepsilon^* \left(\phi + \frac{\xi}{2} \right) \varepsilon \left(\phi - \frac{\xi}{2} \right) \right\}_{ens} e^{-ikx\xi}$$

$$= \frac{\text{const.}}{\lambda^2} \int d^2 u \left\{ E^* \left(x + \frac{u}{2} \right) E \left(x - \frac{u}{2} \right) \right\}_{ens} e^{ik\delta u} \qquad (2\text{-}93)$$

where x is the coordinate transverse to the optical axis and ϕ is the angle from the axis, E, ε are the electric field and its Fourier transform, and $\{...\}_{ens}$ denotes the ensemble average. (Because of the strong linear polarization, the electric field is treated as a scalar.) We first consider the propagation through free-space using the Fresnel kernel:

$$\varepsilon(\phi;z+1) = \varepsilon(\phi;z)e^{ikl\left(1-\phi^2/2\right)} \tag{2-94}$$

where use has been made of the paraxial approximation $\phi^2 << 1$. Substituting this into Eq. (2-93), we obtain

$$\begin{aligned} B(x,\phi;z+1) &= \text{const.} \int d^2\xi \left\{\varepsilon^*\left(\phi+\frac{\xi}{2};z\right)e^{-ikl\left(1-(\phi+\xi/2)^2/2\right)}\varepsilon\left(\phi-\frac{\xi}{2};z\right)e^{ikl\left(1-(\phi-\xi/2)^2/2\right)}\right\}_{ens} e^{ikx\xi} \\ &= \text{const.} \int d^2\xi \left\{\varepsilon^*\left(\phi+\frac{\xi}{2};z\right)\varepsilon\left(\phi-\frac{\xi}{2};z\right)e^{ikl(\phi\varepsilon)}\right\}_{ens} e^{ikx\xi} \\ &= \text{const.} \int d^2\xi \left\{\varepsilon^*\left(\phi+\frac{\xi}{2};z\right)\varepsilon\left(\phi-\frac{\xi}{2};z\right)\right\}_{ens} e^{ik(x-l\phi)\xi} \\ &= B(x-l\phi,\phi;z) \end{aligned} \tag{2-95}$$

which is the desired radiometric transform. In similar fashion, the thin-lens transformation $B_{after}(x, \phi) = B_{before}(x, \phi + x/f)$ is obtained, where f is the focal length of the lens. This result should be compared with the result which is based on Walther's second definition of generalized radiance [2]. However, a direct comparison of the R^2T method with the Fresnel diffraction model, presented in Section 2.1.6.2 demonstrates that the approach based on Walther's second definition is correct.

For non-paraxial propagation, it is not in general clear that Walther's first grf rigorously obeys radiometric transformations. It is worthwhile to ask whether synchrotron radiation may be considered as a quasi-homogeneous source in the sense of Carter and Wolf [7]. The condition for this is that the cross-spectral density $W(r_1, r_2)$ be given by

$$W(r_1, r_2) = [I(r_1, r_2)]^{1/2}\,\mu(r_1, r_2) \tag{2-96}$$

where I is approximately constant over a distance corresponding to the range of nonzero μ, so that the square root may be replaced by $I(\vec{r}_1 + \vec{r}_2/2)$. It also follows from this that the source must be large compared to the wavelength.

For bending magnet and wiggler radiation, the source may or may not be considered quasi-homogeneous. To begin with, the source size (~1 mm) is considerably larger than the wavelength (200 nm or shorter). The cross-spectral density function is zero for values of $|r_1 - r_2|$ much larger than the transverse coherence length. As seen above, this coherence length is given by the single-electron source size $\sigma_r = \lambda/(4\pi\sigma_{r'})$, where $\sigma_{r'}$ is the angular divergence of the electron radiation, given approximately by [73]

$$\sigma_{r'}[\text{mrad}] = \frac{565}{\gamma}(\nu/\nu_c)^{-0.425} \qquad (2\text{-}97)$$

At electron energy 1 GeV, $\gamma \equiv 2000$ and at the critical wavelength, the angular divergence is about 0.25 mrad. If the critical wavelength is 100 Å, the transverse coherence length at λ_c is 3 μm, or roughly 1/100 of the source size. On the other hand, at 10,000 Å with other parameters the same, the transverse coherence length is about 50 μm, or about 1/10 of the source size. Thus the source at 100 Å satisfies the requirements for quasi-homogeneity, whereas at 10,000 Å, it does not.

In the above, the single-electron radiance was used to determine the coherence. This is appropriate because the electrons at the source are statistically independent: in synchrotron radiation, the emission is spontaneous, while the position of each electron in the storage ring is almost completely uncorrelated with those of other electrons. (This expresses the insignificance of the electron-electron interaction in comparison with the electron beam energy.)

Undulator radiation is less often quasi-homogeneous. This is explained using the analysis of Ref. [24], giving

$$\sigma_{r'} = \sqrt{\lambda/L}\,; \quad \sigma_r = (1/4\pi)\sqrt{\lambda L} \qquad (2\text{-}98)$$

where L is the undulator length (typically less than ten meters for 'ordinary' undulators, and several tens of meters for high-gain undulators [see below]). For L =10 m and λ = 100 Å, σ_r = 10 μm, and for λ = 10,000 μm, σ_r = 100 μm.

In all the above analysis, it was assumed that radiation was spontaneous. As the number of undulator periods increases, the fraction of stimulated emission increases exponentially until it dominates. In that case, the positions of radiating electrons are no longer independent and the

radiation becomes highly transversely coherent. The opposite extreme of the partial coherence theory may then be used [12,27].

2.5.1.4 Applications of Radiometric Ray Tracing at Lawrence Berkeley Laboratory

Professor Kwang-Je Kim of the Center for X-Ray Optics, Lawrence Berkeley Laboratory, University of California, Berkeley, California, has investigated the radiance function propagation through free-space for synchrotron radiation [24] , using Walther's first definition of radiance [1], based on Wigner distribution. Based on Bastiaan's earlier results [40], he has demonstrated that Wigner's distribution is invariant for free-space paraxial optics [24]. These results are discussed in Section 2.1.6. He also analyzed the global spatial coherence of synchrotron radiation.

2.5.1.5 Phase-Space Treatment of Linear Electron Accelerator LINAC Radiation at the Central Institute of Physics in Bucharest, Rumania

Using the phase-space throughput approach [43], Dr. George Nemez of the Central Institute of Physics at Bucharest, Rumania (presently visiting Professor at Ginzton Laboratory, Stanford University) has designed optimum radiation throughput for radiation from charged particle beams for the first Romanian linear electron accelerator LINAC 101 [43]. Some of the results adapted by him for this program were discussed in Sections 2.2.3 and 2.2.4.

2.5.2 Schell-Model Beams

In the case of Schell-model beams, the cross-spectral density has the form:

$$W(\vec{r}_1,\vec{r}_2)=\sqrt{I(\vec{r}_a)}\sqrt{I(\vec{r}_2)}\,\mu(\vec{r}_1-\vec{r}_2) \qquad (2\text{-}99)$$

i.e., the model of quasi-homogeneous sources (see Section 2.1.2) is more restricted than the Schell beam model (Ref. [27] and Appendix C). It should be noted that both models cover almost all the sources of interest. Specifically, the quasi-homogeneous sources cover all classical Lambertian heat sources, partially coherent non-Lambertian sources (such as tungsten lamps, deuterium lamps, hollow cathodes, laser induced plasma), multi-mode laser sources (Nd:YAG, laser diodes, etc.)

and synchrotron radiation. On the other hand, the Schell model beams cover fully-coherent single-mode laser sources, described as Gaussian distributions.

Simon and Wolf [27] have investigated Gaussian-Schell model beams. Specifically, in Appendix C, they study the propagation of a Gaussian-Schell model beam through a lossless lens system in the form of Eq. (2-100) and Eq. (2-101). (Compare this with Eq. (2-61).)

$$I(\vec{r}) = I_0 \exp\left(-r^2/2\sigma s^2\right) \tag{2-100}$$

$$\mu(\vec{r}_1,\vec{r}_2) = \exp\left[\frac{-(\vec{r}_2-\vec{r}_1)^2}{2\sigma_\mu^2}\right]\exp\left\{\left[(-ik/2R)\left(r_2^2-r_1^2\right)\right]\right\} \tag{2-101}$$

where I_0 is the spectral density at the axial point $\vec{r} = 0$ and σ_s, σ_μ R are the effective beam width, the transverse coherence length and the radius of curvature, respectively. R is positive or negative as the beam diverges or converges.

Using Walther's first definition of radiance (Ref. [1]; see, also Section 2.1.6), it was shown [24] that in the paraxial optics approximation, the radiance function satisfies the simple transport law [27]:

$$B(\vec{r},\vec{p}) = B_0\left(D\vec{r}-B\vec{p},-C\vec{r}+A\vec{p}\right) \tag{2-102}$$

equivalent to the physical analog of the brightness theorem that states that the phase-space density, or generalized radiance function transfer according to the ABCD matrix law (see Section 2.1).

As an example, the simple lens geometry, illustrated in Figure 2-32, has been analyzed. As a result of this analysis, the angular distribution of the generalized radiance function changes as are illustrated in Figure 2-33.

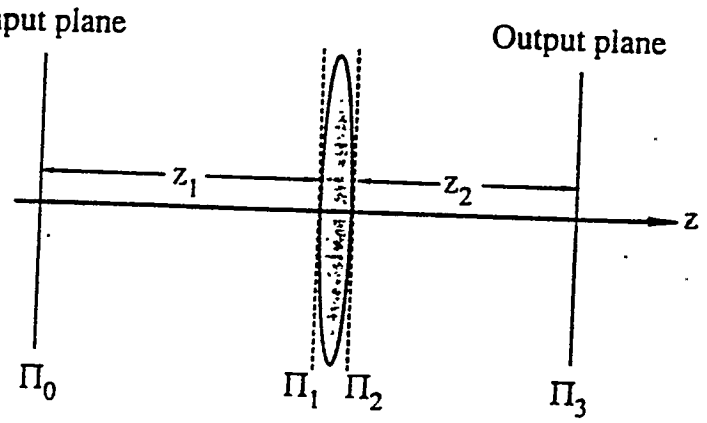

Figure 2-32
Illustration of the Notation for Beam Propagation Through a Thin Lens

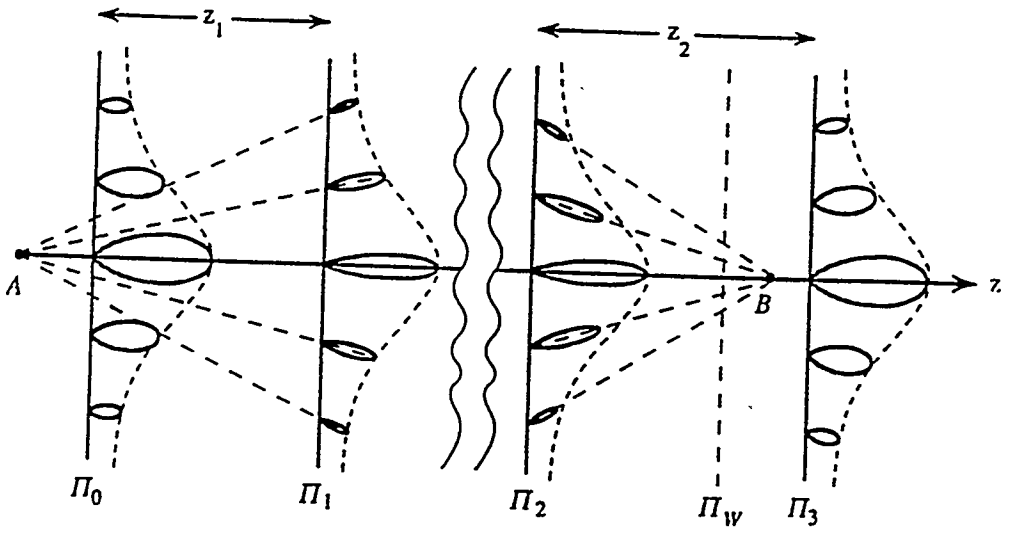

Figure 2-33
Example Which Illustrates the Changes in the Angular Distribution of the Generalized Radiance of a Gaussian-Schell Model Beam on Propagation Through a Thin Lens. Π_o, Π_1, Π_2, and Π_3 have the same meaning as in Figure 2-33 with Π_o coinciding with the plane containing the waist of the incident field. The plane Π_W is the plane containing the waist of the beam after it has passed through the thin lens. For a more detailed description, see Appendix B.

2.5.3 Analogue of the Van Cittert Zernike Theorem for Statistically Homogeneous Wave Fields

In this section, we discuss the subject that will put the R^2T formalism into a broader perspective. The basic objective of the R^2T model is to provide simple propagation relations for radiometric

In particular, using Eq. (2-106), we can obtain the propagation of the coherence area through free-space, generated by some stimulated emission region, using the conventional Fresnel diffraction integral in the form

$$\mu(r') = \frac{\exp ikz}{i\lambda z} \iint \mu_o(\vec{r}_o') \exp\left\{\frac{ik}{2z}\left[(x'-x_o')^2+(y'-y_o')^2\right]\right\} dx_o' dy_o' \qquad (2\text{-}107)$$

where μ_o and μ are the input and output spatial distributions of complex degree of coherence.

The other interesting example is the statistically homogeneous wave field with limited spatial power spectrum:

$$p_x^2 + p_y^2 = p^2 \leq \sin^2\alpha \qquad (2\text{-}108)$$

In such a case, the behavior of the modules $\left|\mu(\vec{R}')\right|$ is illustrated in Figure 2-34.

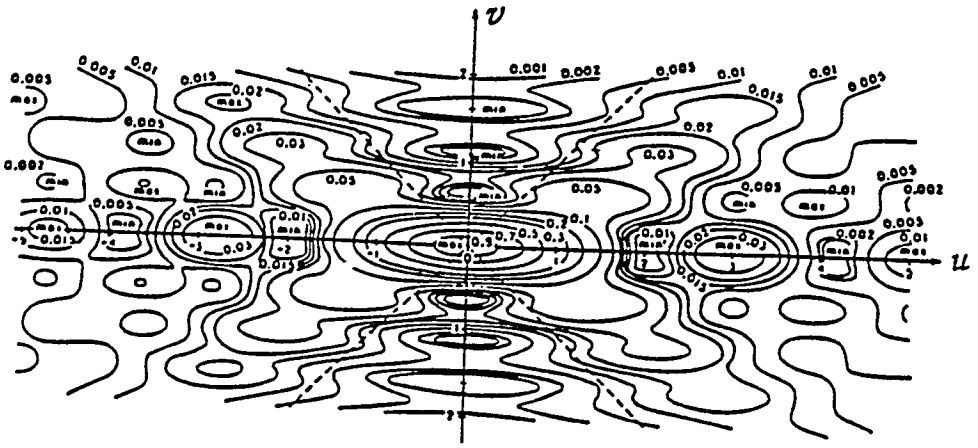

Figure 2-34

Behavior of the Modulus $\left|\mu(\vec{R}')\right|$ of the Degree of Spatial Coherence of the Statistically Homogeneous Wave Field Whose Spatial Power Spectrum is Given by Eq. (2-108) with $\alpha << \pi/2$. The axes represent the quantities $u = kz' \sin^2\alpha$ and $v = k\rho' \sin\alpha$, where z' and ρ' are the components of the vector $\vec{R}' = \vec{R}_2 - \vec{R}_1$ along the z direction and perpendicular to it. The dashed lines represent generators, making angles α (shown exaggerated here) with the z axis, of the cone of directions forming the solid angle Ω_o. The numbers on the contours are the values of $|\mu(\vec{r}', \omega)|^2$. [Adapted from E. H. Linfoot and E. Wolf, Proc. Phys. Soc. London B 69, 823 (1956).

This formalism can be useful in laser physics and in plasma physics where the understanding of propagation of spatial coherence is of fundamental importance.

2.5.4 Holographic Optical Systems

Recently, a number of optical system solutions, including holographic optical elements (HOEs), have been applied in DOE-related programs, including x-ray optics and plasma physics. The HOEs can be treated as a generalization of diffraction gratings. That is, they integrate grating dispersion and optical imaging properties. From a radiometric ray tracing perspective, their behavior is fully defined by two equations: the first is a local grating equation:

$$k(\vec{p}-\vec{p}_o) = m\vec{K}_{||} \qquad (2\text{-}109)$$

where $k = 2\pi/\lambda$, $\vec{p}$ and $\vec{p}_o$ are horizontal components of diffraction and incident propagation unit vectors, $\vec{K}_{||}$ is the horizontal component (i.e., parallel to the grating surface) of the grating vector, and $m = 0, \pm1, \pm2$, determines diffraction orders.

In the Bragg diffraction case, only one diffraction order ($m = +1/-1$) is accepted, and the second equation is

$$k(s_z - s_{zo}) = \vec{K}_{\perp} \qquad (2\text{-}110)$$

where $\vec{s} = (\vec{p}, s_z)$, and $\vec{K}_{\perp}$ is the vertical component of the grating vector $\vec{K}$. Both equations can be treated locally in the vicinity of a given point of the HOE. While Eq. (2-109) fully defines geometrical ray tracing, Eq. (2-110) defines the angular/wavelength characteristics of hologram diffraction efficiency.

Since the behavior of Eq. (2-109) is well known, in this program we concentrated on the analysis of Eq. (2-110). In particular, for Lippmann holographic gratings, $\vec{K}_{||} = 0$ and $\vec{K} = \vec{K}_{\perp}$; thus,

$$|\vec{K}| = \frac{2\pi}{\Lambda} \qquad (2\text{-}111a)$$

and

$$\Lambda = \Lambda(z) \tag{2-111b}$$

is a slowly varying grating constant for the generally nonuniform Lippmann mirror illustrated in Figure 2-35.

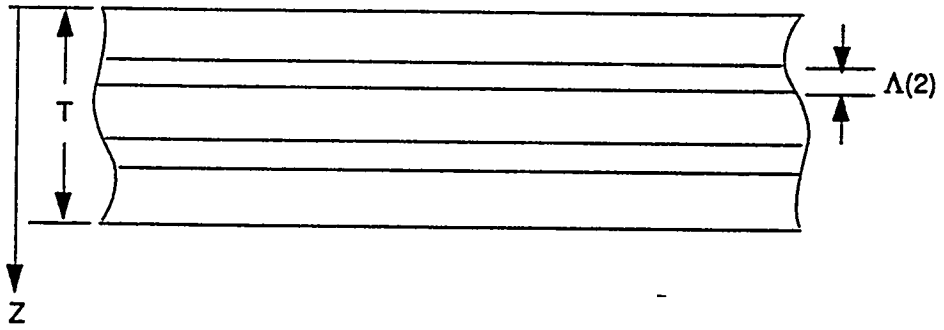

Figure 2-35
Illustration of Nonuniform Lippmann Holographic Mirror with Thickness, T, and Slowly-Varying Distribution of Grating Constant, Λ(z).

2.5.5 Radiation Transfer and Heat Transfer

The case described by Eq. (2-110) was analyzed for the first time in Ref. [29] for the application of HOEs to this program, providing a complete tool for analyzing optical systems, including HOEs, by radiometric tracing.

In the conventional radiometry, the radiative energy transfer is based on the differential equation of the propagation of radiance, encompassing absorption, emission and scattering [86,87,90]:

$$\vec{s}\vec{\nabla}_\nu B_\nu(\vec{r},\vec{s}) = -\alpha_\nu(\vec{r},\vec{s})B_\nu(\vec{r},\vec{s}) + \int B_\nu(\vec{r},\vec{s},\vec{s}')B_\nu(\vec{r},\vec{s})d\Omega' + D_\nu(\vec{r},\vec{s}) \tag{2-112}$$

where B_ν is the radiance function, α_ν is the emissivity, $\vec{r}$ is the position vector, $\vec{s}$ is the unit direction vector, $d\Omega$ is the solid angle element, ν determines frequency. Since the first two terms define the Liouville theorem (see Appendix A), we can adopt the R^2T method for radiative energy

transfer problems. The analogous approach can also be used for structural information transfer [88,89].

3.0 AUXILIARY RESULTS

3.1 Volume Holographic Diffusers

Physical Optics Corporation (POC) has developed a new method of light-beam shaping that utilizes volume holography to scatter collimated light into a controlled pattern with smooth brightness variation. This method of controlled diffusion can achieve structureless illumination patterns much more easily than conventional lenses and mirrors, and at lower manufacturing costs. Aside from small-area illumination by spotlights and searchlights, most illumination tasks involve spreading of light into a moderate angle, such as 20 to 80 degrees. POC's holographic diffusers can diffusely scatter light into such a pattern, while conventional diffusers, such as ordinary frosted glass, totally scatter light into a hemispherical pattern. Holographic diffusers are useful whenever it is desired that the light source appear to be of uniform brightness, with no "hot spots" to discomfort the eye. While this kind of glare-free appearance is as desirable in lights of moderate spread as it is for floodlighting, conventional reflector or lens designs usually appear to have highly non-uniform brightness. POC has developed and demonstrated holographic diffusers with both controlled directionality of transmittance and low visual glare. Using proprietary holographic materials and exposure methods, POC can make a wide variety of diffusers that produce smooth but confined illumination patterns and give the source a glare-free appearance. For example, a holographic diffuser on a round flashlight can produce an elliptical illumination pattern, which normally requires an elliptical reflector. Moreover, any flashlight would benefit from the smooth illumination pattern which holographic diffusers produce, unlike the distracting structured patterns of conventional flashlights.

3.1.1 Controlled Scattering of Light

The scattering of light consists of a loss of the directionality of a beam as its rays are randomly turned into a wider set of directions. It is distinct from the redirection done at the surface of a mirror or lens by reflection or refraction, which do not increase the entropy, or disorder, of a light beam. In nature there can be many degrees of scattering, such as we see with sunlight as it varies from the dazzle of a clear day, with only some blue-light scattering that colors the sky, to an

overcast day with a uniformly gray sky. Intermediate degrees admit of a fuzzy glare in the general direction of the sun. This is volume scattering, the cumulative effect of passage through an extended gradually scattering medium, in this case the earth's atmosphere. Some of the atmosphere's volume scattering processes send light into all directions uniformly, while some have concentrations in the forward or backward directions, depending upon the nature of the scattering centers, whether molecular or particulate. In nature, scattering along any angle from the original direction of the light is uniform around a conical pattern centered on that original direction: there are no azimuthal variations in the scattering (see Figure 3-1). We shall see that holographic diffusers are not subject to this limitation.

Artificial diffusers have become common in this century of electric illumination, with frosted and textured glass as examples. Like their natural counterparts, however, these surface scatterers exhibit highly diffuse scattering. While not all light may be scattered, as in a slight frosting of the surface of a piece of glass, that part of the light which is scattered goes into a wide, almost hemispheric, range of angles away from the original direction of light. Such hemispheric scattering is termed "Lambertian" in the parlance of photometry, after one of its founders. These diffusers commonly rely on surface roughness, a microscale irregularity that consists of multiple random refractors that spread light out, away from its original incoming direction. The statistical characteristics of the irregularity are difficult to control, so that a designer has little ability to specify a particular scattering pattern. If he could do so, such scattering specificity would be a third method of directional control, in addition to reflection and refraction.

POC discovered and empirically confirmed a new method of producing controlled scattering with holographic diffusers, which consist of a thin (< 1 mm) volume of spatially fluctuating refractive index. Using coherent light in a proprietary exposure configuration, the statistics of the fluctuations in the volume hologram can be tailored so that the resulting scattering pattern can take a variety of shapes. In the diffusers produced so far, there are two constraints upon the controlled scattering:

(1) Light is scattered relative to its incoming direction, NOT relative to the surface of the diffuser. This means that for maximum pattern control a diffuser should use collimated light (i.e., all of the same direction, as from a searchlight). Deviations from this ideal input would blur the output pattern accordingly. Non-collimated light will have a spread that is the superposition (technically, the convolution) of the input light and the controlled scattering.

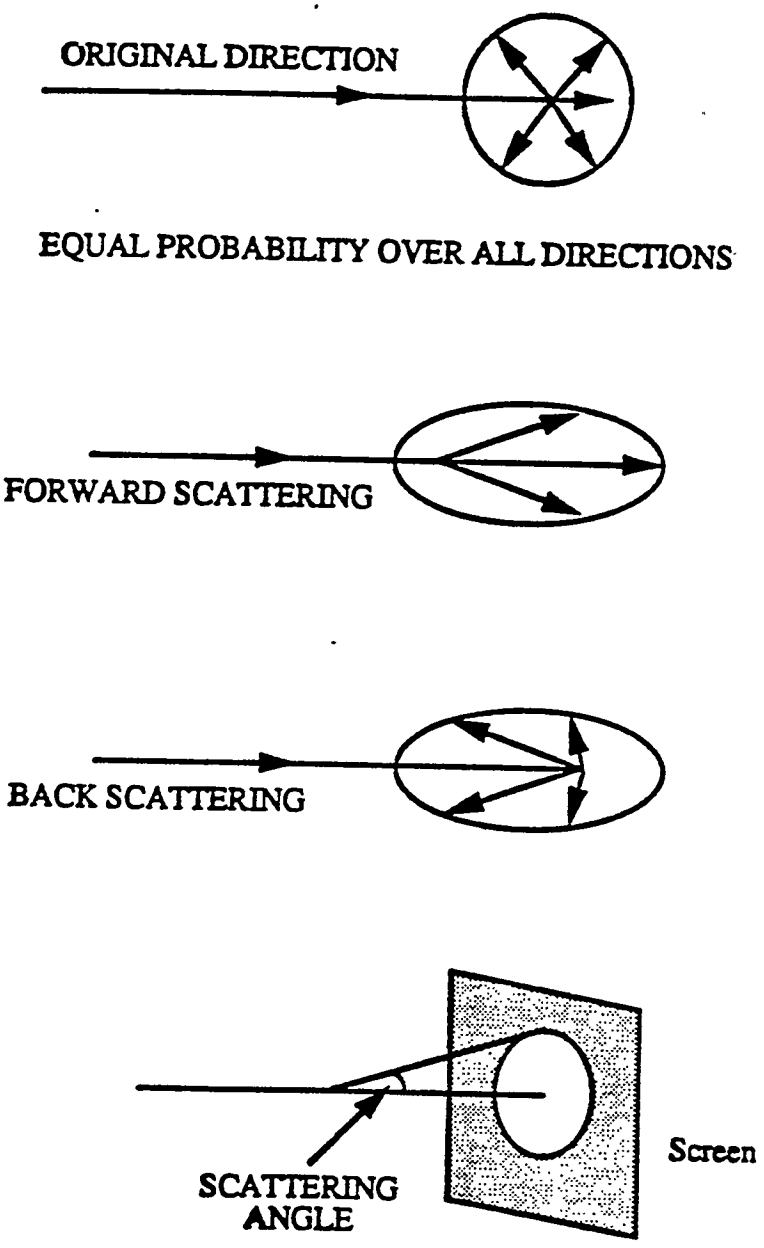

Figure 3-1
Natural Scattering of Light. At all scattering angles, there is circular symmetry.

(2) The scattering pattern is not arbitrarily specifiable, but has the form of an autocorrelation function, as will be explained below. This means that the maximum brightness of the scattering pattern is in the same direction as that of the input light ray, and that the brightness of the scattered light will fall off smoothly to zero with

increased scattering angle away from the original direction of the incoming light, with no discontinuities in the illumination pattern. Unlike conventional diffuse scattering, the pattern need not be rotationally symmetric, so that elliptical patterns are easily generated from round apertures.

The overall illumination pattern from a light with a holographic diffuser will be the resultant of the diffuser's scattering pattern and the total number of direction's encompassed by the light striking the diffuser.

There are a wide variety of lighting tasks for which such controlled diffusion will be useful, and for which lens and mirror designs would be somewhat bulky. Collimated light would be changed by a uniform diffuser into a particular scattering pattern, and the diffuser would appear uniformly bright to someone within its illumination pattern.

3.1.2 Autocorrelation Illumination Patterns

The correlation function was originally discovered by statisticians as a part of their search to express regularities and correspondences in sequences of data. Scientific investigations often express the probability of an occurrence of causality in terms of the correlation function between two sequences of data, f and g, as the sum of the term-by-term products of the members of each n-term sequence:

$$C_{fg}(k) = \sum_{i=0}^{n} f(i)\, g(i+k) \qquad (3\text{-}1)$$

where k is a shift used to find the position of best congruence, as might happen in a case of delayed causality. Autocorrelation is simply a function's correlation with itself, as a function of shift. It is customary to normalize it by dividing by the square of the function:

$$C_f(k) = \sum_{i=0}^{n} f(i)\, f(i+k) \,/\, \sum_{i=0}^{n} f^2(i) \qquad (3\text{-}2)$$

Hereafter this normalization will be understood to be present, although it will not appear in the equations. For continuous functions, the summation becomes an integral, but the autocorrelation function itself has the same character:

$$C_f(u) = \int f(x)\, f(x+u)\, dx \qquad (3\text{-}3)$$

For functions which are finite in extent, this is an overlap integral or functional of a shift u, with a maximum value at u = 0 (no shift) and zero for u bigger than the width of the function. If the input function is real, the autocorrelation is symmetrical.

To illustrate how the autocorrelation function works, Figure 3-2 shows how a rectangular function gives rise to a triangular autocorrelation function that is twice as wide. Other input functions are plotted in Figure 3-3, for -1 < x < 1, from the highest to the lowest. In Figure 3-4, the autocorrelations of these functions are shown in the same order. In spite of the very different input shapes, the autocorrelations are similar.

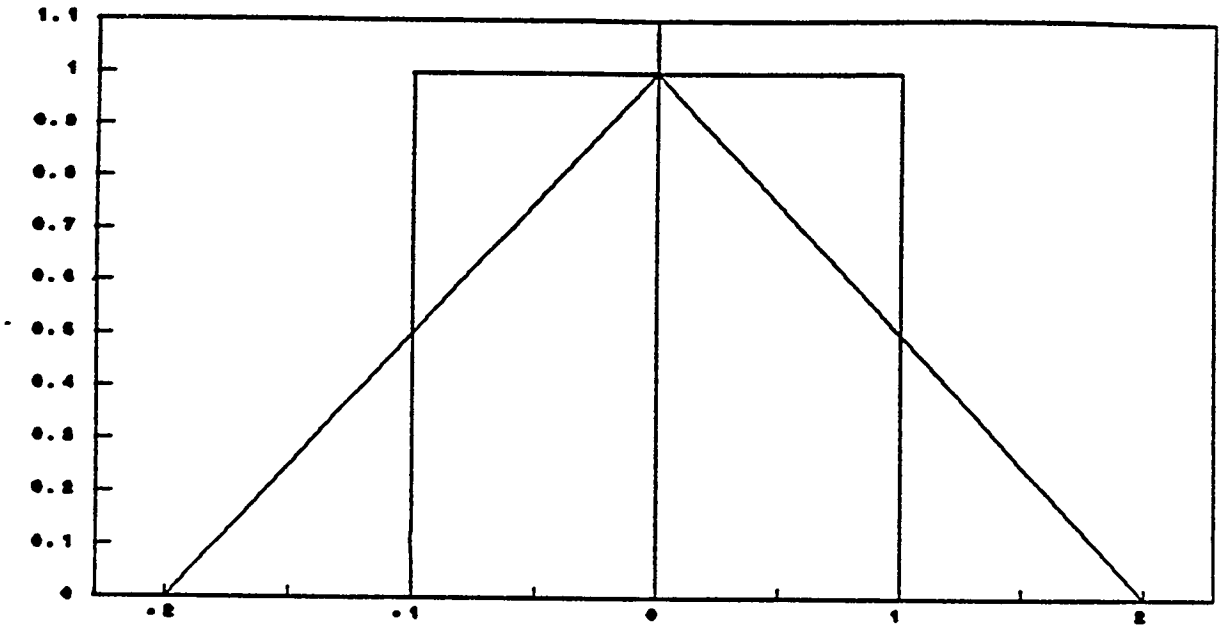

Figure 3-2
Rectangular Function Has Triangular Autocorrelation

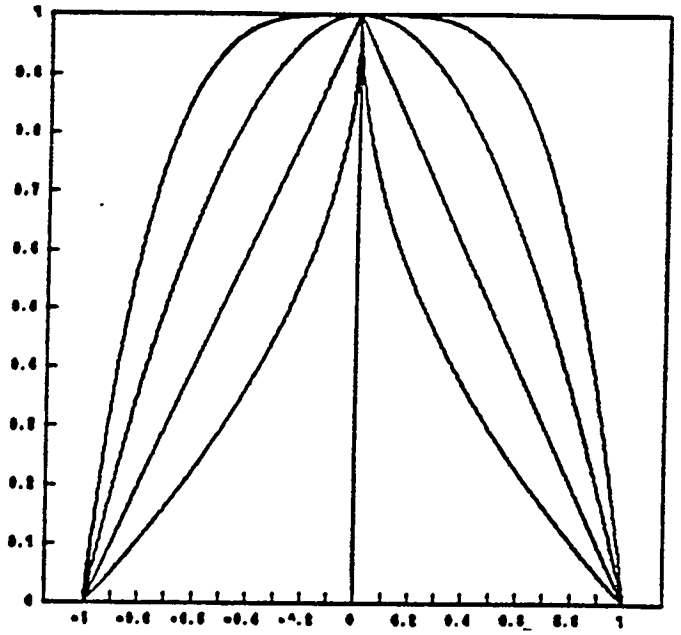

Figure 3-3
Different Input Functions

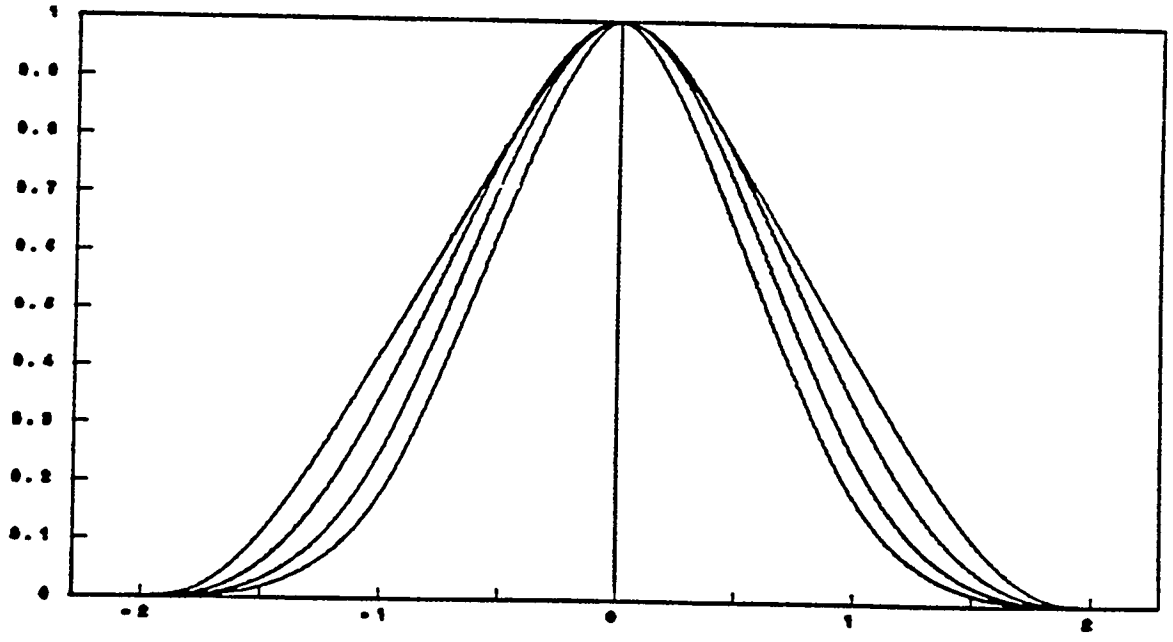

Figure 3-4
Autocorrelation Functions for the Input Functions of Figure 3-3

Actually, holographic diffusers will exhibit a scattering pattern that is a two-dimensional autocorrelation:

$$C_f(u, v) = \iint f(x + u, y + v)\, f(x, y)\, dx\, dy \qquad (3\text{-}4)$$

where f(x,y) is a grey-scale transmittance pattern that is the input to POC's proprietary holographic exposure process. So far, we have produced diffusers using real (i.e., transmittance only) input values, so that the diffusers' output patterns are centro-symmetric. Figure 3-5 shows the elliptical output pattern of our sample diffusers.

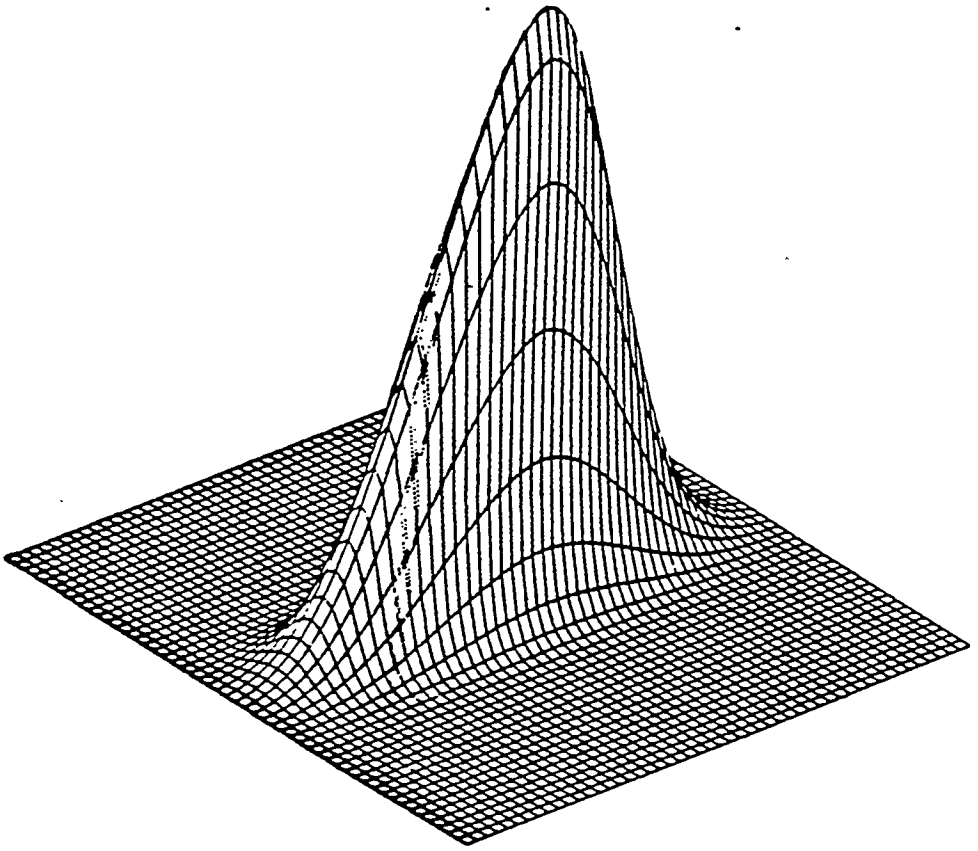

Figure 3-5
Elliptical Scattering Pattern

In general, a lighting device utilizing a holographic diffuser will have an illumination pattern that depends upon the distribution of light striking the diffuser, as well as the scattering pattern of the diffuser itself. The light leaving any point on the diffuser is its scattering pattern smeared by the

distribution of incoming light. The combination of these two distributions gives considerable latitude to an illumination engineer. As long as the diffuser's scattering pattern is wider than the apparent diameter of the source as seen by someone in its illumination pattern, its appearance will be that of uniform brightness, with no bright spots.

3.2 Quasi-Homogeneous Sources with Controlled Spatial Coherence

It is important to realize that the moving diffuser can simulate a quasi-homogeneous source with regulated spatial coherence degrees. This assumes that the diffuser speed is sufficiently high to enable the process to be ergodic. In order to show this, it is necessary to prove the auxiliary theorem that the spatial coherence radius, ρ_{coh}, is proportional to the speckle r.m.s.

$$\rho_{coh} \sim \text{r.m.s.} \tag{3-5}$$

According to the 2-D van Cittert-Zernike theorem, it is possible to regulate the output speckle r.m.s., by the input intensity distribution (or, input aperture). Therefore, it is indeed possible to design the laser source, with high temporal coherence, and low spatial coherence regulated through Eq. (3-5).

3.3 Summary of Non-Imaging Optic (NIO) Software Capabilities

During this program realization, POC has expanded the capability of ray tracing software for NIO's to include the following main features:

1. It is a full menu driven program. For a given three dimensional surface profile, the user need not redefine the mathematical equation to compute the output phase space coordinates whether the ray enters from Z_{min} or Z_{max} (see Figure 3-6).

   If an NIO coupler mode is chosen, the software will generate the mirror image of the other half position of an NIO surface profile automatically to compute the output phase space coordinates of the coupling effect. The flat entry and exit apertures can be of any shape.

2. The program can handle up to 2.1 billion rows of input data points which are more than enough for statistical analysis. It is easily expanded to 4.2 billion rows if necessary.

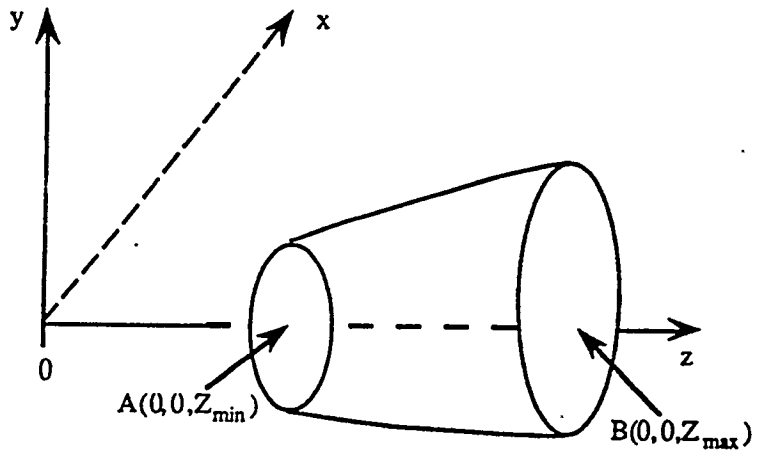

Figure 3-6
Representation of 3D NIO Surface Profile

3. There are four sources of uniform random deviates which allow the user to compare the results if monte carlo analysis is used.

4. The user has a choice of outputting all the ray tracing's history of all input rays into a data file which is useful information for optimization.

5. To add a new NIO surface profile, the user needs only to add a simple subroutine to the program.

6. The software is also designed to read a special input ray distribution which is stored in an ASCII data file. The size of the file is only limited to the size of the storage media.

3.3.1 Non Imaging Optic (NIO) Surface Profile

Winston has generated a 2D Compound Parabolic Concentrator (CPC) (see Figure 3-7) which is based on the "edge-ray principle". The equation is given by

$$\left(\sqrt{r^2}\cos\theta_{max} + Z\sin\theta_{max}\right)^2 + 2a_1(1+\sin\theta_{max})2\sqrt{r^2} - 2a_1\cos\theta_{max}(2+\sin\theta_{max})Z$$

$$- a_1^2(1+\sin\theta_{max})(3+\sin\theta_{max}) = 0 \qquad (3\text{-}6)$$

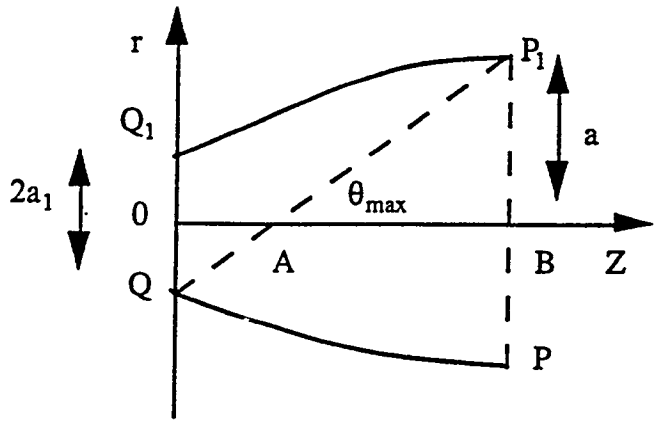

Figure 3-7
2-D CPC Based on the "Edge-Ray Principle"

where θ_{max} is the acceptance angle, 2a is the width of the small (exit) aperture, and $2a = {}^{2a_1}/_{\sin \theta_{max}}$ is the width of the large (entrance) aperture. The length of the CPC is given by

$$OB = \frac{a + a'}{\tan \theta_{max}} \tag{3-7}$$

The point Q is the focal point of a parabola whose axis makes an angle $-\theta_{max}$ with OZ axis. A 3D axial symmetric CPC can be generated by replacing r^2 with $r^2 = x^2 + y^2$. For an elliptic cross section, we use $r^2 = b_y^2\, x^2 + b_x^2\, y^2$. In general, a 3D axial symmetric CPC is not as efficient as in 2D case at θ_{max}. The 3D computation is based on dividing the entry aperture into a grid with spacing equal to ${}^{1}/_{N_{x\ grid}}$ and ${}^{1}/_{N_{y\ grid}}$ of the width of the aperture on x and y axis, respectively. For a circular aperture, we set $N_{x\ grid} = N_{y\ grid} = 100$. For other apertures, we select ${}^{1}/_{N_{x\ grid}}$ and ${}^{1}/_{N_{y\ grid}}$ such that $N_{x\ grid} \times N_{y\ grid} \approx 10^4$. The rays are traced at a chosen collecting angle θ of each grid point (Figure 3-8 with x-axis normal to the Figure). The various entry cross sections with the same area are shown in Figure 3-9. The proportion of these rays that are transmitted by the 3-D NIO give the power transmission $T(\theta,\theta_{max})$ which is defined by

$$T(\theta, \theta_{max}) = \frac{\text{number of output rays}}{\text{number of input rays at the entry aperture}} \tag{3-8}$$

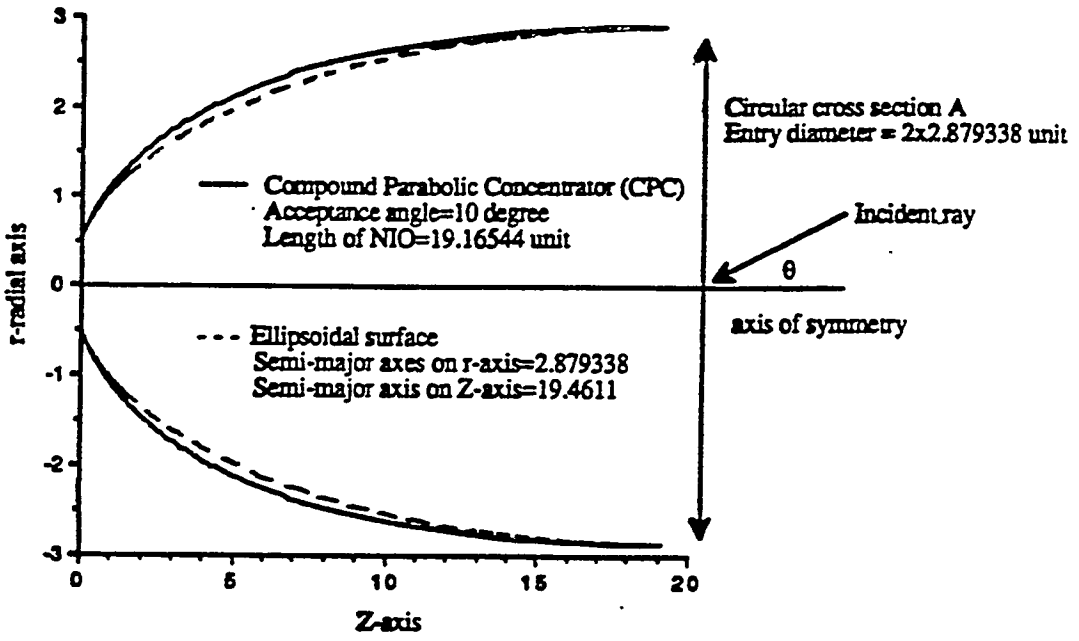

Figure 3-8
Cross Section of Concentrator Profile

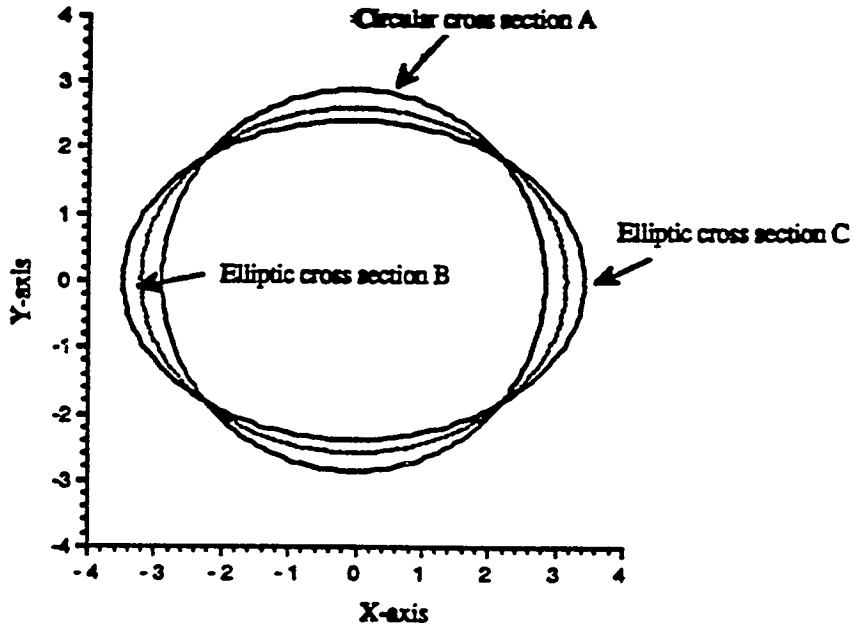

Figure 3-9
Entry Cross Sections at z = 19.16544

Figure 3-10 shows that $T(\theta, \theta_{max})$ can be improved if the entry cross section is modified according to the direction of incident ray. We use elliptic cross section and ellipsoid as an illustration. The equation of an ellipsoid is given by

$$\frac{x^2}{b_x^2} + \frac{y^2}{b_y^2} + \frac{(z-z_c)^2}{b_z^2} = 1 \qquad (3\text{-}9)$$

where b_x, b_y, b_z, and z_c are semi axes and center of the ellipsoid, respectively.

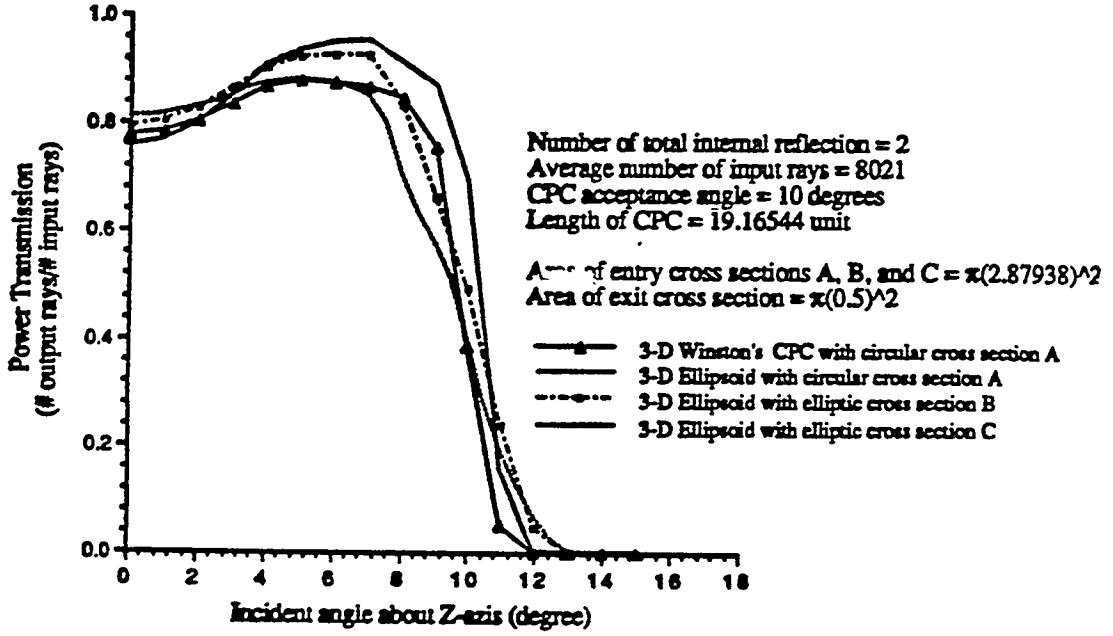

Figure 3-10
Power Transmission for Various Cross Sections

3.3.2 Basic Ray Tracing Algorithm

All vectors are relative to 0, x, y, z frame of reference with 0 as the origin. $\vec{a}_x$, $\vec{a}_y$ and $\vec{a}_z$ are unit vectors along 0x, 0y and 0z, respectively (see Figure 3-11).

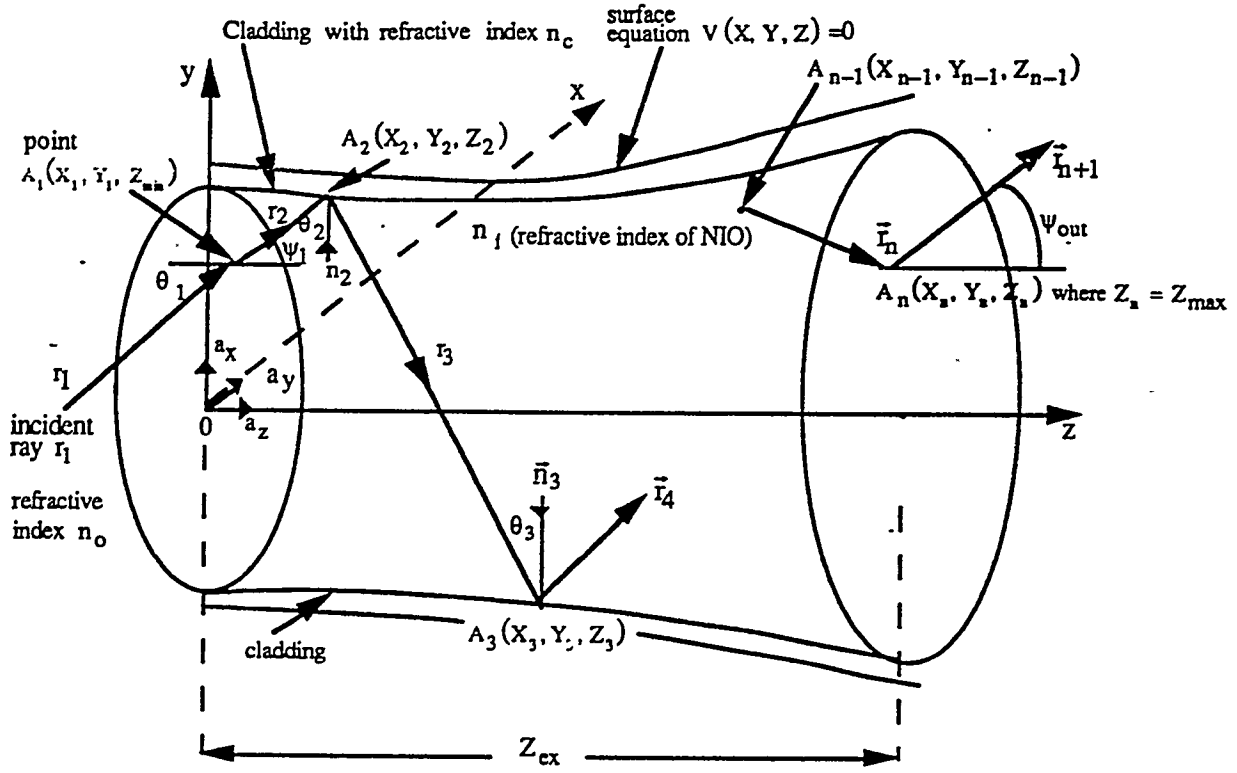

Figure 3-12
Representation of NIO Surface Profile and Notations for Ray Tracing

Definition of notations

$V(X, Y, Z) = 0$, NIO surface equation

n_0 = refractive index outside NIO

n_f = refractive index of NIO

n_c = refractive index of cladding

$\vec{r}_1$ = incident unit vector at $z = z_{min}$

$\vec{r}_{n+1}$ = transmitted unit vector at $z = z_{max}$

$\vec{r}_2, \vec{r}_3, \ldots, \vec{r}_n$ are ray tracing unit vectors inside NIO from A_{p-1} to A_P where $p = 2, 3, \ldots, n$.

$$\vec{r}_2 = \frac{1}{n_f}\left[n_0\,\vec{r}_1 + \left\{n_f(\vec{n}_1 \bullet \vec{r}_2 - n_0(\vec{n}_1 \bullet \vec{r}_1))\right\}\vec{n}_1\right] \qquad (3\text{-}10)$$

$$\vec{r}_p = \vec{r}_{p-1} - 2\left(\vec{n}_{p-1} \bullet \vec{r}_{p-1}\right)\vec{n}_{p-1}, \quad p = 2, 3, \cdots, n-1 \tag{3-11}$$

$$\vec{r}_{n+1} = \frac{1}{n_0}\left[n_f\ \vec{r}_n + \left\{n_0(\vec{n}_n \bullet \vec{r}_{n+1}) - n_f(\vec{n}_n \bullet \vec{r}_n)\right\}\vec{n}_n\right] \tag{3-12}$$

where the unit surface normal $\vec{n}_p$ are given by

$$\vec{n}_1 = \vec{a}_z \text{ at point } A_1 \tag{3-13}$$

$$\vec{n}_n = \vec{a}_z \text{ at point } A_n \tag{3-14}$$

$\vec{n}_p = \dfrac{\nabla V}{|\nabla V|}$ unit outward normal surface vector at A_p, $p = 2, 3, \cdots, n\text{-}1$

Snell law at

$$\text{point } A_1\text{: } n_0 \sin\theta_1 = n_f \sin\psi_1 \tag{3-15}$$

$$\text{point } A_n\text{: } n_f \sin\psi_n = n_0 \sin\psi_{out} \tag{3-16}$$

$$\text{point } A_p\text{: } n_f \sin\theta_p = n_c \text{ for total internal reflection} \tag{3-17}$$

$L_p = A_{p-1}\,A_p$ = distance between A_{p-1} and A_p on an NIO surface, $p = 2,3,\ldots n$. The position vector of A_p relative to origin 0 is given by

$$\vec{OA}_p = \vec{OA}_{p-1} + L_p\ \vec{r}_p\,, \quad p = 2, 3, \cdots, n \tag{3-18}$$

where L_p can be found by solving

$$V\left(\vec{OA}_p\right) = 0 \tag{3-19}$$

with the Newton-Raphson method

3.3.3 Winston's Modified CPC Profile

Our curve depends on six parameters: t_0, τ_0, τ_1, d, c, a_1, $t_0 \geq 0$; $\tau_0 \geq \tau_1 > 0$; $c > 0$; $d > 0$; a_1 is a real number. The additional conditions on the domain of admissible parameters are given by Eqs. (3-23b) and (3-37) shown below. This means that the point P_2 is in the right half plane and that we choose the right branch of the parabola.

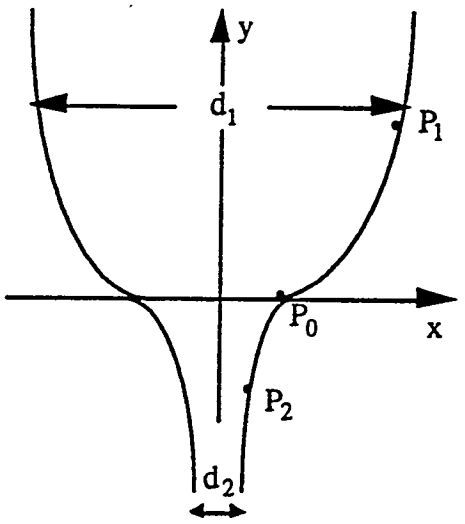

Figure 3-12
From P_0 to P_1: The Piece of Parabola.
From P_0 to P_2: The Piece of Hyperbola.

Remark: It is possible to reduce the number of parameters to five, if the diameter of the upper fiber d_1 is made to be equal to 1. Indeed passing to another scale, if necessary, one can suppose that $d_1 = 1$ (see Eq.(3-36) below), it enables us to consider a_1 as an intermediate coefficient. The following are formulas for intermediate coefficients.

$$\alpha = \frac{d - 2c\, t_0\, \tau_0^2}{2cdt_0 + \tau_0^2} \tag{3-20}$$

$$a = t_0 + \frac{\alpha d}{\tau_0} - \tau_0 \tag{3-21}$$

$$b = c\, t_0^2 + \alpha\tau_0 + \frac{d}{\tau_0} \tag{3-22}$$

$$t_1 = \frac{d - d\tau_1^2}{2c\tau_1^2 + 2c\alpha d} \tag{3-23}$$

$$t_1 \geq t_0 \tag{3-23a}$$

$$a_2 = -ct_0^2 - \frac{t_0}{2ct_1} \tag{3-24}$$

$$\beta = \frac{1}{2ct_1} \tag{3-25}$$

$$u = 1 + \alpha\beta \tag{3-26}$$

$$v = \alpha - \beta \tag{3-27}$$

$$\Im = a + a_1 - \beta b \tag{3-28}$$

$$\eta = b + a_2 + \beta a \tag{3-29}$$

The coordinates of the points $P_0 = (x_0, y_0)$, $P_1 = (x_1, y_1)$, $P_2 = (x_2, y_2)$ are

$$x_1 = a_1 + \frac{t_1}{2} \tag{3-30}$$

$$y_1 = c\, t_1^2 + \frac{1}{2c} + a_2 \tag{3-31}$$

$$x_0 = a_1 - \frac{t_0^2}{2t_1} + t_0 \tag{3-32}$$

$$y_0 = 0 \tag{3-33}$$

$$x_2 = a_1 + a + \tau_1 + \frac{d\beta}{\tau_1} + d\beta\tau_1 - \frac{\alpha d}{\tau_1} - b\beta \tag{3-34}$$

$$y_2 = a_2 + b + \beta\tau_1 + \beta a - \frac{d}{\tau_1} - \alpha\tau_1 - \frac{\alpha\beta d}{\tau_1} \tag{3-35}$$

Since $d_1 = 2x_1 = 2a_1 + t_1$, if we put $d_1 = 1$, we can consider a_1 as an intermediate coefficient given by the formula

$$a_1 = \frac{1}{2}(1 - t_1) \tag{3-36}$$

since p_2 is in the right half plane, $x_2 > 0$ or

$$a_1 + a_2 + \tau_1 + \frac{d\beta}{\tau_1} + \alpha\beta\tau_1 - \frac{\alpha d}{\tau_1} - b\beta > 0 \tag{3-37}$$

Equations for the Curve

Parabolic part $(y_1 \geq y \geq 0,\ x_0 \leq x \leq x_1)$

$$\left(1+\beta^2\right)\left[(y-a_2) - \beta(x-a_1)\right] = c\left[(x-a_1) + \beta(y-a_2)\right]^2 \tag{3-38}$$

Hyperbolic part $(0 \geq y \geq y_2,\ x_2 \leq x \leq x_0)$

$$\left[u(x-\Im) - v(y-\eta)\right]\left[v(x-\Im) + u(y-\eta)\right] + d\left(u^2+v^2\right)^2 = 0 \tag{3-39}$$

Example: let $c = 0.1$, $d = 1$, $\tau_0 = 1$, $t_0 = 5$, $\tau_1 = 0.5$, $a_1 = 0$

then

$$\alpha = 0,\ a = 4,\ b = 3.5,\ t_1 = 20,\ a_2 = -3.75,\ \beta = 0.25,$$
$$u = 1,\ v = -0.25,\ \xi = 3.125,\ \eta = 0.75$$

$$\begin{cases} x_1 = 10 \\ y_1 = 41.25 \end{cases} \qquad \begin{cases} x_0 = 4.375 \\ y_0 = 0 \end{cases} \qquad \begin{cases} x_2 = 4.125 \\ y_2 = -1.125 \end{cases}$$

Equations

1. Parabolic part

$$10.625 \bullet [y + 3.75 - 0.25x] - [x + 0.25(y + 3.75)]^2 = 0$$

2. Hyperbolic part

$$[(x - 3.125) + 0.25(y - 0.75)][(y - 0.75) - 0.25(x - 3.125)] - (1.0625)^2 = 0$$

The ratio of diameters = $x_1 : x_2 = 10 : 4.123 \approx 2.5$

3.4 Experimental Results

Holographic optical elements have a unique property in that they can both spatially and spectrally transform a beam distribution. An example of this is a concentrator which focuses only on a range of wavelengths, allowing all others to be transmitted unaltered. One type of structure which has many applications is a volume grating. Figure 3-13 shows a typical volume transmission grating. POC has fabricated gratings with several types of index modulation, including sinusoidal, rectangular and triangular; having an index modulation as high as 0.2. The highest diffraction efficiency demonstrated is ~97.9% for s-polarization. The wavelength range is limited by the dichromated gelatin material, from ~360 nm to 2.8 μm.

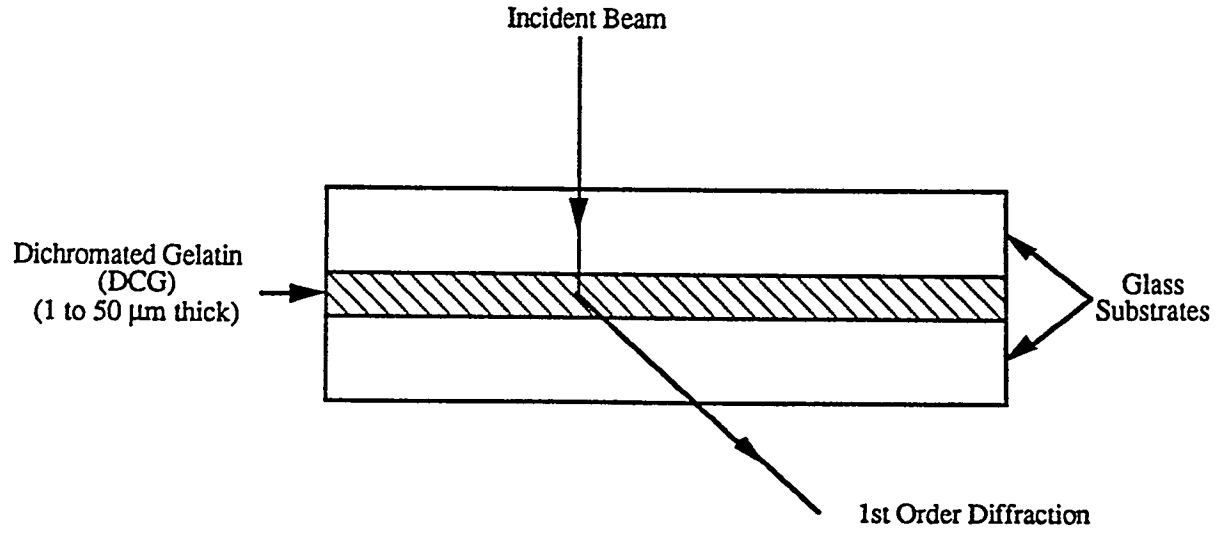

Figure 3-13
Illustration of a Typical Volume Holographic Transmission Grating Structure

A prototype beamsplitting and wavelength division multiplexing (WDM) grating hologram was fabricated to separate a combined beam of red (632.8 nm) and green (543 nm) HeNe laser light (as shown in Figure 3-14). When the combined beam was launched into the hologram, the green beam was separated, with about 50% of the light being transmitted through the hologram and the rest being distributed throughout the other gratings. There was no effect on the red beam, which was 100% transmitted through the hologram at the incident angle. By changing the angle of incidence, it was possible to have the red beam separated out, and the green beam 100% transmitted through the hologram. The efficiency of this exploratory prototype is low, however, further improvement is possible.

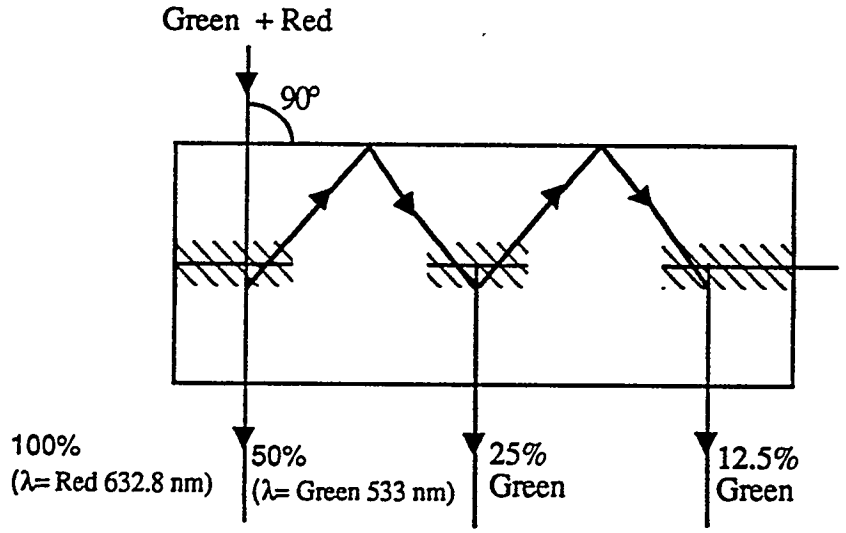

Figure 3-14
Multiple Holographic Grating for Use in Beamsplitting and
Wavelength Division Multiplexing Applications

Figure 3-15 illustrates the circular-to-circular beam distribution formation property of a non-imaging optic (NIO). (Currently, POC has NIOs for transforming the highly divergent light from 100, 200 and 400 μm fibers into nearly collimated (within 3°) large diameter beams. These can be incorporated with the grating beamsplitting/WDM holograms to create efficient and compact fiber optic WDMs.)

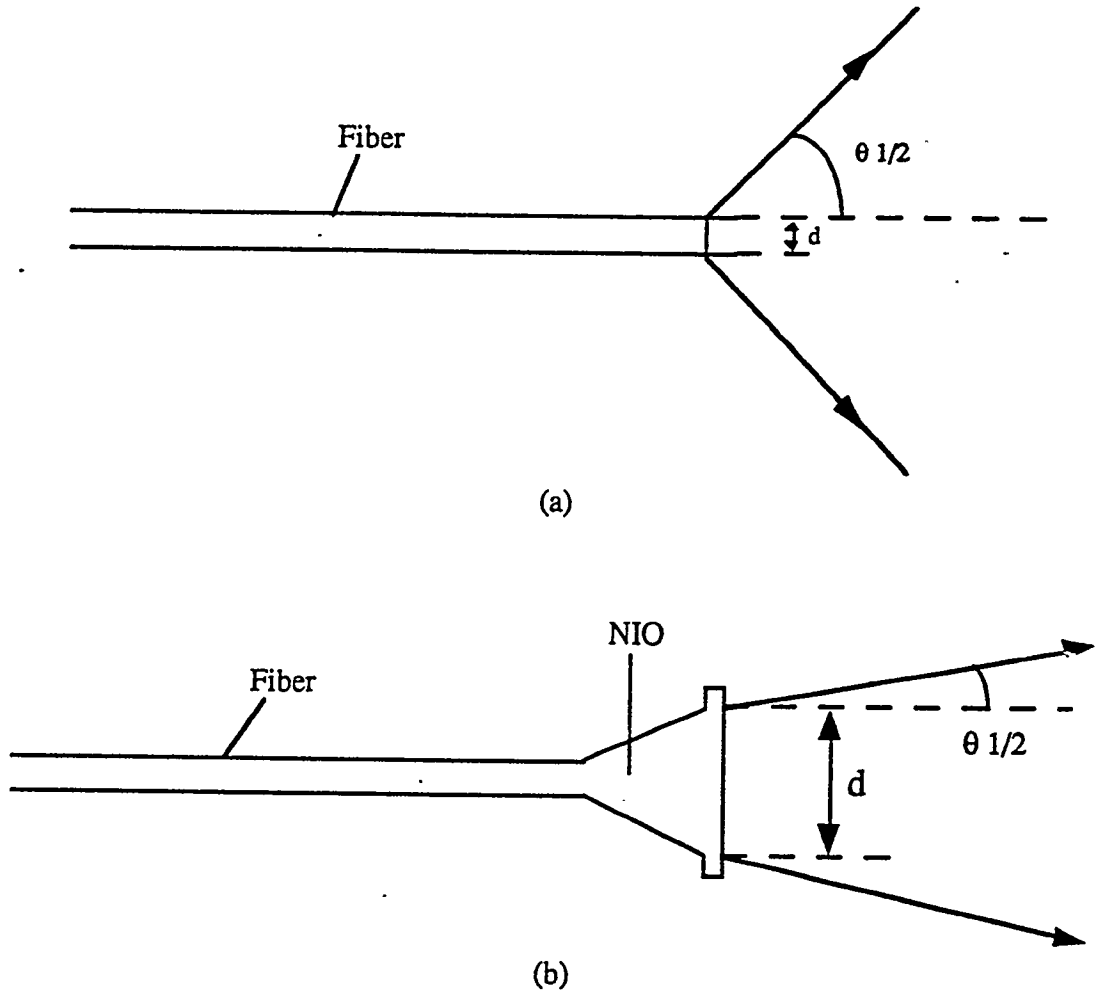

Figure 3-15
Beam Distribution Formation Property of NIO: (a) Highly Divergent Output of a Solitary Fiber, (b) Nearly Collimated Output of the Fiber-NIO Combination.

As reported earlier, HOEs for NIO applications such as couplers and WDM's have been demonstrated using DCG volume holograms recorded on separate films and multiplexed by stacking them together. Demonstration HOEs for 3 to 4 wavelength WDMs have been fabricated having efficiencies of up to 98% with approximately 10% cross-talk. Also, by using a similar concept, 1 to 4 couplers for single wavelength (e.g., 633 nm) have been fabricated. However, due to the additive nature of each layer, HOEs thus fabricated showed high background absorption and noise. This noise will increase with the increase in the number of wavelengths or channels. One way to avoid this drawback is to multiplex the holograms in one volume (i.e., in one film), thus the background and noise will be just that of one holographic layer. Multiplexing, however introduces a reduction in the efficiency by a factor of $\frac{1}{N}$ where N is the number of holograms

multiplexed together. This is unacceptable if high efficiency - high number of channels are required. Also, the designed architecture is not suitable for packaging into a compact unit due to the diversity of angles associated with channels.

Due to these drawbacks, POC has studied the alternative HOE design approach for couplers and WDM applications. The device is based on a set of coupled holograms fabricated on a single substrate. By making slanted gratings and total internal reflection (TIR), the two holograms act like a conjugate pair for a normally incident (collimated) input beam into several output beams also emerging normal to the substrate. This device can be used for both one to many channel couplers and for many wavelength WDMs. The operation of the device is shown in Figure 3-16(a) and (b).

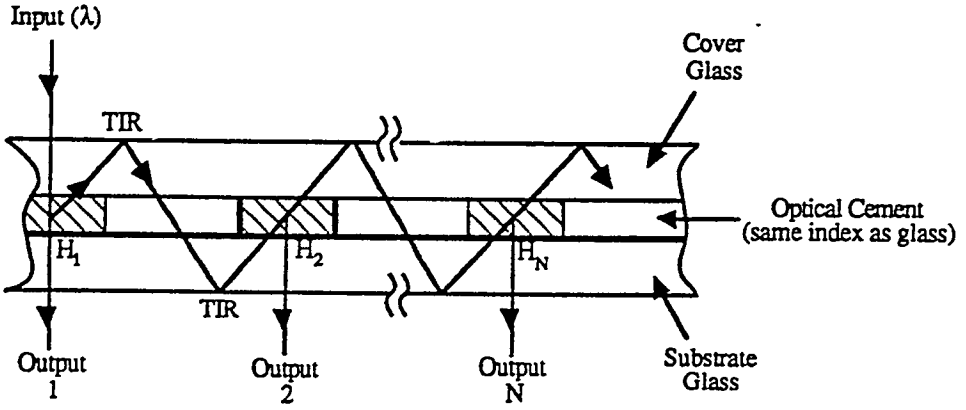

(a) 1 to N Coupler

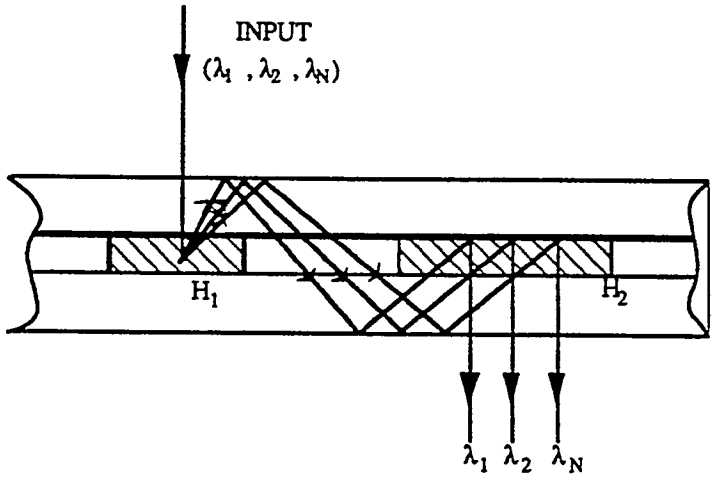

(b) n-channel WDM

Figure 3-16
Integrated Coupled Holograms and TIR for (a) Power Splitting, and (b) Wavelength Splitting (WDM) Applications

As depicted in Figure 3-16, a single slanted TIR hologram recording geometry was used for both devices. By recording holograms (or a single hologram) and laminating it with a glass cover plate, (using optical cement of the same index as glass), a monolithic device is obtained for both a one to many coupler and for WDM applications.

In the case of a 1 to N coupler, the hologram slant angle is designed for a Bragg reflection at the desired wavelength λ (e.g., 633 nm), and the efficiencies of the individual holograms are adjusted by selective exposure to change both index modulation Δn and the average index $\bar{n}$ of the recording material. Several experiments have been completed to characterize the material response to exposures so that peak wavelengths and efficiencies of holograms can be adjusted to the required values. We have fabricated a demonstration model for a 1 to 4 coupler which has a power uniformity of within 10% and a total device efficiency of ~80%. Further studies and effort would increase this efficiency to 95% and beyond.

For the WDM application, as described in Figure 3-16(b), only a single hologram needs to be recorded. This hologram should have a bandwidth covering the range of wavelengths (λ_1, λ_2,...λ_n) at considerably high efficiencies (~90%).

Such holograms have been fabricated and demonstrated in POC's labs and have been used as a Littrow grating in POC's WDM devices [29]. For this approach, similar dispersion properties of the grating are used, together with its "conjugate" pair (obtained by cutting out a strip of hologram and laminating it with a cover glass plate), to produce a spatially separated but normal output beam at different wavelengths.

Currently, material characterization and optimization of recording parameters are being continued to achieve the required bandwidth, efficiency and high signal to noise ratio.

4.0 REFERENCES

1. A. Walther, "Radiometry and coherence," J. Opt. Soc. Am., 58, 1256 (1968).

2. A. Walther, "Radiometry and coherence," J. Opt. Soc. Am., 63, 1622 (1973).

3. A. Walther, "Propagation of the generalized radiance through lenses," J. Opt. Soc. Am., 68, 1606-1611 (1978).

4. E. W. Marchand and E. Wolf, "Radiometry with sources of any state of coherence," J. Opt. Soc. Am., 64, 1219-1226 (1974).

5. E. W. Marchand and E. Wolf, "Walther's definition of generalized radiance," J. Opt. Soc. Am., 64, 1273-1274 (1974).

6. W. H. Carter and E. Wolf, "Coherence properties of Lambertian and non-Lambertian sources," J. Opt. Soc. Am., 65, 1067-1071 (1975).

7. W H. Carter and E. Wolf, "Coherence and radiometry with quasi-homogeneous planar sources," J. Opt. Soc. Am., 67, 785 (1977).

8. E. W. Marchand and E. Wolf, "Radiometry with sources of any state of coherence," J. Opt. Soc. Am., 64, 1219 (1974).

9. E. Wolf, "The radiant intensity from planar sources of any state of coherence," J. Opt. Soc. Am., 68, 1597-1605 (1978).

10. A. T. Friberg, "On the existence of a radiance function for finite planar sources of arbitrary states of coherence," J. Opt. Soc. Am., 69, 192-199 (1979).

11. T. Jannson, "Radiance transfer function," J. Opt. Soc. Am., 70, 1544-1549 (1980).

12. E. Wolf, "Coherence and Radiometry," J. Opt. Soc. Am., 68, 6-17 (1978).

13. T. Jannson, "Self-imaging effect in physical radiometry," J. Opt. Soc. Am., 73, 402-409 (1983).

14. E. W. Marchand and E. Wolf, "Generalized radiometry for radiation from partially coherent sources," Opt. Comm., 6, 4 (1972).

15. P. DeSantis, F. Gori, G. Guattari, and C. Palma, "An example of a Collet-Wolf source," Opt. Comm., 29, 2, 256-260 (1979).

16. E. Collet, J. Foley, and E. Wolf, "On an investigation of Tatarskii into the relationship between coherence theory and the theory of radiative transfer," J. Opt. Soc. Am., 67, 465-467 (1977).

17. F. Gori and E. Wolf, "Sources with factorized cross-spectral densities," Opt. Comm., 61, 6, 369-373 (1987).

18. E. Wolf and W. H. Carter, "A radiometric generalization of the Van Cittert Zernike theorem for fields generated by sources of arbitrary state of coherence," Opt. Comm., 16, 3, 297-302 (1976).

19. E. Wolf, "New theory of partial coherence in the space-frequency domain. Part I: spectra and cross spectra of steady state sources," J. Opt. Soc. Am., 72, 2 (1982).

20. E. Wolf, "New theory of partial coherence in the space-frequency domain. Part II: steady state fields and higher order correlations," J. Opt. Soc. Am. A, 3, 1, 76-85 (1986).

21. E. Wolf, "Coherent-mode propagation in spatially band-limited wave fields," J. Opt. Soc. Am. A, 3, 11, 1920-1924 (1986).

22. W. H. Carter and E. Wolf, "Inverse problem with quasi-homogeneous sources," J. Opt. Soc. Am. A, 2, 11, 1994-2000 (1985).

23. G. S. Agarwal, J. T. Foley, and E. Wolf, "The radiance and phase-space representations of the cross-spectral density operator," Opt. Comm., 62, 2, 67-72 (1987).

24. K. J. Kim, "Brightness, coherence and propagation characteristics of synchrotron radiation," Nucl. Instr. and Methods, A246, 71 (1986).

25. T. Jannson, L. Sadovnik, T. Aye, I. Tengara, "Radiometric ray tracing," JOSA Dec. 1991, Proc. of the 1991 OSA Annual Meeting, San Jose, CA, Nov. 1991; MCC4.

26. T. Jannson, I. Tengara, and D. Erwin, "Semigeometrical phase-space trajectories in physical radiometry," in preparation.

27. R. Simon, E. Wolf, "Transfer of radiance by Gaussian-Schell Model beams in paraxial system," submitted to JOSA.

28. R. K. Luneburg, *Mathematical theory of optics* (University of California, Berkeley, 1966).

29. T. Jannson, I. Tengara, "Lippmann-Bragg broadband holographic mirrors," JOSA A, 8, 201 (1991).

30. E. Wolf, J. Jannson, T. Jannson, "Analogue of the van Cittert Zernike theorem for statistically homogeneous wave fields," Opt. Lett. 15, 1032 (1990).

31. H. Kogelnik and T. Li, "Laser beams and resonators," Appl. Opt., 5, 1550-1567 (1966).

32. See, for example, M. Born and E. Wolf, *Principles of optics* (Pergamon Press, Section 4.8, 1970).

33. D. Marcuse, *Light transmission optics* (Academic Press, 1970).

34. T. Jannson and R. Winston, "Liouville theorem and concentrator optics," J. Opt. Soc. Am. A, 3, 7 (1986).

35. W. T. Welford and R. Winston, *The optics of non-imaging concentrators* (Academic Press, 1978).

36. H. P. Baltes, J. Geist, and A. Walther, *Radiometry and coherence*, in Topics in Current Physics, 9, edited by H. P. Baltes (Springer, Berlin, 1978).

37. J. T. Foley and E. Wolf, "Radiance function of partially coherent fields," J. Mod. Opt., 38, 2053-2068 (1991).

38. A. T. Friberg, G. S. Agarwal, J. T. Foley, and E. Wolf, "Statistical wave-theoretic derivation of the free-space transport equation of radiometry," J. Opt. Soc. Am. B (in press).

39. E. Wigner, "On the quantum correction for the thermodynamic equilibrium," Phys. Rev., 40, 749-759 (1932).

40. M. J. Bastiaan, "Wigner distribution function and its application to first-order optics," J. Opt. Soc. Am., 69, 1710-1716 (1979).

41. S. Creagh and R. Littlejohn, "Semiclassical trace formulas in the presence of continuous symmetries," Phys. Rev. A, 44, 836-850 (1991).

42. A. M. Kondratienko and A. N. Skrinsky, Opt. Spectrosc., 42, 189 (1977).

43. G. Nemez, I. E. Teoderescu, and M. Nemez, "Phase space treatment of optical beams," Proc. 3rd Int. School of Coherent Optics (Bucharest, Rumania, Aug. 30-Sept. 8, 1982).

44. J. W. Goodman, *Introduction to Fourier optics* (McGraw-Hill, 1968).

45. J. W. Goodman, *Statistical optics* (Wiley, 1985).

46. C. Kunz and K. Codling, *Synchrotron Radiation, Techniques and Applications* (Springer, Berlin, 1979).

47. E. Tegeler, German National Lab. (German equivalent to U.S. NIST), Private Communication, February 1992.

48. G. Gloge and D. Marcuse, "Formal quantum theory of light rays," J. Opt. Soc. Am., 59, 1629-1631 (1969).

49. G. Eichmann, "Quasi-geometric optics of media with inhomogeneous index of refraction," J. Opt. Soc. Am., 61, 161-168 (1971).

50. T. Jannson and R. Janicki, "An eigenvalue formulation of inverse theory of scalar diffraction," Optik, 56, 429-441 (1980).

51. T. Jannson, "Information capacity of Bragg holograms in planar optics," J. Opt. Soc. Am, 71, 342 (1982).

52. T. Jannson, H. Stoll, and C. Karaguleff, "The interconnectability of neuro-optic processors," SPIE Proc., 698, 157-169 (1986).

53. See, for example, J. R. Klauder and E. C. Sudharshan, *Fundamentals of quantum optics* (Benjamin Inc. 1968).

54. L. Brilbuin, *Science and information theory* (Academic Press, 1956).

55. A. J. Lichtenberg, *Phase space dynamics of particles* (Wiley, New York, 1969).

56. See also, M. Planck, *The theory of heat radiation* (Dover, New York, 1959).

57. L. Allen and J. H. Eberly, *Optical Resonance and Two-Level Atoms* (Wiley, New York, 1975).

58. H. A. Kramers, "Quantentheorie des elektrons und der strahlung in hand- und jahrbuch der chemischen physik," Eucken-Wolf (Leipzig, 1938) (English translation, Quantum Mechanics (Amsterdam, North Holland, 1957)).

59. E. Wolf, "New theory of radiation energy transfer in free electromagnetic fields," Phys. Rev. D, 13, 869 (1976).

60. E. C. G. Sudarshan, "Quantum electrodynamics and light rays," Physica A, 96, 315-320 (1981).

61. E. C. G. Sudarshan, "Quantum theory of radiative transfer," Phys. Rev. A, 23, 2803-2809 (1981).

62. L. V. Bourimborde, W. D. Furlan, and E. E. Sicre, "Off-axis analysis of the Strehl ratio using the Wigner distribution function," J. Mod. Opt., 38, 1685-1689 (1991).

63. V. P. Maslov, Asimptoticheskije metody i teoria vozmushchenij (Nauka, Moskva, 1988 (in Russian)).

64. V. Guillemin and S. Sternberg, "Geometric Asymptotics," Mathematical Surveys, 14, America Mathematical Society (Providence, RI, 1977).

65. H. E. Moses, R. J. Nagem, and G. V. H. Sandri, "The general solution of the three-dimensional acoustic equation and of Maxwell equations in the infinite domain in terms of the asymptotic solution in the wave zone," J. Math. Phys., 33, 86-101 (1992).

66. I. Bialynicki-Birula, Z. Bialynicka-Birula, and G. Alamone, "Spatial antibunching of photons," Phys. Rev. A, 43, 3696-3703 (1991).

67. L. S. Schulman, *Techniques and applications of path integration* (Wiley, New York, 1981).

68. C. DeWitt, A. Maheshwari, and B. Nelson, "Path integration in non-relativistic quantum mechanics," Phys. Rep., 50, 255-372 (1979).

69. L. Allen, and J. H. Eberly, *Optical resonance and two-level atoms* (Wiley, New York, 1975).

70. F. T. Arecchi, "Order and chaos in quantum optics," in *Coherence, Cooperation and Fluctuations*, Eds. F. Haake, L. M. Narducci, and D. F. Walls (Cambridge University Press, Cambridge, 1986).

71. S. Winick and S. Doniach, *Synchrotron Radiation Research* (Plenum, New York, 1980).

72. E.-E. Koch, *Handbook of Synchrotron Radiation* (North-Holland, Amsterdam, 1983).

73. G. Margaritondo, *Introduction to Synchrotron Radiation* (Oxford, New York, 1988).

74. J. Thomas, G. Jezequel, and I. Pollini, "Determination of the optical properties of absorbing uniaxial crystals from multiangle reflections with polarized synchrotron radiation," J. Opt. Soc. Am. A, 6, 27 (1989).

75. P. A. Lee, P. H. Citrin, P. Eisenberger, and B. M. Kincaid, "Extended x-ray absorption fine structure --- its strengths and limitations as a structural tool," Rev. Mod. Phys., 53, 769 (1981).

76. M. O. Krause, "Photoionization of atoms and molecules using synchrotron radiation," IEEE Trans. Nuclear Sci., NS-28, 1215 (1981).

77. B. K. Tanner and D. K. Bowen, *Characterization of Crystal Growth Defects by X-Ray Methods* (Plenum, New York, 1981).

78. H. Takada, K. Furukawa, and T. Tomimasu, "Development of a compact synchrotron radiation system for x-ray lithography," Opt. Eng., 27, 550 (1988).

79. E. Hughes, H. D. Zeman, L. E. Campbell, R. Hofstadter, U. Meyer-Berkhout, J. N.Otis, J. Rolfe, J. P. Stone, S. Wilson, E. Rubinstein, D. C. Harrison, R. S. Kernoff, A. C. Thompson, and G. S. Brown, "The application of synchrotron radiation to non-invasive angiography," Nucl. Instr. and Methods, 208, 665 (1983).

80. M. R. Howells, M. A. Iarocci, and J. Kirz, "Experiments in x-ray holographic microscopy using synchrotron radiation," J. Opt. Soc. Am. A, 3, 2171 (1986).

81. K. J. Kim, "Brightness and coherence of synchrotron radiation and high-gain free electron lasers," Proc. VIIth National Conf. on Synchrotron Radiation (SR-86), Novosibirsk, 1986.

82. T. Jannson, G. Savant, and Y. Qiao, "Bragg holographic structures for XUV applications, a new approach," Opt. Lett., 14, 344 (1989).

83. T. Jannson, G. Savant, and L. Wang, "Extreme-ultraviolet Bragg holographic structures: theory and experiments," J. Opt. Soc. Am. A, 8, 1587 (1991).

84. T. Jannson, "Holographic technology for solar energy concentration," Final Report #DE-AC03-81ER10836 (July 1984).

85. Y. Kitugawa, et al., "Demonstration of collisionally enhanced degenerate four wave mixing in a plasma," Phys. Rev. Lett., 62, 151 (1989).

86. E. Wolf, "New theory of radiative energy transfer in free electromagnetic fields," Phys Rev., 13, 869 (1976).

87. V. I. Tatarskii, "The effects of the turbulent atmosphere on wave propagation," Israel Program for Scientific Translation (Jerusalem, 1971).

88. J. Winthrop, "Propagation of structural information in optical wave fields," J. Opt. Soc. Am., 61, 15 (1971).

89. D. Gabor, "Light and information," Progress in Optics, Vol. I ed. E. Wolf (North Holland, 1960).

90. M.Z. Zubairy, and E. Wolf, "Exact equations for radiative transfer of energy and momentum in free electromagnetic fields," Opt. Comm., 20, 321 (1977).

APPENDIX A

DENSITY MATRIX, GENERALIZED RADIANCE FUNCTION, SPATIAL COHERENCE AND LIOUVILLE THEOREM

A.1 Introduction

The purpose of this appendix is to show mutual relations among the radiance function, the density matrix and spatial coherence, based on a formal analogy between 3-D physical optics and 3-D quantum mechanics. It has been shown that 3-D monochromatic Maxwell equations with the z coordinate as a parameter [33,49] are fully equivalent to the spinor matrix equation that is formally identical with the 3-D Dirac relativistic equation, if we apply the following formal substitutions:

$$\hbar \rightarrow \lambda\!\!\!^{-}, \text{ where } \lambda\!\!\!^{-} = \lambda/2\pi \tag{A-1a}$$

$$t \rightarrow z \tag{A-1b}$$

$$V \rightarrow -n \tag{A-1c}$$

$$m \rightarrow n_0$$

where V is scalar potential energy. It has also been shown [48] that the paraxial (diffusion) approximation in physical optics is formally equivalent to the non-relativistic approximation in quantum mechanics, and the first quantization of optics has been demonstrated.

Based on this analogy, we can introduce the optical ("relativistic") Hamiltonian, in the form

$$\hat{H} = -\left(n^2 - \hat{p}_x^2 - p_y{}^2\right)^{1/2} \tag{A-2}$$

where $\hat{p}_x = -i\lambda\!\!\!^{-}\frac{\partial}{\partial x}$, $\hat{p}_y = -i\lambda\!\!\!^{-}\frac{\partial}{\partial y}$, and using

$$\hat{H} = i\lambda\!\!\!^{-}\frac{\partial}{\partial z} \tag{A-3}$$

we obtain the optical analog of the Klein-Gordon equation [48]:

$$\frac{\partial^2 u}{\partial x^2} + \frac{\partial^2 u}{\partial y^2} + \frac{\partial^2 u}{\partial z^2} + \left(\frac{n}{\lambda\!\!\!^{-}}\right)^2 u = 0 \tag{A-4}$$

which is the Helmholtz equation with $\lambda\!\!\!^{-} = \lambda/2\pi = 1/k$. In the paraxial ("non-relativistic") approximation, the optical Hamiltonian is

$$\hat{H} = \frac{1}{2n_o}\left(\hat{p}_x^2 + p_y^2\right) - n \qquad \text{(A-5)}$$

where $n \cong n_o$, and $\hat{p}_x = n\dot{x}$, $\hat{p}_y = n\dot{y}$, where $\dot{x} = \frac{dx}{dz}$, $\dot{y} = \frac{dy}{dz}$. Using Eqs. (A-3), and (A-5), we obtain the optical analog of the Schroedinger equation:

$$\hat{H}u = i\lambda\frac{\partial u}{\partial z} \text{ or} \qquad \text{(A-6a)}$$

$$\frac{\partial^2 u}{\partial x^2} + \frac{\partial^2 u}{\partial y^2} + \frac{2in_o}{\lambda}\frac{\partial u}{\partial z} + \frac{2n_o n}{\lambda^2}u = 0 \qquad \text{(A-6b)}$$

which is the paraxial monochromatic wave equation. The paraxial energy eigenvalue equation is

$$\hat{H}u = Eu \qquad \text{(A-7)}$$

where the optical Hamiltonian is defined by Eq. (A-5). For the optical analog of a stationary state in quantum mechanics, we have a 2-D index spatial distribution in the form:

$$n = n(x,y) \qquad \text{(A-8)}$$

and

$$u(x,y;z) = \psi(x,y)\ \exp i(Ez/\lambda) \qquad \text{(A-9)}$$

where

$$k_z = ks_z = E/\lambda = kE \qquad \text{(A-10a)}$$

Thus,

$$E = s_z \qquad \text{(A-10b)}$$

i.e., the optical analog of the energy is the z-component of the unit vector of propagation, $\vec{s}$. For the discrete eigenstates, the Hamiltonian eigenequation is

$$\hat{H}\psi_n = E_n\psi_n \qquad \text{(A-11)}$$

Therefore, in the stationary case (A-8), the stationary Schroedinger equation (A-6b) is equivalent to the Hamiltonian eigenequation (A-7) or (A-11).

A.2 Stationary State

This stationary Schroedinger equation, either in the discrete or the continuous case, has many applications in optics. Specifically, for the discrete case, we have the following interesting cases:

1. Parabolically Focusing Medium

In this case,

$$n = 1 - n_1 \tag{A-12}$$

where

$$n_1 = \frac{1}{2} w^2 x^2 \tag{A-13}$$

and the eigenfunctions are well-known Gaussian modes of the harmonic oscillator [31].

2. Nonlinear Oscillator

In this case,

$$n_1 = \frac{1}{2} w^2 x^2 + \beta x^3 + \ldots \tag{A-14}$$

or, in the 2-D general case,

$$n = n_o + n_1 x + n_2 y + n_3 x^3 + n_4 xy + n_5 y^2 \tag{A-15}$$

In general, this describes some aberration-related cases. By analogy to classical mechanics, it would be interesting to identify some nonlinear oscillating cases with chaotic behavior.

3. *Laser Resonator*

In this case, we would obtain, for example, some characteristics modes of a curved mirror laser oscillator [31].

4. *Fabry-Perot Etalon*

In this case, we obtain sinusoidal eigenfunctions [49].

5. *Cylindrical Optics*

In the general cylindrical optics case, we have n = n(x,y). Using typical quantum mechanic substitutions

$$\hat{H} = \frac{\hat{p}^2}{2n_o} - n = -\frac{\lambda^2}{2n_o}\nabla^2 - n \qquad \text{(A-16)}$$

Eq. (A-6b) reduces to

$$\frac{\partial^2\psi}{\partial x^2} + \frac{\partial^2\psi}{\partial y^2} + \frac{2n_o}{\lambda^2}(n - E)\,\psi = 0 \qquad \text{(A-17)}$$

Obviously, there is an infinity of cases that can be solved and experimentally realized, using modern methods of integrated optics . The most interesting special cases are

a. Channel waveguide arrays
b. Planar optics
c. Fiber arrays

A.3 Non-Stationary State

We can consider the case where refractive index varies slowly with z:

$$\frac{\partial n}{\partial z} \equiv 0 \qquad \text{(A-18)}$$

This situation would be an analog of the adiabatic case in quantum mechanics. The strong z-dependence of n will be equivalent to the strongly relativistic case in quantum mechanics; then, the Dirac equations will be necessary. In such a case, however, we can expect some Fresnel reflections in the opposite z-direction, with no obvious analogy to the quantum mechanical case ("time" passing in *two* opposite directions).

A.4 Semi-Geometrical Case

In quantum mechanics, the classical asymptotic approximation is realized by the relation

$$\hbar \to 0 \qquad \text{(A-19)}$$

By analogy, the asymptotic geometrical optics approximation is obtained by

$$\lambda \to 0 \qquad \text{(A-20)}$$

The interesting novelty here is that the limit (20) can be realized not only formally as in Eq. (A-19) but also physically, by providing optical sources with shorter optical wavelengths. Polychromatic optics does not have a quantum mechanical analogy, with the possible exception of Sudharsan's approach [60,61].

A.5 Mixed States, Density Matrix and Spatial Coherence

So far, we have considered only "pure" quantum mechanical states. In physical (statistical) optics, the "mixed" states are described by an ensemble of complex amplitudes, $\{\dots\}_{ens}$. Since they are the statistical realization of the ensemble, those complex amplitudes are more or less spatially correlated through the cross-spectral density function:

$$W(\vec{r}_1,\vec{r}_2)=\left\{u^*(\vec{r}_1)\,u(\vec{r}_2)\right\}_{ens} \tag{A-21}$$

defined by Wolf [12], where the complex degree of spatial coherence is

$$\mu(\vec{r}_1,\vec{r}_2)=\frac{\left\{u^*(\vec{r}_1)\,u(\vec{r}_2)\right\}_{ens}}{\sqrt{I(\vec{r}_1)}\sqrt{I(\vec{r}_2)}} \tag{A-22}$$

and $I(\vec{r})=W(\vec{r},\vec{r})$ is optical intensity.

Following the quantum-mechanical analogy (see, for example, Ref. [53]), we introduce the density operator $\hat{\rho}$ in the form:

$$\hat{\rho}\equiv\left\{|u\rangle\langle u|\right\}_{ens} \tag{A-23}$$

where Dirac notation is used.

In the space domain, the density matrix is

$$\begin{aligned}\rho_{ij}&=\langle\vec{r}_j|\hat{\rho}|\vec{r}_i\rangle=\langle\vec{r}_j|\left\{|u\rangle\langle u|\right\}_{ens}|\vec{r}_i\rangle\\&=\left\{\langle\vec{r}_j|u\rangle\langle u|\vec{r}_i\rangle\right\}_{ens}=\left\{u^*(\vec{r}_i)\,u(\vec{r}_j)\right\}_{ens}\end{aligned} \tag{A-24}$$

Comparing Eq. (A-21) with Eq. (A-24), we obtain

$$\rho_{ij}=W_{ij} \tag{A-25}$$

i.e., *density matrix in physical optics is identical to the cross-spectral density function representing the spatial coherence of the monochromatic optical field.* Considering the inverse analogy of 3-D quantum mechanics to 3-D physical optics, we can say that the quantum-mechanical density matrix characterizes the spatial coherence of the quantum mechanical wave functions.

It is easy to show that the density operator $\hat{\rho}$ is hermitian:

$$\hat{\rho}^{+} = \hat{\rho} \tag{A-26}$$

and, introducing the orthonormal (discrete) eigenbasis,

$$\hat{\rho}\,|\Phi_n\rangle = \lambda_n |\Phi_n\rangle \tag{A-27}$$

where

$$\langle \Phi_n | \Phi_{n'} \rangle = \delta_{nn'} \tag{A-28a}$$

and

$$\sum_n |\Phi_n\rangle \langle \Phi_n| = \hat{I} \tag{A-28b}$$

where $\hat{I}$ is unity operator. We obtain

$$\langle \Phi_{n'} | \hat{\rho} | \Phi_n \rangle = \lambda_n \, \delta_{nn'} \tag{A-29}$$

where $\delta_{nn'}$ is Kronecker delta.

Using Eqs. (A-28b), (A-24), and (A-29), we obtain

$$\begin{aligned} \langle \vec{r}_1 | \hat{\rho} | \vec{r}_2 \rangle &= \sum_n \sum_{n'} \langle \vec{r}_1 | \Phi_n \rangle \langle \Phi_n | \hat{\rho} | \Phi_{n'} \rangle \langle \Phi_{n'} | \vec{r}_2 \rangle \\ &= \sum_n \sum_{n'} \langle \vec{r}_1 | \Phi_n \rangle \lambda_n \delta_{nn'} \langle \Phi_{n'} | \vec{r}_2 \rangle \\ &= \sum_n \langle \vec{r}_1 | \Phi_n \rangle \lambda_n \langle \Phi_n | \vec{r}_2 \rangle \end{aligned} \tag{A-30}$$

This is the discrete analog of the Mercer theorem [50]. In the operator form, we have

$$\hat{\rho} = \sum_n |\Phi_n\rangle \lambda_n \langle \Phi_n| \tag{A-31}$$

Using Eqs. (A-28a) and (A-29) and the completeness relation,

$$\iint |\vec{r}\rangle \langle \vec{r}\,| \, d^2 r = \hat{I} \tag{A-32}$$

we obtain the following expression for the density matrix trace

$$\begin{aligned} T_r\hat{\rho} &= \iint \langle \vec{r} | \hat{\rho} | \vec{r} \rangle \, d^2r = \iint \sum_n \langle \vec{r} | \Phi_n \rangle \, \lambda_n \, \langle \Phi_n | \vec{r} \rangle \, d^2r \\ &= \sum_n \iint \lambda_n \, \langle \Phi_n | \vec{r} \rangle \, \langle \vec{r} | \Phi_n \rangle \, d^2r \\ &= \sum_n \lambda_n \, \langle \Phi_n | \Phi_n \rangle = \sum_n \lambda_n \end{aligned} \tag{A-32b}$$

It is seen from Eq. (A-24) that

$$W(\vec{r},\vec{r}) = \langle \vec{r} | \hat{\rho} | \vec{r} \rangle \doteq I(\vec{r}) \tag{A-33}$$

i.e., the *optical intensity is identical to the diagonal component of the density component,* and, in the paraxial (non-relativistic) approximation

$$F = \iint I(\vec{r}) \, d^2r = T_r\hat{\rho} = \iint \langle \vec{r} | \hat{\rho} | \vec{r} \rangle \, d^2r \tag{A-34}$$

i.e., *paraxial radiation flux is identical with the density matrix trace.*

Consider the density matrix representation in eigenstate functions of some operator

$$\langle \psi_n | \hat{\rho} | \psi_{n'} \rangle = \{ \langle \psi_n | u \rangle \, \langle u | \psi_{n'} \rangle \}_{ens} \tag{A-35}$$

or, in brief,

$$\rho_{n'n} = \{ a_n \, a^*_{n'} \}_{ens} = \rho_{n'n}(z) \tag{A-36}$$

where $a_n = \langle \psi_n | u \rangle$. Using the optical Hamiltonian in paraxial approximation:

$$\hat{H} = \frac{\hat{p}_x^2 + p_y^2}{2n_o} - n \tag{A-37}$$

where

$$\hat{p} = -i\lambda\hat{\nabla} \text{ and } \hat{p}^2 = -\lambda^2\Delta, \tag{A-38}$$

and using the Schroedinger equation

$$i\lambda\frac{\partial u}{\partial z} = \hat{H}u \tag{A-39}$$

we obtain

$$\frac{\partial \rho_{n'n}(z)}{\partial z} = \left\{\frac{\partial a_n}{\partial z}a_n^{*'} + \frac{\partial a_{n'}^{*}}{\partial z}a_n\right\}_{ens} \tag{A-40}$$

where

$$i\lambda\frac{\partial a_n}{\partial z} = \sum_n \left\langle m\middle|\hat{H}\middle|n\right\rangle a_n \tag{A-41}$$

and the matrix representation of the optical Hamiltonian is

$$\left\langle m\middle|\hat{H}\middle|n\right\rangle = \int\left\langle \psi_m\middle|\vec{r}\right\rangle \hat{H}\left\langle \vec{r}\middle|\psi_n\right\rangle d^2r \tag{A-42}$$

Eq. (A-40) in operator form is

$$i\lambda\frac{\partial \rho}{\partial z} = \hat{H}\hat{\rho} - \hat{\rho}\hat{H} = \left(\hat{H},\hat{\rho}\right) \tag{A-43}$$

where (...) is the quantum-mechanical Poisson bracket. Eq. (A-43) is well-known is non-relativistic quantum mechanics (see e.g., Ref. [53]) and describes the time evaluation of the density matrix. If the eigenvectors $\left|\psi_m\right\rangle$ are also the eigenvectors of the optical Hamiltonian, then Eq. (A-42) becomes

$$\begin{aligned}\left\langle m\middle|\hat{H}\middle|n\right\rangle &= \int\left\langle \psi_m\middle|\vec{r}\right\rangle \hat{H}\left\langle \vec{r}\middle|\psi_n\right\rangle d^2r \\ &= \int\left\langle \psi_m\middle|\vec{r}\right\rangle \lambda_m\left\langle \vec{r}\middle|\psi_n\right\rangle d^2n = \lambda_m\left\langle \psi_m\middle|\psi_n\right\rangle \\ &= \lambda_m\delta_{nm} = E_m\delta_{nm}\end{aligned} \tag{A-44}$$

and Eq. (A-40) simplifies to

$$i\lambda\frac{\partial\rho_{n'n}(z)}{\partial z} = (E_{n'} - E_n)\rho_{n'n}(z) \tag{A-45}$$

which can be easily integrated (see e.g., Ref. [53]). If for $z = 0$, $\rho_{n'n}(z) = \rho_{n'n}(0)$, then

$$\rho_{n'n(z)} = \exp\left[i(E_n - E_{n'})\frac{z}{\lambda}\right] \tag{A-46}$$

Substituting Eq. (A-10b) into Eq. (A-46) and using paraxial approximation

$$E = s_z = \sqrt{1-p^2} \cong 1 - \frac{p^2}{2} \tag{A-47}$$

Eq. (A-46) becomes

$$\rho_{n'n}(z) = \exp\left[i(s_{zn} - s_{zn'})\,kz\right] = \exp\left[ikz/2\left(p_{n'}^2 - p_n^2\right)\right] \tag{A-48}$$

i.e., in the stationary state described by Eqs. (A-8) to (A-10), the evolution of the optical density matrix is described by Eq. (A-48).

Using the Mercer theorem (30), we find that the density matrix factorizes only if a single eigenstate exists; i.e., $\lambda_n = \delta_{nm}$, and Eq. (A-30) reduces to the form

$$\langle\vec{r}_1|\hat{\rho}|\vec{r}_2\rangle = \langle\vec{r}_1|\Phi_m\rangle\langle\Phi_m|\vec{r}_2\rangle \tag{A-49}$$

It was shown by Gamo and Wolf [19,20] that in such cases the radiation is fully spatially coherent; i.e., $|\mu| = 1$.

A.6 Relation Between Density Matrix and Radiance Function in Paraxial Approximation

Using the complex radiance (brightness) definition [11] and Dirac notation, we obtain in paraxial approximation

$$B^{(+)}(\vec{r},\vec{p}) = \left\{\langle\vec{r}|u\rangle\langle u|\vec{p}\rangle\right\}_{ens}\langle\vec{p}|\vec{r}\rangle \tag{A-50}$$

where

$$\langle\vec{r}|u\rangle = u(\vec{r}),\ \langle u|\vec{p}\rangle = \tilde{u}^*(\vec{p}/\lambda), \text{ and } \langle\vec{p}|\vec{r}\rangle = \exp(-ik\vec{p}/\lambda) \tag{A-51}$$

Also, using Wolf's definition of Walthers' second definition of the complex radiance function (equivalent to Eq. (A-50)), we have

$$B^{(+)}(\vec{r},\vec{p}) \propto \iint W(\vec{r}',\vec{r})\exp\left[ik\vec{p}(\vec{r}'-\vec{r})\right]d^2r' \tag{A-52}$$

and using Eqs. (A-24) and (A-51), we obtain

$$B^{(+)}(\vec{r},\vec{p}) \propto \iint\langle\vec{r}|\hat{\rho}|\vec{r}'\rangle\langle\vec{r}'|\vec{p}\rangle\langle\vec{p}|\vec{r}\rangle d^2r' = \langle\vec{r}|\hat{\rho}|\vec{p}\rangle\langle\vec{p}|\vec{r}\rangle \tag{A-53}$$

i.e., the *complex radiance function can be interpreted as the density matrix in phase-space representation* $(\vec{r},\vec{p})$, *multiplied by the Fourier eigenfunction* $\langle\vec{p}|\vec{r}\rangle$.

In the quasi-homogeneous case, $B^{(+)} = B/2$, and the above property can be extended to the radiance function $B(\vec{r},\vec{p})$. In such a case, we obtain,

$$\iint B(\vec{r},\vec{p})\,d^2p = \iint\langle\vec{r}|\hat{\rho}|\vec{p}\rangle\langle\vec{p}|\vec{r}\rangle d^2p = \langle\vec{r}|\hat{\rho}|\vec{r}\rangle = I(\vec{r}) \tag{A-54}$$

in accordance with the classical definition of the radiance function, considering the fact that in paraxial approximation the emissivity is proportional to intensity, I. Analogously, we obtain the classical relation between the radiation flux F, intensity I, and radiance function. Using Eq. (A-34), we obtain

$$\begin{aligned} F &= \iint I(\vec{r})d^2r = \iint\langle\vec{r}|\hat{\rho}|\vec{r}\rangle d^2r \\ &= \iiint\int\langle\vec{r}|\hat{\rho}|\vec{p}\rangle\langle\vec{p}|\vec{r}\rangle d^2r\,d^2p \\ &= \iiint\int B(\vec{r},\vec{p})d^2r\,d^2p \end{aligned} \tag{A-55}$$

A.7 Liouville Theorem

A.7.1 The Liouville Theorem as an Asymptotic Case for the Density Matrix Motion Equation

Using the motion equation for the density matrix (see Eq. (A-43)):

$$i\hbar\frac{\partial\hat{\rho}}{\partial z}=\left(\hat{H},\hat{\rho}\right)$$

we can provide the "classical" asymptotic approximation, $\hbar \to 0$, by replacing the commutating relation $\left(\hat{H},\hat{\rho}\right)$ by classical Poisson brackets, in the form

$$i\hbar\left(\hat{H},\hat{\rho}\right)\overset{\hbar\to 0}{\Longrightarrow}\left(\frac{\partial H}{\partial x}\frac{\partial \rho}{\partial p_x}-\frac{\partial \rho}{\partial x}\frac{\partial H}{\partial p_x}\right)+ +\left(\frac{\partial H}{\partial y}\frac{\partial \rho}{\partial p_y}-\frac{\partial \rho}{\partial y}\frac{\partial H}{\partial p_y}\right);\quad \text{and}\quad \frac{\partial\hat{\rho}}{\partial z}\Rightarrow\frac{\partial \rho}{\partial z} \tag{A-56}$$

and, comparing Eq. (A-43) with Eq. (A-56), we obtain

$$\frac{\partial \rho}{\partial z}+\left(\frac{\partial \rho}{\partial x}\frac{\partial H}{\partial px}-\frac{\partial H}{\partial x}\frac{\partial \rho}{\partial px}\right)+\left(\frac{\partial \rho}{\partial y}\frac{\partial H}{\partial py}-\frac{\partial H}{\partial y}\frac{\partial \rho}{\partial py}\right)=0 \tag{A-57}$$

where ρ is the classical phase-space density function [33]. Using Hamilton's equations [33]

$$\frac{dx}{dz}=\frac{\partial H}{\partial px}\qquad\frac{dy}{dz}=\frac{\partial H}{\partial py} \tag{A-58a}$$

$$\frac{dpx}{dz}=-\frac{\partial H}{\partial x}\qquad\frac{dpy}{dz}=-\frac{\partial H}{\partial y} \tag{A-58b}$$

Eq. (A-57) becomes

$$\frac{\partial \rho}{\partial z}+\left(\frac{\partial \rho}{\partial x}\frac{dx}{dz}+\frac{dpx}{dz}\frac{\partial \rho}{\partial px}\right)+\left(\frac{\partial \rho}{\partial y}\frac{dy}{dz}+\frac{dpy}{dz}\frac{\partial \rho}{\partial py}\right)=0, \tag{A-59}$$

or, using the total derivative,

$$\frac{d\rho}{dz} = \frac{\partial \rho}{\partial z} + \mathrm{div}(\rho \vec{v}) = 0 \qquad \text{(A-60)}$$

where $\vec{v} = (\dot{x}, \dot{y})$,

i.e., in the paraxial approximation, we obtain the classical Liouville theorem, as a consequence of the density matrix motion equation. If, on the basis of Eq. (A-55), we identify the generalized radiance function $B(\vec{r}, \vec{p})$ with phase-space density $\rho(\vec{r}, \vec{p})$, we also obtain the free space form of the radiative transfer equation:

$$\vec{s} \nabla B = 0 \qquad \text{(A-61)}$$

It should also be noted that the Liouville equation (A-60), or

$$\frac{dB}{dz} = 0 \qquad \text{(A-62)}$$

is equivalent to the classical motion equation for the radiance function

$$B(\vec{r}, \vec{p}) = B_o \left(\vec{r} - (z / s_z) \vec{p}, \vec{p} \right) \qquad \text{(A-63)}$$

that can be interpreted as following. Consider the geometry of Eq. (A-63), illustrated in Figure A-1.

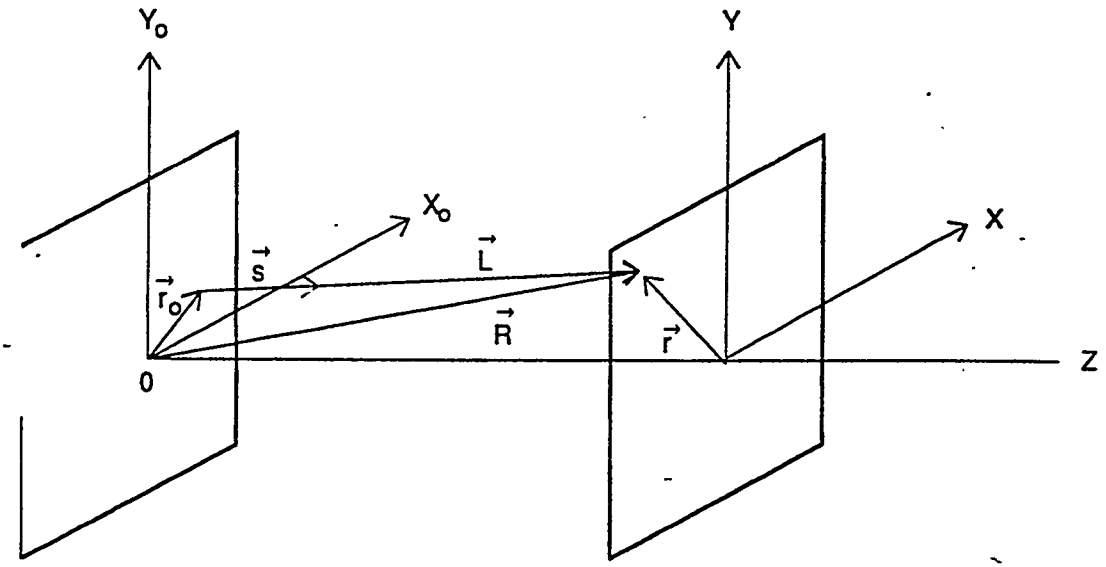

Figure A-1
Geometry of Eq. (A-63)

On the basis of Eq. (A-63),

$$\vec{r}_0 = \vec{r} - (z/s_z)\vec{p} \tag{A-64}$$

or

$$\vec{r} - \vec{r}_0 = (z/s_z)\vec{p} = \vec{\ell} \tag{A-65}$$

where $\vec{L}$, illustrated in Figure A-1, is

$$\vec{L} = (\vec{\ell}, \ell s_z) = (\ell \cdot \vec{p}, \ell s_z) = \left(z/s_z \vec{p}, \ell \cdot s_z\right) \tag{A-66}$$

since, according to Figure A-1, $\ell = z/s_z$. Therefore, indeed, Eq. (A-64) satisfies the geometry illustrated in Figure A-1.

A.7.2 Liouville Theorem in Spherical Coordinates

Using the Lagrangian in spherical coordinates, we have

$$L = n\sqrt{1 + r^2\dot{\theta}^2 + r^2 \sin^2\theta\dot{\rho}^2} \tag{A-67}$$

where $\dot{\theta} = d\theta/dr$, $\dot{\rho} = d\rho/dr$; also, $p_\theta = \frac{\partial L}{\partial \dot{\theta}}$, $p_\rho = \frac{\partial L}{\partial \dot{\rho}}$, and the Liouville theorem is

$$\frac{\partial \rho}{\partial r} + \mathrm{div}(\rho \vec{v}) = 0 \text{ or} \tag{A-68}$$

$$\frac{\partial \rho}{\partial r} + \frac{\partial}{\partial \theta}\left(\rho \frac{d\theta}{dr}\right) + \frac{\partial}{\partial \rho}\left(\rho \frac{d\rho}{dr}\right) + \frac{\partial}{\partial p_\theta}\left(\rho \frac{dp_\theta}{dr}\right) + \frac{\partial}{\partial p_\rho}\left(\rho \frac{dp_\rho}{dr}\right) = 0 \tag{A-69}$$

Here, the r coordinate is a parameter, not the z coordinate, and the phase volume element is always Cartesian

$$dV = d\theta\, d\rho\, dp_\theta\, dp_\rho \tag{A-70}$$

Obviously, in the case of a non-uniform medium, we need to replace the $\vec{p}$ vector by the $\vec{k}$ vector

$$\vec{k} = kn\vec{p} \tag{A-71}$$

As an example, we can consider the spectrum with cylindrical symmetry. In such a case,

$$k_\theta^2 + k_\rho^2 \le n^2 \sin^2\alpha = K^2 \tag{A-72}$$

where α is the cone angle and the phase space volume is

$$V = 4\pi r^2 \pi K^2 \tag{A-73}$$

On the basis of the Liouville theorem in spherical coordinates, the phase space volume (A-73) is invariant, i.e.,

$$r\, n \sin\alpha = \text{inv.} \tag{A-74}$$

Using this equation for two concentric spherical surfaces with radii r_1 and r_2, we have

$$r_1 n_1 \sin \alpha_1 = r_2 n_2 \sin \alpha_2 \qquad \text{(A-75)}$$

and assuming $n_1 = 1$ (air), $n_2 = n$ and $\alpha_2 = \pi/2$ and $\alpha_1 = \alpha$, we obtain the following formula for the theoretical limit of concentration

$$C = \frac{4\pi r_1^2}{4\pi r_2^2} = \left(\frac{n}{\sin \alpha}\right)^2 \qquad \text{(A-76)}$$

where α defines the angular acceptance of the incident radiation. As a result, we obtain the ideal 3-D concentrator.

conf abstract, preprint removed; reprints removed. db